SCUOLA DI DOTTORATO
UNIVERSITÀ DEGLI STUDI *MEDITERRANEA* DI REGGIO CALABRIA

DEPARTMENT OF CIVIL ENGINEERING, ENERGY, ENVIRONMENT AND MATERIALS (DICEAM)

DOTTORATO DI RICERCA IN
INGEGNERIA CIVILE, AMBIENTALE E DELLA SICUREZZA" CURRICULUM "INGEGNERIA IDRAULICA, COSTRUZIONI IDRAULICHE E MARITTIME, IDROLOGIA E ENERGIA DALLE ACQUE"

S.S.D. ICAR/02

XXXII CICLO

MODELING OF THE 1783 TSUNAMI EVENT IN SCILLA GENERATED BY EARTHQUAKE AND LANDSLIDE

DOTTORANDO:
Francesca Minniti

TUTOR:
Prof. Giuseppe Barbaro

Prof. Giorgio Bellotti

COORDINATORE:
Prof. Felice Arena

REGGIO CALABRIA, GENNAIO 2021

FRANCESCA MINNITI

MODELING OF THE 1783 TSUNAMI EVENT IN SCILLA GENERATED BY EARTHQUAKE AND LANDSLIDE

ABSTRACT

In 1783 began what has gone down in history as the great seismic crisis in Calabria, during which two major earthquakes occurred which affected the Calabrian ridge from the Strait to the north. Between 6th and 7th February in Scilla there was the tsunami that caused the greatest number of victims in Italy: 1500 people.

The mechanism that triggered the tsunami was the detachment of a ridge of rock due to the violent earthquake that affected the area; this detachment caused a subaerial landslide which , by sliding, then deposited on the seabed a few kilometers from the coast, immediately generating the tsunami event. The generation mechanism was, therefore, by evaluating temporally what happened, the submarine deposit of the landslide that broke off the coast.

During these years some studies have been carried out, by means of numerical modeling, aimed at interpreting and evaluating the extent of the event; the understanding and relative modeling capacity of an event of this magnitude is fundamental for future risk assessments on the Calabrian coasts that could be affected by these phenomena.

The objective of the research is to perform numerical simulations with state-of-art tsunami generation and propagation models, using the best possible bathymetric and topographic data and the historical data to compare the goodness of the results.

In this way we obtain the validation of a model that can be used to simulate possible events of this magnitude on the Calabrian coasts and therefore be able to have a reliable tsunami early warning system; it has also the advantage of perfectly combining computational burdens and goodness of results.

Regarding the hypothesis made in this study on the shape and the sliding time of the landslide necessary for the simulation, reference was made to models and simulations developed by other authors, in particular Mazzanti and Bozzano (2008).

Once the landslide and its movement has been hypothesized, it was inserted in the model and the event was simulated; the data was compared with the historical data deriving from a collection of testimonies of survivors.

A numerical model developed by Bellotti (2008) an based on the mild-slope equation is applied to reproduce the propagation of small-amplitude transient waves. The model make use of the Fourier Transform to convert the time-dependent hyperbolic equation into a set of elliptic equations in the frequency domain.

This application is presented to show the applicability of the present approach to real life scenarios; at the end it is discussed how this model could be applied as support to a tsunami early warning system in Calabrian coasts.

Keywords: *Tsunami hazard – landslide generated tsunami – numerical modeling of wave propagation – mild slope equation (MSE), Scilla (RC), Fourier Transform, warnig system in Calabrian coasts.*

CONTENTS

LIST OF FIGURES.....

LIST OF TABLES .....

INTRODUCTION **1**

1. DEPTH INTEGRATED WAVE MODEL WITH INCLUSION OF LANDSLIDE TSUNAMIS GENERATION.....4

1.1 Introduction..... 4

1.2 Derivation of model equation 7

1.3 Fully-dispersion model derivation..... 11

1.3.1 Field equation 11

1.3.2 Boundary conditions 14

1.3.3 On the application of the model..... 16

2. THE SCILLA 1783 CASE **20**

2.1 Historical review..... 20

2.1.1 Historical sources on the event..... 20

2.1.2 Historical data of the event..... 29

2.2 Literature review 36

2.2.1 The landslide source..... 36

2.2.2 The catastrophic tsunami..... 49

3. SIMULATION SOFTWARE COMSOL MULTIPHYSICS..... **66**

3.1 Introduction..... 66

3.2 Equation-based models..... 66

3.2.1 Mathematics interfaces 66

3.2.2 Coefficient form PDE interfaces (c)..... 67

4. MODELING LANDSLIDE AND TSUNAMI **72**

4.1 Methodology 73
4.2 Geographic data and domain 74
4.3 Landslide modeling 78
4.4 Wave propagation modeling 90
4.4.1 Geographic domain 90
4.4.2 Geographic data 91
4.4.3 Source term 93
4.4.4 Boundary conditions 94
4.4.5 Meshing computational domain 95
4.4.6 Numerical simulation 96
4.4.7 Discussion 100
5. RISK ANALYSIS AND MANAGEMENT OF TSUNAMIS IN CALABRIA 104
5.1 Methodology 104
5.2 Results 105
5.3 Discussion 110
CONCLUSIONS 112
BIBLIOGRAPHY 115

LIST OF FIGURES

Fig. 1.1 Sketch representing the main variables involved in the analytical model. **5**

Fig. 2.1 Epicenters (red triangles), dates and magnitudes of the five strongest earthquakes affecting Calabria during the sequence of 1783 (Zaniboni et al.,2016). **20**

Fig. 2.2 Localization of the effects of the earthquake of February 6, 1783. The time is indicated in time universal (UT), which is one hour ahead of local time (Comastri and Mariotti, 2008).. ..... **22**

Fig. 2.3 Views of various landslides on the Calabrian coast around Scilla occurred in 1783 (Comastri and Mariotti, 2008). **25**

Fig. 2.4 Location of the landslide triggered by the earthquake that was followed by the tsunami (source QGIS) **29**

Fig. 2.5 Georeferenced map of the territory obtained from a 5x5 DTM and processed in QGIS software (source QGIS). 3**0**

Fig. 2.6 Zoom of the georeferenced map of the territory affected by the landslide obtained from a 5x5 DTM and processed in QGIS software (source QGIS). 3**0**

Fig. 2.7 3D perspective view of the Scilla coastal sector. The white dashed line bounds the 1783 landslide deposit. The red dashed line encloses the subaerial landslide. The yellow dotted lines identify the lateral boundaries of the submarine depression (Mazzanti and Bozzano,2011) **31**

Fig. 2.8 **a** Topo-bathymetry of the region where the slide occurred. The subaerial slide scar (red line) is stillobservable today. The magenta dashed contour encloses the observed deposit, at about 300 m sea depth. **b** Satellite image from Google Earth_, of Scilla, with the two beaches of Marina Grande and Chianalea (Zaniboni et al.,2016). **32**

Fig. 2.9 View of the Scilla landslide scar area from the Tyrrhenian sea (Bozzano et al.,2008). **36**

Fig. 2.10 Aerial view and present multibeam bathymetry (left) and pre-landslide 50 m DTMM(right) used in the landslide modelling (Mazzanti and Bozzano,2011). **39**

Fig. 2.11 Time sequence of the landslide propagation (plan view). Thered dotted linebounds the real mapped landslide deposit (Mazzanti and Bozzano,2011).. ..... **40**

Fig. 2.12 Time sequence of the landslide velocity distribution during the first 42 s of numerical simulation (Mazzanti and Bozzano,2011).. ..... **41**

Fig. 2.13 Time sequence of the landslide thickness distribution during the first 42 s of numerical simulation (Mazzanti and Bozzano,2011).. ..... **42**

Fig. 2.14 Topography and bathymetry of the simulation computational domain (coordinates expressed in WGS84-UTM, zone 33 N). The initial slide thickness is depicted with a yellow-red palette. The sliding surface is portrayed in light gray. The central dark blue line is the predefined trajectory of the center of mass of the blocks forming the slide. The simulated final deposit is represented in different green tones and refers to the simulation with friction coefficients providing the best misfit. Notice that the most massive part of the simulated slide stops inside the boundary of the observed deposit (magenta dashed contour) (Zaniboni et al.,2016).. ..... **44**

Fig. 2.15 Computed misfit for different combinations of subaerial and submarine friction coefficients. The color scale marks the values, with purple and blue denoting the $\mu_{SA} - \mu_{SM}$ pairs providing the least misfit between the simulated and the observed deposit (Zaniboni et al.,2016).. ..... **46**

Fig. 2.16 Mean velocity (red line), CoM velocity (black circles) and Froude number (blue line) time histories. The Froude number is computed in terms of the average velocity and average depth of the underwater blocks .Magenta triangles mark the instants when block n enters the water. The velocity peak occurs at17 s. The Froude number curve crosses the critical value around 27 s (Zaniboni et al.,2016).. ..... **48**

Fig. 2.17 Scilla 1783 slide simulation by means of the code UBO-BLOCK1. Upper Panel) profile of the initial sliding body (in blue) and of the final simulated deposit at about 300 m depth (in red) over the undisturbed sliding surface (grey area). Middle panel) acceleration of the individual CoMs (black circles) and of the CoM of the whole slide (green line) vs. distance along the sliding profile. Lower panel) CoM velocities (black dots) and average velocity (green line) plotted on the sliding track distance (Zaniboni et al.,2019)..... **49**

Fig. 2.18 Sketch explaining how the landslide simulation results (in terms of velocity and geometry) are converted in order to be used as input parameters for the tsunami modelling (Mazzanti and Bozzano,2011)..... **51**

Fig. 2.19 DTMM (Digital Terrain and Marine Model) of Southern Calabria and the sector of Sicily overlooking the Messina Straits with indicated the location of the 1783 Scilla landslide, the villages affected by the Tsunami and the gauge points used in the tsunami simulation (Mazzanti and Bozzano,2011)..... **52**

Fig. 2.20 Time sequence of the wave surface elevation during the first 10 min after the landslide occurrence (Mazzanti and Bozzano,2011). **53**
Fig. 2.21 Maximum surface elevation of the wave during the first20 min after the slide. Values higher than 10 m are reported as thedark red color (Mazzanti and Bozzano,2011). **53**
Fig. 2.22 Propagation fields of the 1783 tsunami, given every 10 s. Sea level positive (negative) elevation is reproduced with a yellow-red (cyan-blue) palette. In each snapshot, the instantaneous position of the slide with thickness larger than 2 m (less than 2 m) is reported in green (gray) and the observed deposit in dashed black (Zaniboni et al.,2016).. ..... **55**
Fig. 2.23 **a** Maximum sea surface elevation. The green area is the initial landslide position. Places with tsunami observations (see Table 6) are marked by black triangles. **b** Zoom over the Marina Grande beach [delimited by th eblack rectangle in (a)] (Zaniboni et al.,2016).. ..... **56**
Fig. 2.24 Synthetic marigrams computed in four different locations shown in the right map as purple circles. The green area shows the landslide initial position (Zaniboni et al.,2016). **57**
Fig. 2.25 Computational grids adopted for numerical simulation of tsunami propagation: Grid 1 (dashed green) was used for the tsunami simulations by Zaniboni et al. (2016); Grid 2 (in red) has been used in the first simulation of this paper; Grid 3 and 4 (in blue) are an extension of Grid 1 covering the target area of Capo Peloro (Zaniboni et al.,2019). **59**
Figure 2.26. Maximum tsunami elevation, computed for each point of Grid 2. Numbers represent the positions of the available observations (see Table 2). The respective toponyms are reported in the legend together with the inundation distance (I) and runup (R). The blue dashed rectangle marks the limits of the 10 m resolution Grids 3 and 4, zooming on the area of Capo Peloro, that differ from one another only for a small part of their topography. The purple boundary delimits the sliding surface of the 1783 Scilla landslide (Zaniboni et al.,2019). **60**
Fig. 2.27. Area covered by Grids 3 and 4 employed to simulate the impact of the 1783 tsunami in Capo Peloro, the easternmost point of Sicily. The magenta contour delimits the strip swept by the landslide (Zaniboni et al.,2019)..... **61**
Fig. 2.28. Propagation frames for the 1783 Scilla landslide-tsunami in the target area of Capo Peloro, eastern Sicily (Zaniboni et al.,2019). **63**
Fig. 2.29. Maximum water inundation in Capo Peloro for the high-resolution Grid 3 (western portion). The purple squares mark the cells inundated in the simulation with the low-resolution Grid 2. The black symbols represent the positions of historical buildings: Torre degli Inglesi, the site where

tsunami deposits were recognized and associated with the 1783 event (Pantosti et al.,2008); Torre Bianca, partially buries by sand deposits (Bottari and Carveni, 2009) (Zaniboni et al.,2019)..... **64**
Fig. 4.1 Reference domain for the event of 1783 (source Google Earth). **75**
Fig. 4.2 QGIS shapefile that identifies bathymetric data (source QGIS). **76**
Fig. 4.3 QGIS shapefile that identifies a zoom of the area most affected by the tsunami. (source QGIS) **76**
Fig. 4.4 2D plane view of meshgrid interpolating bathymetric data. **77**
Fig. 4.5 3D plane view of meshgrid interpolating bathymetric data. **77**
Fig. 4.6 Identification of the subdomain affected by the landslide in QGIS. **78**
Fig. 4.7 2D plane view of the landslide geometric shape.. 79
Fig. 4.8 3D plane view of the landslide geometric shape.. 79
Fig. 4.9: 2D plane view of the ellipsoidal bathymeric subdomain.. ..... **80**
Fig. 4.10: 3D plane view of the ellipsoidal bathymeric subdomain.. ..... **80**
Fig 4.11 Landslide modeling at time T= 5 sec.. ..... **82**
Fig 4.12 Landslide modeling at time T= 10 sec.. ..... **82**
Fig 4.13 Landslide modeling at time T= 15 sec.. ..... **83**
Fig 4.14 Landslide modeling at time T= 20 sec.. ..... **83**
Fig 4.15 Landslide modeling at time T= 25 sec.. ..... **84**
Fig 4.16 Landslide modeling at time T= 30 sec.. ..... **84**
Fig 4.17 Landslide modeling at time T= 35 sec.. ..... **85**
Fig 4.18 Landslide modeling at time T= 40 sec.. ..... **85**
Fig 4.19 Landslide modeling at time T= 45 sec.. ..... **86**
Fig 4.20 Landslide modeling at time T= 50 sec.. ..... **86**
Fig 4.21 Landslide modeling at time T= 55 sec.. ..... **87**
Fig 4.22 Landslide modeling at time T= 60 sec.. ..... **87**
Fig 4.23 Landslide modeling at time T= 65 sec.. ..... **88**
Fig 4.24 Landslide modeling at time T= 70 sec.. ..... **88**
Fig 4.25 Landslide modeling at time T= 75 sec.. 89
Fig 4.26 Landslide modeling at time T= 80 sec.. 89
Fig 4.27 QGIS shapefile representing domain boundaries.. ..... **90**
Fig 4.28 Scilla computational domain purified from the part of land.. ..... **91**
Fig. 4.29 2D plane view of meshgrid interpolating bathymetric data of Scilla.. ..... **92**

Fig. 4.30 3D plane view of meshgrid interpolating bathymetric data of Scilla. **92**
Fig. 4.31 Scilla coastline interested by full-reflection boundary condition.. ..... **94**
Fig. 4.32 Scilla coastline interested by radiation boundary condition..... **95**
Fig. 4.33 Zoom of the elements of the mesh for the area of Scilla.. ..... **96**
Fig. 4.34 Points where the elevation of the wave was evaluated. In green there is the area of Chianalea; in red Scilla Sud; in orange Scilla Nord. The arrow indicates the position of the landslide and the point where the wave elevation was evaluated.. ..... **97**
Fig. 4.35 Free surface elevation obtained from the depth integrated model in Monte Capo Pacì (the landslide source)... ..... **98**
Fig. 4.36 Free surface elevation obtained from the depth integrated model in Scilla Marina Grande Nord... ..... **98**
Fig. 4.37 Free surface elevation obtained from the depth integrated model in Scilla Marina Grande Sud **99**
Fig. 4.38 Free surface elevation obtained from the depth integrated model in Scilla Chianalea. **99**
Fig. 4.39 Superimposition of the four distributions to better highlight the different effects of the tsunami at the considered locations. In blu there is the free surface elevation in Scilla Marina Grande Sud, in red there is the free surface elevation in Scilla Marina Grande Nord, in black there is the free surface elevation in landslide source, in yellow there is the free surface elevation in Scilla Chianalea. **100**
Fig. 5.1 Location of the areas with values of historical data: Scilla, Cannitello (Villa San Giovanni), Reggio Calabria..... **106**
Fig. 5.2 Location of the points where the inundation is evaluated. **106**
Fig 5.3 Inundation hypothesis in pink of 200 m near Livorno river and of 90 m along S. Nicola's Curch in Marina Grande and of 10 m in Chianalea, (Calabrian Geoportal,1954). **107**
Fig 5.4 Inundation hypothesis in pink of 200 m near Livorno river and of 90 m along S. Nicola's Curch in Marina Grande and of 10 m in Chianalea, (Bing, nowadays). **107**
Fig 5.5 Inundation hypothesis in pink of 50 m in Cannitello (Villa San Giovanni), (Calabrian Geoportal,1954)..... **108**
Fig 5.6 Inundation hypothesis in pink of 50 m in Cannitello (Villa San Giovanni), (Bing, nowadays). **108**
Fig 5.7 : Inundation hypothesis in pink of 80 m in Reggio Calabria, (Calabrian Geoportal,1954).. **109**
Fig 5.8 Inundation hypothesis in pink of 80 m in Reggio Calabria, (Bing, nowaday). **109**

LIST OF TABLES

Table 1 Inundation distance and run-up height in some of the locations along the coast 33

Table 2 Summary of pieces of evidence of the 1783 tsunami in Calabria and Sicily, with the exclusion of local effects in the area of Scilla 35

Table 3 Parameters used in the best simulation of the Scilla rock avalanche by DAN3D. 38

Table 4 The landslide features used in the tsunami modelling. 50

Table 5 Run-up estimates for the locations in the study. 54

Table 6 Number and toponyms of the places where tsunami run-up heights and inundation distances are available from historical reports (modified after Graziani et al.2006) compared with the respective values obtained in the numerical simulations. 57

Table 7 Characteristics of the different grids described in the case study of Zaniboni et al. (2019). 60

Table 8 Meshgrid features interpolating bathymetric data. 77

Table 9 Meshgrid features of the bathymetric subdomain. 81

Table 10 Time features of the landslide displacement in its subaerial phase 81

Table 11 Time features of the landslide displacement in its submerged phase 81

Table 12 Coordinates of the points where the wave propagation is calculated 97

INTRODUCTION

The reconstruction of historical events that affected significantly the coasts in the Mediterranean Sea is very important since they can be used to test numerical simulation codes as well as for better estimates of the hazard and risk. One of the most relevant cases in the Mediterranean, owing to the disastrous impact and the unusual availability of plenty of very detailed observations, is the 6 February 1783 landslide-induced tsunami in Scilla.

South-eastern Calabria (Italy) is particularly susceptible to natural hazards like earthquakes, landslides and tsunamis, and it has experienced several catastrophic events in historical and pre-historical times (Sarconi 1784; Baratta 1901, 1910; Mercalli 1906).

One of the most recent events is the so-called ‘‘1783 Terremoto delle Calabrie’’ earthquake, a seismic sequence characterized by five main shocks between M5.8 and M7.3 that struck the southern part of Calabria between February 5th and March 28th 1783. The number of casualties, already high because of the earthquake, rose further due to seismic-induced phenomena such as landslides that are well described in the historical sources (Minasi 1785).

One of the largest landslides occurred 30 min after the February 6th earthquake (immediately after midnight) south of Scilla and, plunging into the sea, induced a huge tsunami, as high as 16 m, that killed more than 1,500 inhabitants along the Marina Grande beach (Hamilton 1783; Sarconi 1784; Minasi 1785; Vivenzio 1788; De Lorenzo 1877).

Given the large number of casualties, this event can be considered one of the most catastrophic landslide-induced tsunami historically documented in Italy, as already stated by the Italian Tsunami Catalogue (Tinti et al. 2007).

The huge death toll and the impression raised by the disaster induced the Bourbon government, ruling the region at that time, to finance and arrange several ad-hoc surveys. Further,such a calamity was seen as a big challenge by the coeval international scientific community that was engaged in understanding the nature of earthquakes.

Therefore, a number of additional investigations were carried out in the first years after the tragedy by scholars and travelers from different countries (see notes about the mainshock in Guidoboni et al., 2007). The overall result of these observations and research activities that is relevant for our study is that a description of the tsunami source and of the tsunami consequences was made available for future generations.

In the Mediterranean Sea, tsunamis are known to be of smaller magnitude than in the Pacific and in the Indian Oceans, but their effects can be as lethal, owing to the high coastal exposure and

vulnerability, constantly growing in the last decades as the result of an increased coastal occupation. This poses the need for more detailed assessments of tsunami hazard and of the consequences of tsunami impact, which also implies the need for more accurate numerical simulation tools.

Mazzanti and Bozzano (2011) performed the Numerical modelling of the 1783 Scilla tsunami with a linear shallow water model, which was applied to both tsunami generation and propagation as described by Harbitz and Pedersen (1992). In this model, the landslide is simplified and described as a flexible box with a pre-defined velocity progression.

Zaniboni et al. (2016) simulated the generation and propagation of the tsunami by the finite difference code UBO-TSUFD (Tinti and Tonini 2013) solving frictionless nonlinear shallow-water equations with a staggered-grid technique and dynamic boundary conditions at the coastal lowing flooding computations.

Zaniboni et al. (2019) extended the study also for the area of Capo Peloro and Punta Faro in Sicily by using the same numerical models both for landslide and tsunami simulation of the previous investigation (Zaniboni et al.,2016).

The objective of the research is to perform numerical simulations with state-of-art tsunami generation and propagation models, using the best possible bathymetric and topographic data and the historical data to compare the goodness of the results.

In this way we obtain the validation of a model that can be used to simulate possible events of this magnitude on the Calabrian coasts and therefore be able to have a reliable tsunami early warning system; it has also the advantage of perfectly combining computational burdens and goodness of results.

A numerical model developed by Bellotti (2008) and based on the mild-slope equation is applied to reproduce the propagation of small-amplitude transient waves. The model make use of the Fourier Transform to convert the time-dependent hyperbolic equation into a set of elliptic equations in the frequency domain.

This application is presented to show the applicability of the present approach to real life scenarios; at the end it is discussed how this model could be applied as support to a tsunami early warning system in Calabrian coasts.

1. DEPTH INTEGRATED WAVE MODEL WITH INCLUSION OF LANDSLIDE TSUNAMIS GENERATION

A numerical model based on the mild slope equation, suitable to reproduce the propagation of small amplitude tsunamis in the far field, is extended to reproduce the generation and the propagation of waves generated by landslides.

The wave generation is modeled through a forcing term included in the field equation, which reproduces the effects of the movement of a submerged landslide on the fluid.

1.1 INTRODUCTION

Tsunamis are long water waves generated by geophysical events, like earthquakes, landslides, submarine volcanic eruptions, etc. (Wiegel, 1955). These events produce sudden movements of the sea/ocean floor or of the water free surface, generating waves. Many different approaches and simplifications can be used to reproduce numerically/mathematically tsunamis. The most accurate models are those resolving the full three-dimensional equations of the fluid dynamics, e.g. the Navier-Stokes equations. Example of such models are those developed by Liu et al. (2005) and by Grilli et al. (1999, 2002).

These models are computationally expensive and allow the simulation of the considered phenomena over relatively small geographical areas, typically of the order of a few km2. When studying the propagation of tsunamis over large areas, i.e. at the oceanic scales, depth integrated models are certainly more appropriate. They represent a good compromise between accuracy of the results and computational costs. Traditionally these models are based on the nonlinear shallow water equations, in view of the fact that tsunamis are considered to be very long waves if compared to the water depth where they propagate. However in the recent past it has become well accepted that this kind of waves is a wave packet, that in most cases may exhibit a frequency-dispersive behavior.

The Boussinesq-type equations (BTE, Peregrine, 1967) have therefore become a standard tool for the simulation of tsunamis. These equations allow the reproduction of weakly nonlinear, weakly frequency-dispersive water waves, although recently new formulations of these equations can be applied to wider conditions. Moreover the wave frequency dispersive behavior becomes more evident for tsunamis generated by landslides, where the spatial extent of the source is usually not

much larger than the water depth. One problem that arises when reproducing tsunamis with depth integrated models, is that, other than in shallow water approximation, it is not always possible to rigorously incorporate the effects of the movements of the sea floor into the equations, in order to reproduce the generation of waves due to earthquakes or landslides.

Jiang and Le Blonde (1994) have presented a numerical model to simulate the generation due to submarine mudslide, where the generated waves are governed by the nonlinear shallow water equations forced by the time variation of the sea bottom which is totally transferred to the free water surface. Tinti at al. (2001) have presented an analytical investigation of long water waves excited by rigid bodies sliding on the sea bottom, based on the linear shallow water equations.

Their problem is based on the hyperbolic wave equation that includes a forcing term, defined as the second derivative in time of the varying water depth, modified by the passage of the landslide. Furthermore the paper of Tinti et al. (2006) shows the same technique applied in the framework of the nonlinear shallow water equations, and a filter function is introduced in the forcing term of the continuity equation in order to take into account when the slide length is no more much larger than the water depth. The continuity equation is formulated as follows:

$$\eta_t + \nabla_h \cdot (vh) = -h_t \frac{1}{\cosh(k_s h)} \qquad 1.1$$

where $\eta(x,y,t)$ is the free water surface, $v(x,y,z,t)$ is the fluid particle velocity, $h(x,y,t)=h_f(x,y)-h_l(x,y,t)$ is the water depth function defined as the fixed sea floor depth (h_f) minus the thickness of the moving landslide (h_l). k_s is the landslide length parameter, equal to $2\pi/L_s$, where L_s is the landslide length.

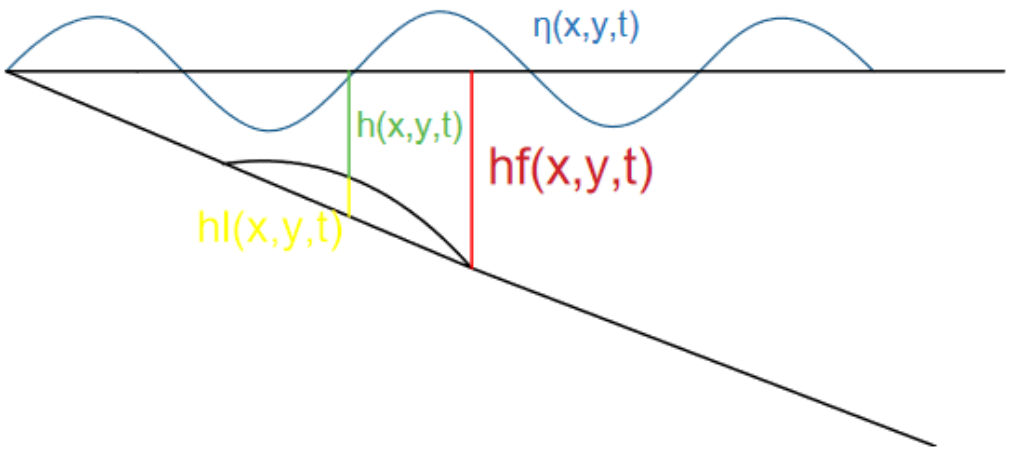

Fig. 1.1 Sketch representing the main variables involved in the analytical model.

Note that the water depth variation, due to the movements of the landslide, is filtered by means of a function which depends on the water depth and on the land-slide length. Alternatively, Watts et al. (2003) have proposed a tool namely the Tsunami Open and Progressive Initial Conditions System (TOPICS). Given the properties of the landslide, it allows calculation of proper initial conditions (in terms of water surface elevation and horizontal velocities of the fluid), that can be provided to depth-integrated models in order to represent the effects of the landslide on the waves.

Moreover, Watts et al. (2005) presented numerical model application which simulates the generation and propagation of the Indian Ocean tsunami of 26 December 2004. They split the tsunami generating fault into four segments, and the vertical dislocation along each segment was given as input to the TOP-ICS software, which by means of the Okada formula (Okada, 1985) provide, as output, a characteristic wave length and tsunami initial amplitude.

The Okada formula expresses the dislocation in a closed form in an elastic half-space. The displacement field u_i (x_1, x_2, x_3) produced by a dislocation Δu_j across a surface Σ in an isotropic medium can be defined as:

$$u_i = \frac{1}{F}\int\int_{\Sigma} \Delta u_j \left[\lambda \delta_{jk} \frac{\delta u_i^n}{\delta \xi_n} + \mu\left(\frac{\delta u_i^j}{\delta \xi_k} + \frac{\delta u_i^k}{\delta \xi_j}\right)\upsilon_k\right] d\Sigma$$

Where:

δ_{jk} = Kronecker delta;

λ, μ= Lamè coefficients.

Then they simulate the tsunami propagation solving the higher-order Boussinesq equations in their FUNWAVE model. A further method is that developed by Lynett and Liu (2002, 2005), who have re-derived a Boussinesq-like set of equations that directly incorporates the effects of the movements of the bottom induced by the landslide. They have used scaling lengths that consider also the relative depth of the landslide, also providing guidance on the importance of frequency-dispersion and waves/landslide non linearity.

Cecioni and Bellotti (NHESS, 2010) described and validated in more detail a method based on the depth integrated mild slope equation (here in after MSE), that they have already described in their previous paper Cecioni and Bellotti (Applied Ocean Research, 2010). In that work they introduced heuristically a new function for the incorporation of the effects of the moving sea floor to reproduce the waves generation.

The resulting forcing term which appears in the MSE is similar to that of Tinti et al. (2006), right hand side term of Eq. (1.1), but the filter function depends on the wavelength instead of the landslide

length. In Cecioni and Bellotti (Applied Ocean Research ,2010) it was shown that the new technique is very accurate in the limits of mild slope sea bottom and small amplitude waves and landslide and it appears essential when applying frequency-dispersive equations.

1.2 DERIVATION OF MODEL EQUATION

The model equation can be obtained starting from the linear (small amplitude) water wave equations for an incompressible irrotational fluid on an uneven bottom:

$$\nabla_h^2 \Phi + \Phi_{zz} = 0 \qquad \text{-h(x,y,t)<z<0} \qquad 1.2$$

$$\Phi_z + \frac{1}{g}\Phi_{tt} = 0 \qquad \text{z=0} \qquad 1.3$$

$$\Phi_z + h_t + \nabla_h \Phi \cdot \nabla_h h = 0 \qquad \text{z=-h(x,y,t)} \qquad 1.4$$

where ϕ(x,y,z,t) is the velocity potential in the fluid, h(x,y,t) is the water depth, defined as the fixed sea floor depth minus the landslide thickness, $h(x,y,t) = h_f(x,y) - h_l(x,y,t)$.
g is the gravity acceleration, while ∇h is the differential operator which means the divergence in the horizontal coordinates (x,y) and the symbol · stays for the scalar product. All these variables are real and scalar. Equation (1.2) is the Laplace equation, Eq. (1.3) includes the dynamic and kinematic boundary conditions at the free water surface, while Eq. (1.4) is the bottom boundary condition which reproduces the sea floor movements allowing h to varies in time. We follow the procedure described by Svendsen (2005), who starts from the Laplace equation and the free surface and bottom boundary conditions to derive the MSE, with the difference that here we take into account a moving sea floor. The solution of the given problem is assumed to be of the form

$$\phi(x,y,x,t) = \varphi(x,y,t) f(z) \qquad 1.5$$

Where ϕ(x,y,t) is the velocity potential at the undisturbed free water surface z=0, which can be complex and it includes the effects of reflected waves; f(z) is a function that describes how the kinematic field varies along the water depth and can be chosen as that resulting from the linear wave theory valid for harmonic waves propagating in constant depth, which however still holds locally for uneven bottom, i.e.

$$f(z) = \frac{\cosh[k(h_f+z)]}{\cosh(kh_f)} \quad 1.6$$

where k is the wave number, defined as 2π/L with L the wave length. In the cases of not constant depth, hf and therefore k vary with the horizontal coordinates, therefore f=f(x,y,z). However, if the mild slope assumption ${\nabla_h h_f}/{kh_f} \ll 1$ is here introduced the variation of the function f with the horizontal coordinates can be neglected if compared with the vertical one. From the assumption (1.5) it comes that

$$\Phi_{zz} = k^2\varphi \frac{\cosh[k(h_f+z)]}{\cosh(kh_f)} = k^2\Phi \quad 1.7$$

therefore the Laplace equation (1.2) can be written as

$$\Delta_h^2\Phi + k^2\Phi = 0 \quad 1.8$$

The following considerations are made:

$f(z)=1$ at $z=0$

$f_z = k\tanh(kh_f) = \frac{\omega^2}{g}$ at $z=0$

$f_z=0$ at $z=-h$ 1.9

In order to depth integrate the field equation (Laplace equation 1.2), here it is made use of the Gauss's Theorem, which states for one dimensional domain

$$\int_a^b \frac{\partial v}{\partial x} dx = v(b) - v(a) \quad 1.10$$

where υ is a differentiable vector field. By considering a special vector field defined as υ =ϕ1∇ϕ2, where ϕ1 and ϕ2 are arbitrary differentiable scalar functions, the Gauss theorem can be written as

$$\int_a^b \left[\Phi_1 \frac{\partial^2\Phi_2}{\partial x^2} + \frac{\partial\Phi_1}{\partial x}\frac{\partial\Phi_2}{\partial x}\right] dx = \left[\Phi_1 \frac{\partial\Phi_2}{\partial x}\right]_b - \left[\Phi_1 \frac{\partial\Phi_2}{\partial x}\right]_a \quad 1.11$$

Equation 1.11 is known as Green's theorem. Interchanging ϕ1 and ϕ2 and subtracting the resulting equation from (1.11) gives

$$\int_{\mathrm{a}}^{\mathrm{b}}\left[\Phi_1\frac{\partial^2\Phi_2}{\partial \mathrm{x}^2}-\Phi_2\frac{\partial^2\Phi_1}{\partial \mathrm{x}^2}\right]\mathrm{dx}=\left[\Phi_1\frac{\partial\Phi_2}{\partial \mathrm{x}}-\Phi_2\frac{\partial\Phi_1}{\partial \mathrm{x}}\right]_a^b \qquad 1.12$$

For the present purpose Eq. 1.12 is used with x=z, ϕ1=f(z) and ϕ2=ϕ(x,y,z,t), therefore

$$\int_{-h}^{0}\left(\mathrm{f}\frac{\partial^2\Phi}{\partial \mathrm{z}^2}-\Phi\frac{\partial^2\mathrm{f}}{\partial \mathrm{z}^2}\right)dz=\left[\mathrm{f}\frac{\partial\Phi}{\partial \mathrm{z}}-\Phi\frac{\partial\mathrm{f}}{\partial \mathrm{z}}\right]_0-\left[\mathrm{f}\frac{\partial\Phi}{\partial \mathrm{z}}-\Phi\frac{\partial\mathrm{f}}{\partial \mathrm{z}}\right]_{-h} \qquad 1.13$$

Substituting the Laplace equation (1.2) in the first term at the left hand side (LHS), and the boundary conditions at z=0 and z= −h(1.3 and 1.4) and using Eq. (1.9) in the right hand side (RHS) terms, then, after changing the sign, Eq. (1.13) becomes

$$\int_{-\mathrm{h}}^{0}\left(\mathrm{f}\nabla_{\mathrm{h}}^2\Phi+\mathrm{k}^2\mathrm{f}\Phi\right)\mathrm{dz}=\frac{1}{\mathrm{g}}\varphi_{\mathrm{tt}}+\varphi\frac{\omega^2}{\mathrm{g}}-[\mathrm{fh_t}]_{-\mathrm{h}}-[\mathrm{f}\nabla_{\mathrm{h}}\mathrm{h}\cdot\nabla_{\mathrm{h}}\Phi]_{-\mathrm{h}} \qquad 1.14$$

the LHS can be seen as the integration over the depth of the field equation. Considering that

$$\nabla_{\mathrm{h}}\Phi=\nabla_{\mathrm{h}}(\varphi f)=f\nabla_{\mathrm{h}}\varphi+\varphi\nabla_{\mathrm{h}}f \qquad 1.15$$

And

$$\nabla_h^2\Phi=f\nabla_h^2\varphi+2\nabla_{\mathrm{h}}\varphi\cdot\nabla_{\mathrm{h}}f+\varphi\nabla_h^2f \qquad 1.16$$

using the expression (1.15) for the last term of the RHS and expression (1.16) for the first term of the LHS, Eq. (1.14) becomes

$$\int_{-h}^{0}(f^2\nabla_h^2\varphi+2f\nabla_{\mathrm{h}}f\cdot\nabla_{\mathrm{h}}\varphi+f\varphi\nabla_h^2f+k^2f^2\varphi)\,dz=\frac{1}{g}(\varphi_{tt}+\omega^2\varphi)-\frac{1}{cosh(kh_f)}h_t-$$
$$[f\nabla_{\mathrm{h}}h\cdot(f\nabla_{\mathrm{h}}\varphi+\varphi\nabla_{\mathrm{h}}f)]_{-h} \qquad 1.17$$

Now incorporating the first two terms of the LHS of Eq. (1.17) follows

$$\int_{-h}^{0} \nabla_{\mathrm{h}} \cdot (f^2 \nabla_{\mathrm{h}} \varphi)\, dz + [f^2 \nabla_{\mathrm{h}} h \cdot \nabla_{\mathrm{h}} \varphi]_{-h} + \varphi k^2 \int_{-h}^{0} f^2\, dz = -\int_{-h}^{0} \varphi f \nabla_h^2 f dz - \frac{1}{cosh(kh_f)} h_t -$$

$$\varphi \nabla_{\mathrm{h}} h \cdot [f \nabla_{\mathrm{h}} f]_{-h} + \frac{1}{g}(\varphi_{tt} + \omega^2 \varphi) \qquad 1.18$$

Applying the Leibniz's rule for the first two terms on the LHS and knowing that

$$\int_{-\mathrm{h}}^{0} \mathrm{f}^2 \mathrm{dz} = \frac{\mathrm{cc_g}}{\mathrm{g}} \qquad 1.19$$

where c and c_g are respectively the phase and the group velocities, by multiplying Eq. (1.18) for g it results

$$\nabla_{\mathrm{h}} \cdot \left(\mathrm{cc_g} \nabla_{\mathrm{h}} \varphi\right) + \varphi k^2 \mathrm{cc_g} - \varphi_{tt} - \omega^2 \varphi + h_t \frac{g}{cosh(kh_f)} = -g\varphi \left\{ \int_{-h}^{0} f \nabla_h^2 f dz + \nabla_{\mathrm{h}} h \cdot [f \nabla_{\mathrm{h}} f]_{-h} \right\} \quad 1.20$$

Rigorously the identity of Eq. (1.19) is obtained for a single frequency of the wave spectrum, consequently Eq. (1.20) is valid for monochromatic waves, or can be seen as representative of narrow banded spectra sea state around a carrying frequency. The RHS terms of Eq. (1.20) can be shown to be $O((\nabla_h h)^2, \nabla_h^2 h)$.

Therefore, as we introduced the mild slope assumption above, i.e.: by allowing Eq. (1.6), $\nabla_h h \ll kh$ and it can be argued that the RHS terms $\ll$ LHS terms. Similarly, $\nabla^2_h h \ll \nabla_h h$, which is a natural additional assumption because $\nabla^2_h h = O(\nabla_h h)$ can only occur over short distances without changing $O(\nabla_h h)$. This means that the RHS terms are $\ll$ of all the others terms, we therefore get

$$\varphi_{tt} - \nabla_{\mathrm{h}} \cdot \left(\mathrm{cc_g} \nabla_{\mathrm{h}} \varphi\right) + \left(\omega^2 - k^2 \mathrm{cc_g}\right) \varphi = -\frac{g}{cosh(kh_f)} h_t \qquad 1.21$$

which is the hyperbolic version of the MSE in terms of fluid velocity potential and is usually referred to as the "time-dependent mild-slope equation", allowing the simulation in the time-domain of the wave propagation. To obtain the MSE in terms of the free surface elevation η, Eq. (1.21) needs to be differentiated with respect to time

$$\varphi_{ttt} - \nabla_{\mathrm{h}} \cdot \left(\mathrm{cc_g} \nabla_{\mathrm{h}} \varphi_t\right) + \left(\omega^2 - k^2 \mathrm{cc_g}\right) \varphi_t = -\frac{g}{cosh(kh_f)} h_{tt} \qquad 1.22$$

and then use the dynamic boundary condition at the free surface

$$\eta = -\frac{1}{g}\varphi_t \qquad 1.23$$

from which we obtain that $\phi_t = -g\eta$ and $\phi_{tt} = -g\eta_t$, those expressions can be substituted into Eq. (1.22) to get, after dividing by g

$$-\eta_{tt} + \nabla_h \cdot \left(cc_g \nabla_h \eta\right) - \left(\omega^2 - k^2 cc_g\right)\eta = -\frac{1}{cosh(kh_f)} h_{tt} \qquad 1.24$$

which is the hyperbolic version of the MSE in terms of water free surface elevation. Note that if the phase and group velocities are evaluated in the shallow water limit as $c=c_g=\sqrt{gh}$, then Eq. (1.24) reduces to the governing equation for forced long waves

$$\eta_{tt} - \nabla_h \cdot (gh\nabla_h \eta) = \frac{1}{cosh(kh_f)} h_{tt} \qquad 1.25$$

As said the time dependent MSE is not able to reproduce broad banded spectra sea state, due to the fact that Eq. (1.24) contains some coefficients which have to be calculated for each wave frequency component. By employing the spectral approach, the model can on the contrary cover a broad spectrum wave field, typical of tsunamis, since for each wave frequency a dedicated elliptical equation is solved and, due to the linearity of the equations, superimposition of all the solutions is allowed.

1.3 FULLY-DISPERSION MODEL DERIVATION

1.3.1 Field equation

We start from the linearized (small amplitude) water wave equations for an incompressible irrotational fluid on an uneven bottom, considering two-dimensional horizontal propagation:

$$\nabla^2 \Phi + \Phi_{zz} = 0 \qquad -h(x,y) \leq z \leq 0 \qquad 1.26$$

$$\Phi_t + g\eta = 0 \qquad z=0 \qquad 1.27$$

$\eta_t - \Phi_z = 0$ z=0 1.28

$\Phi_z + \nabla\Phi \cdot \nabla h = 0$ z=-h(x,y) 1.29

Where ϕ(x,y,z,t) is the velocity potential in the fluid, η(x,y,t) is the instantaneous elevation of the free surface, h(x,y) is the water depth and g is the gravity acceleration. All these variables are real and scalar.

To simplify the problem we assume that

ϕ(x,y,x,t)= φ(x,y,t)f(z,h) 1.30

Where ϕ(x,y,t) is the velocity potential at z=0 and f(z) is a function that describes how the kinematic field varies along the water depth. Please note that, although not clearly indicated here, the function f may depend on the frequency of the waves and on the local water depth, as detailed later. Bellotti et al. (2008) followed the procedure described by Dingemans (1997), who used a variational principle to derive two evolution equations, valid for mildly sloping bottom, for the free surface elevation η and the velocity potential ϕ at the undisturbed water level z=0:

$\eta_t = G\varphi - \nabla \cdot (F\nabla\varphi)$ 1.31

$\varphi_t = -g\eta$ 1.32

F and G depend on the specific function f and are more conveniently evaluated later. They are defined as

$F=\int_{-h}^{0} f^2 dz$ 1.33

$G=\int_{-h}^{0} \left(\frac{\partial f}{\partial z}\right)^2 dz$ 1.34

Eqs. (1.31) and (1.32) are respectively equivalent to a mass and to a momentum conservation equations (it is easy to show that for very long waves f does not vary over the water depth and that (1.31) and (1.32) reduce to the linearized version of the NSWE). The first of these can be modified in order to incorporate the effect of the movements of the bottom, such those occurring during earthquakes and submerged landslides. Eq. (1.31) therefore can be heuristically rewritten as

$$\eta_t = G\varphi - \nabla \cdot (F\nabla\varphi) - h_t \qquad 1.35$$

provided that the horizontal scale of the area where the bottom moves is much larger than the scale of the water depth.

By eliminating ϕ between Eqs. (1.31) and (1.32), a single second order hyperbolic equation for η is obtained:

$$\eta_{tt} - gG\eta - \nabla \cdot (gF\nabla\eta) = -h_{tt} \qquad 1.36$$

Eq. (1.36) is usually referred to as the 'time-dependent mild-slope equation' and allows the simulation in the time-domain of the wave propagation. However F and G are to be calculated by assuming a dominant frequency of the wave spectrum, and the validity of the resulting equation is only for narrow frequency-spectra seas (see the recent work by Lee et al., 2006 and references there in).

Here a spectral approach is used to solve Eq. (1.36), resulting in a model which is valid for broad spectrum wave field as those typical of tsunamis. The Fourier Transform (see for example Mei, 1995) of Eq. (1.36) is calculated with respect to the time t (remember that f, and consequently F and G, does not depend on the time) yielding:

$$-\omega^2 N - \nabla\cdot(gF\nabla N) + gGN = \omega^2 H \qquad 1.37$$

with N(x,y,ω) being the Fourier Transform of η(x,y,t), H(x,y,ω) the Fourier transform of h(x,y,t), and as usual ω the angular frequency. Note that N and H may be complex numbers.

Now for each value of ω the function f can be chosen as that resulting from the linear wave theory valid for harmonic waves propagating in constant depth, which however still holds in the case of mildly sloping bottom, i.e.

$$f=\frac{\cosh[k(h+z)]}{\cosh(kh)} \qquad 1.38$$

where the wave number k is obtained by solving the frequency dispersion relationship

$$\omega^2 = gk\tanh(kh) \qquad 1.39$$

F and G can be calculated for any value of ω as (Dingemans, 1997):

$$F=\frac{cc_g}{g} \quad 1.40$$

$$G=\frac{\omega 2-k^2 cc_g}{g} \quad 1.41$$

where c and cg are respectively the phase and group celerity.Eqs. (1.33) and (1.34) when inserted into Eq. (1.37) lead to the elliptic version of the mild-slope equation (Berkhoff, 1972)

$$\nabla\cdot(cc_g\nabla N)+\omega^2\frac{c_g}{c}N=-\omega^2 H \quad 1.42$$

Eq. (1.42) is used for the reproduction of harmonic waves, and represents a formidable tool for studying the propagation of small amplitude waves into harbors and over coastal areas (Zhao et al., 2001). The right hand side term of Eq. (1.42) represents the generation of the tsunamis waves due to bottom movements during earthquakes and submerged landslides. This term could be set to zero if a wave-maker condition is imposed at one boundary.

Here however it is to be kept in mind that several (potentially infinite) values of ω are to be considered and therefore many equations like (1.42) need to be solved to obtain the final result in the frequency domain.

Once the equations (1.42) are solved with the appropriate boundary conditions (discussed later) the result in the time-domain can be obtained by taking the Inverse Fourier Transform of N(x,y,ω) to obtain η(x,y,t).

1.3.2 Boundary conditions

Boundary conditions are the fully reflective conditions at solid boundaries, a radiation condition and a wave-maker boundary condition, the use of which is detailed in the following.

The full-reflection boundary conditions can be expressed by imposing that the fluid velocity in the direction orthogonal to the boundary is zero.

By using Eq. (1.32) it follows that the derivative of the Fourier Transform of the free surface elevation η along the normal to the reflective boundary should be zero (see Mei, 1983):

$$N_n=0 \quad 1.43$$

The radiation boundary condition can be obtained by using a mathematical formulation that allows the waves that propagate toward the open boundaries to freely exit the computational domain. This condition can be easily formulated for progressive outgoing waves (Sommerfeld, 1964; VanDongeren and Svendsen, 1997):

$$\eta_t + \frac{c}{\cos(\vartheta_n)}\eta_n = 0 \qquad 1.44$$

where *c* is the linear phase celerity and θn is the angle the wave direction forms with the outgoing normal to the considered boundary.

The Fourier Transform of Eq. (1.44) provides the radiation condition in the frequency domain (see Beltrami et al., 2001; Steward and Panchang, 2000):

$$N_n + ik\cos(\vartheta_n)N = 0 \qquad 1.45$$

Please note that the Eq. (1.45) is non linear in the sense that θn is not known a priori and depends on the solution itself. Iterative techniques can therefore be applied or a reasonable estimate of this parameter can be used to solve the indeterminacy.

The wave-maker condition is conveniently formulated in terms of the velocity potential at z=0 as follows:

$$\varphi_n = u^I \text{ , } z=0 \qquad 1.46$$

Where u^I is the velocity at z=0 of the desired wave field orthogonal to the wave-maker boundary.

In order to obtain a mathematical expression involving η and consequently N we make use of the evolution Eq. (1.32) which if transformed in the frequency domain results as follows

$$i\omega\Phi = -gN \qquad 1.47$$

providing the usual relationship between Φ and N:

$$\Phi = -\frac{g}{i\omega}N \qquad 1.48$$

which allows rewriting of the wave-maker condition as

$$N_n = -\frac{\mathrm{i}\omega}{g} U^I \qquad 1.49$$

Being u^{I} the Fourier Transform of the desired time series of velocity at z=0. It is worth to remind that the proposed wave-maker condition is used to specify the fluid velocity at z=0, and that the velocity field for –h<z<0 is assumed to vary as the function f.
Evanescent modes are therefore not included in this formulation.

1.3.3 On the application of the model

An important point to discuss is how the waves are generated in the model. Two alternative approaches are available. The first is based on the source term in the model equation. It represents heuristically the movements of the bottom and can be used both for generating inside the domain some desired wave field (see Larsen and Dancy, 1983; Bellotti et al., 2003; Lee and Sung, 2007), or to directly model the effect of large earthquakes and landslides. The second approach makes use of the wave-maker boundary conditions, which may be considered to be similar to the wave paddle used in physical models (although here evanescent modes are not reproduced).
Both these approaches can be used following a 'direct' or an 'indirect' procedure. The 'direct' one is applicable when the movement of the bottom is known, or when the properties of the waves to be generated are known at the wave-maker boundary.
In this case the proper time series of hand the transformed variable H to be used into the Eq. (1.42) can be easily calculated by means of the discrete Fourier Transform; equivalently the fluid velocity at z=0 of the waves at the wave-maker can be calculated and directly used into Eq. (1.47).
The 'indirect 'procedure is convenient when the surface elevation time series is known at some points of the computational domain and the position of the area (or of the boundary) where the waves are generated is known. In this case it is possible to find the source terms appearing into Eqs. (1.42) or (1.47) by an inversion technique as follows. The first step is to solve the equations (1.42) using a unit value of the source term.

The result of such preliminary computation is referred to as N'(x,y,ω). In view of the linearity of the problem the true solution in the frequency domain N(x,y,ω) can be obtained by multiplying N' for the Fourier Transform of the unknown source term, indicated as S(ω):

$$N(x,y,\omega)=S(\omega)N'(x,y,\omega) \qquad 1.50$$

Let us assume that at one point P of the computational domain the elevation of the surface η_P is available. Then at that point the transformed variable N_P can be easily calculated.
Eq. (1.50) can be inverted to obtain the source term S(ω):

$$S(\omega) = \frac{N_p(\omega)}{N'_p(\omega)} \qquad 1.51$$

where N'_P is the result of the unit source term computations at the point P.
Of course this procedure is easy to apply using only the surface elevation at one point and when an identical source term, which in principle is a complex number, applies to all the generation areas/boundaries. This implies for example that the waves are generated with the same height and phase. If the records at more than one point are available, two alternative uses can be made of the data.
On the one hand it can be assumed that the source term is identical for all the generation areas/boundaries, and an optimization procedure can be used to find the value that best fits the data. On the other hand it can be assumed that each of the generation area/boundary has its own value of the source term and it is possible to write a linear system to be solved for these unknown source terms. Alternatively an overdetermined system (the number of records available is greater than the number of source terms to be found) can be solved by means of an optimization procedure.
A further practical point of interest is that the discrete Fourier transform is used and a finite set of equations is obtained, representing a finite time interval in the frequency domain.
The integral transform of the data used to generate the waves (time series of η_P ,h, u^I) is carried out using the Fast Fourier Transform. Each of the resulting field equations in the frequency domain (1.42) is solved using an available mild-slope equation solver based on the finite element method (Beltrami et al., 2001; Bellotti et al., 2003).
The inverse transform of N is finally carried out using the Inverse Fast Fourier Transform. As far as the length of the time interval to be considered is concerned it should be kept in mind that when

solving partial differential equations using the discrete Fourier Transform the solution is obtained for a finite time interval; it is assumed that the solution is periodical over that time interval and that it repeats identically over the following and the preceding time.

Therefore the selected time interval should be long enough to allow all the wave energy to exit the computational domain trough the open boundaries before the time interval ends. Otherwise interference between wave energy coming from different time intervals is obtained. If all the wave energy has left the domain at the end of the computation, the following one has zero initial conditions everywhere, as desired.

To save computational time the elliptic Eq. (1.42) should be solved only for those wave frequencies for which the Fourier Transform of the source terms used to generate the waves is significantly greater than zero. Some wave components (especially the high frequency ones) receiving negligible energy should not been considered and the corresponding Eq. (1.42) not solved.

2. THE SCILLA 1783 CASE

2.1 HISTORICAL REVIEW

2.1.1 Historical sources on the event

The catastrophic seismic sequence of February-March 1783 devastated all of central-southern Calabria and caused widespread destruction also in the Strait area and in the Messina area.

In less than two months, between February 5 and March 28, 1783, there were five very strong earthquakes and several hundred minor events (Fig. 2.1).

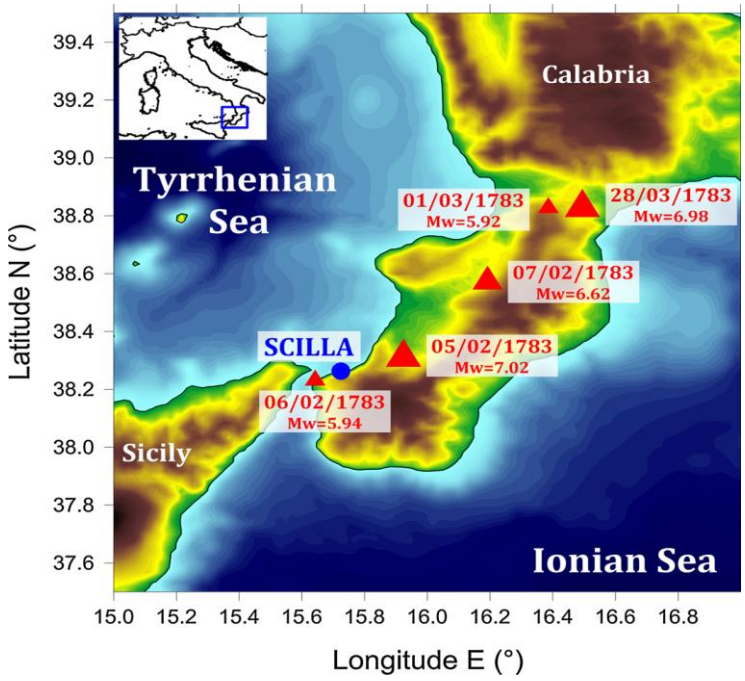

Fig. 2.1 Epicenters (red triangles), dates and magnitudes of the five strongest earthquakes affecting Calabria during 1783 (Zaniboni et al., 2016).

The cumulative picture of the damages is vast and of extraordinary severity: over 180 inhabited centers were totally or almost totally destroyed; the dead were about 30,000; the destructive effects on buildings were accompanied by extensive upheavals of the soils and of the hydrogeological system. The succession of the most violent shocks, which occurred on 5, 6 and 7 February, 1 and 28 March, shows a shift of the epicenters along the Arco Calabro from the Aspromonte region to the Marcellinara isthmus.

The proximity between the various shocks has made it very complex, and sometimes impossible, to distinguish the effects of damage relating to individual events and evaluate their intensity, taking into account the high vulnerability of a building heritage, not only of poor construction quality, but also strongly weakened by many close shocks (Boschi et al. 1995; Guidoboni et al. 2007).

One of these shocks, the one that occurred at 0:20 UT on February 6, originated in the Strait area or in the immediate vicinity. Unfortunately, this is the shock for which we have less information on the effects in the individual locations, known above all for the great tsunami that hit the beach of Scilla.

Among the numerous sources that testify to the effects of the earthquakes of 1783, the most complete are certainly the works of Michele Sarconi (1783) and Giovanni Vivenzio (1783, 1788).

The first is the final report of the mission sent by the Bourbon government to Calabria and Messina for a systematic reconnaissance of the places affected by the disaster and to gather first-hand information on all the natural phenomena that accompanied the earthquake.

The expedition, which lasted from 10 April to 2 June 1783, included numerous scientists and technicians who were members of the Academy of Sciences and Fine Arts of Naples, including the naturalist Antonio Minasi and the geographer Father Eliseo della Concezione. Unlike the academics, Vivenzio, King Ferdinand IV's personal physician, did not directly visit the places of the catastrophe, but made use of the official report drawn up by the vicar general for Calabria, Prince Francesco Pignatelli, as well as other reports from direct witnesses, and statistical data on injuries and mortality in individual localities collected by the central government.

Among the works of a general nature there is also the long report sent by Sir William Hamilton (1783) to the Royal Society of London, published in the Philosophical Transactions. The author, who at the time was the British ambassador to Naples, wrote this report after returning from a long journey made in May 1783 to the places hit by the earthquake.

There are also many memorial sources useful for the detailed reconstruction of the effects in the individual localities. In particular, for Messina we should remember the works of Alberto Corrao (1784) and Andrea Gallo (1783, 1784), professors - the first of canon law, the second of philosophy and mathematics - in the Real Collegio Carolino. For Reggio Calabria, the Memoria di Pietro Roscitano (1783), already cited above, and the Historical Note, written by the contemporary canon Gregorio Palestino and published in summary by De Lorenzo (ed. 1895).

Finally, as regards the description of the events in Scilla, the works of Girolamo Minasi (1783, 1785), direct witness of the event. The first earthquake occurred on February 5, around 12:00 UT, and

mainly affected the area of the Tyrrhenian side of Calabria between the Piana di Gioia Tauro and the north-western hills of Aspromonte. In this area almost all the buildings were devastated and many thousands of people lost their lives.

Over 20 localities, including Bagnara Calabra, Oppido Mamertina, Palmi, Santa Cristina d'Aspromonte, Sinopoli, were almost completely destroyed and another 24 towns suffered extensive destruction. In many other locations, including the cities and smaller towns on both sides of the Strait, the effects of the earthquake, although less devastating, were destructive, with serious and widespread collapses.

A little more than twelve hours later, at 0:20 UT on February 6, there was the second great quake, so as mentioned we only have information for a few locations. Probably the epicenter was in the northern part of the Strait, in the area between Scilla, Messina and Reggio Calabria which were the places most affected by this earthquake (Fig. 2.2).

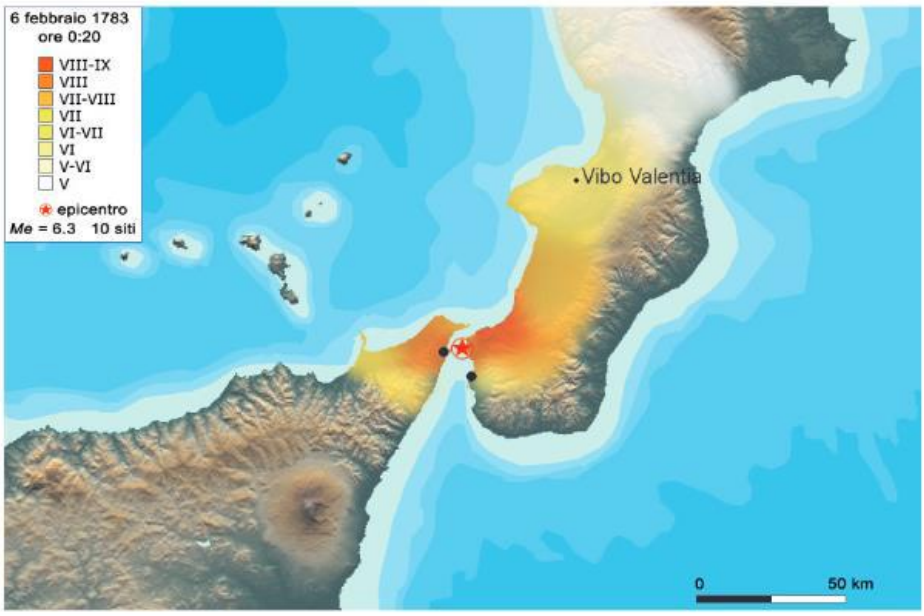

Fig. 2.2 Localization of the effects of the earthquake of February 6, 1783. The time is indicated in time universal (UT), which is one hour ahead of local time (Comastri and Mariotti, 2008).

The earthquake of February 6, 1783 was followed in Scilla by a devastating tsunami. Most likely the shock was not directly responsible for the origin of the tsunami, which was instead caused by a large landslide triggered by the earthquake, attested and described by contemporary sources. In addition

to the narrative sources mentioned above, the tsunami is documented by an iconographic testimonies.

It is an engraving of which the author is not known, made in 1790 by the Dominican father Antonio Minasi, learned naturalist and professor of botany native of Scilla, who, as mentioned above, had been part of the mission of the Neapolitan Academy in 1783.

The table is divided into five distinct views: four square-shaped representing various landslides that occurred on the Calabrian coast south of the city of Scilla, including the massive one that caused the tsunami; the fifth, rectangular in shape, is a planimetric map with an indication of the entire area affected by the landslide and the subsequent tsunami (Fig. 2.3).

1. Case de Bovi in Campallà. 2. Lesione fino dal 1782. 3. casino de Minasi. 4. Torre del Cavallo. 5. Capo S. Gregorio. 7. Capo Dirupo. 8. Lido la Nave. 9. Capo Pasci, ove lo scoglio Formica. 10. Punto di Veduta. 11. Porto di Messina. 12. Punta del Pezzo.

Alla Diletta in G.C. M.ª Emma Hart, che colla forte su

Fig. 2.3 Views of various landslides on the Calabrian coast around Scilla occurred in 1783 (Comastri and Mariotti, 2008).

The unsigned engraving, made in 1790 by Antonio Minasi, is divided into five panels. In the first, top left, the coast near Capo Pacì, south of Scilla, is depicted before the earthquakes of 1783.

Above all, one notices an evident crack that already crossed the Campallà area from 1782.

In the second box, on the side, the same area: in the lower left you can see the small landslides caused by the earthquake of 5 February 1783; in the center, the great landslide that occurred following the quake of 6 February.

In the lower left panel, the coast at Capo San Gregorio is depicted, where a large rocky boulder collapsed with the earthquake of February 5, 1783.

In the third box, at the top right, the area of Capo Pacì again after a landslide that occurred on 24 March 1790 - independent of seismic events - which caused an anomalous wave.

In the fifth square (rectangular) there is the planimetric map with the indication of the whole area affected by the phenomena described: the sign (blue in the original) that joins the two banks of the Strait indicates the path of the wave originated by the landslide Campallà area in 1783.

The philosopher Baratta in his essay *"I terremoti d'Italia. Saggio di storia, geografia e bibliografia sismica italiana"* (Torino, 1901) described the event through testimonies:

"… ..After the first shock, the ground continued to be more or less intensely agitated: Mr. Grillo in Oppido felt the earthquake triple with such subsequent frequency that in many hours the earth was either a few times quiet or almost always "taken by dark vibration". In Scilla, according to a chronicler quoted by De Lorenzo, the sea was seen invading the land every quarter of an hour and then withdraw, and this in the space of about 3 m.

According to Minasi, 140 replies were heard in the first 24 hours after the first shaking: the Gallo per Messina reports that from about 19 h on the 5th until midnight the tremors were repeated less than a quarter of an hour apart on the other.

In Monteleone Pignatari from 19 h 20 m to 23 h 45 m counted 1 light, 8 mediocre and 5 strong; from 0 h 45 m to 5 h 45 m in the night 5-6 other 90, which followed from 3 to 3, from 4 to 4 and at most 5 in 5 minutes, in addition to this constantly from 20 to 20 or from 30 to 30 m if on heard louder ones preceded by rumble.

Thus it comes to about 1 h 6 m ant. of day 6, in which a very intense reply inflicted new damage in Reggio, Messina and all the other places previously damaged (At the words of the Gallo the shock was startling and whirling at the sign that the men could not stand up. Monteleone, according to Pignatari's observation, was horizontal NNE-SSW with a strong roar, lasting about 90 seconds; in Catanzaro, according to De Leone, perhaps it was only undulating, more intense, but shorter than

the first, and so also between Cosenza and Rossano, where Masci lived. From synchronous documents published by Mercalli we learn that the second earthquake caused very serious damage to Messina, but less than that of the first, and this contrary to what Perrey claims).

And it is precisely on this occasion that the famous Scilla disaster occurred. The violence of the impact caused you to fall with an immense crash for over 2 km. coastal part of Mount Paci: the sea retreated, and, some time after the end of the earthquake, a shudder was felt starting from within the mass of waters, which spilled with unspeakable speed on the beach.

The quivering wave fled and fled again from the shore to return furiously to the beach again, rising almost to the top of the houses and churches built there, spreading mourning and desolation. About a thousand and a half people in those fatal moments lost their lives, since, frightened by the first shock, by the repeated repetitions and by the landslides that continually occurred in the mountains surrounding the town, fearing to die under the houses, mostly destroyed or made unsafe, they were sheltered under tents in the beach, or housed in boats on the sea, thus remaining a victim of the huge upheaval (since the population had abandoned their homes to retire to the navy after the first shock, so there were no victims for the fall of the buildings on the occasion of the second).

This tsunami had its maximum intensity in Scilla and therefore on the opposite bank of the lighthouse tower, where the wave invaded the shore causing the death of many people who were hospitalized in small boats and advanced about 600 steps, breaking the embankments and flooding the campaigns. On the shore of the "Marina grande" of Scilla, Minasi recalls, sponges and corals were seen thrown from the water, things that could only be found at a good distance from the beach, where the sea is at a fair depth.

[…] Sarconi mentions a mediocre tsunami which occurred on the occasion of the first shock (5 February) especially along the coasts that extend from Messina to the Lighthouse, and from Scilla to Reggio. In Messina, the sea first broke down, then, when the wave withdrew from the shore with deadly violence, it flooded it passing the bench, which was partially demolished or damaged, and flooding a portion of the maritime theater: even in Reggio the sea went out of its limits usual and invaded the road "de 'Giunchi".

At the Catona there was also some traces of flooding, as well as at the Torre del Faro and in the stretch from Peloro to the surroundings of Messina, with the difference that in the parts closest to this city it was much more sensitive.

After the earthquake in Scylla, the sea first retreated for eight steps, then began to rise, to tremble, and finally to grow as a sign that boiling (this is the impression received by a person worthy of faith

- the priest Pontilio - who was in the in the middle of the water, on a rock) ran to recover not only the stretch it had previously occupied, but a portion of the beach on which boats were stranded with sailors inside, who had to grab the oars and start rowing to save themselves.

Minasi, quoted by De Lorenzo, writes that "a little before the great earthquake was felt we saw the sea slowly move away from Lido della Canalea (di Scilla) for about ten meters, and soon resume the upward motion with the same slowness until to reach the primitive border. Even Capo Cenide, says Sarconi, traces of the invasion of the water were noted, which in the 5th day had shown - according to the inhabitants - more boiling (swirling) than usual, also altering the usual course of the tide: in this state it was kept until the morning of day 6. And De Lorenzo himself reports that some sailors in the Gulf of Gioia, at the head of the Vatican, after about 8m. who had felt the shock, noticed that the waves formed two great waves.

And the truthfulness of the news diligently collected by Sarconi is also confirmed by Vivenzio according to which the sea surrounding the Calabrian region, both in the west and in the south, was violently shaken during the shock and by the observations of Pignatari who says that after the emotion in Roccella sul Jonio and in Nicotera the sea retreated to flood the coast two or three times. Thus the various synchronous narratives all agree in admitting a tsunami on the occasion of the first shock: but comparing the phenomena presented by the sea in correlation with the second or on the occasion of earthquakes that occurred in other regions, where the epicenter was undoubtedly at sea, he sees that they are completely inadequate to believe that the impulse has come from that region.

[....] And here I believe it is necessary to mention an important and debated question: whether, that is, the terrible movement of the mass of water that occurred in Scylla after the second great shock, was a real tsunami connected with this, or instead a mechanical effect of the abrupt and sudden descend into the sea of Mount Campallà. The supporters of this second hypothesis leaned especially on what the synchronous chronicler Palestino left written. - quoted by De Lorenzo - that, that is, the steepness and the tsunami occurred half an hour after the second main shock.

On the other hand, according to Dr. Pignatari "in the shock of 7h 30m it is, that Mount Campallà falls near Scilla: perhaps the reason for which it is hardly noticed by citizens. Shortly after; but not soon, as some would like, the famous sea quake or opposite shores of Scilla and Torre del Faro occur.

No new villages fall into this shock; but neither the fallen do the ruins increase, and in the others the injuries ". And Sarconi, hinting at the second shock, adds: "in that fearful motion the upheaval of the land was such that a part of the great mount Bacì ... fell with a horrible roar ... The unfortunate ones

of the conceived terror were just found .. when sudden, after a few minutes after the tremor had cessed, I heard a shudder, and a secret whisper, which approaching from the inside of the sea ... then the vehement flood came.

Therefore the chronicler Palestino is in disagreement with what Pignatari and the Sarconi. The first between the shock and the steepness and the subsequent tsunami, asserts that about half an hour has passed, the other two instead admit that one phenomenon happened immediately, or almost to the other.

It seems to me that, given the immense violence that the storm explained in Scilla, the height to which the water reached, the strength that it had at the Torre del Faro and the movement made sensitive up to Catania, to describe it as such formidable tsunami at the steepness of Mount Campallà, is a completely inadequate cause to explain the terrible grandeur of the phenomenon [...].”

2.1.2 Historical data of the event

The earthquake of February 6, 1783 was followed in Scilla by a devastating tsunami. Most likely the shock was not directly responsible for the origin of the tsunami, which was instead caused by a large landslide triggered by the earthquake, attested and described by contemporary sources.
The location of the event is shown in the following figures (Fig. 2.4, Fig. 2.5, Fig. 2.6):

Fig. 2.4 Location of the landslide triggered by the earthquake that was followed by the tsunami (source QGIS).

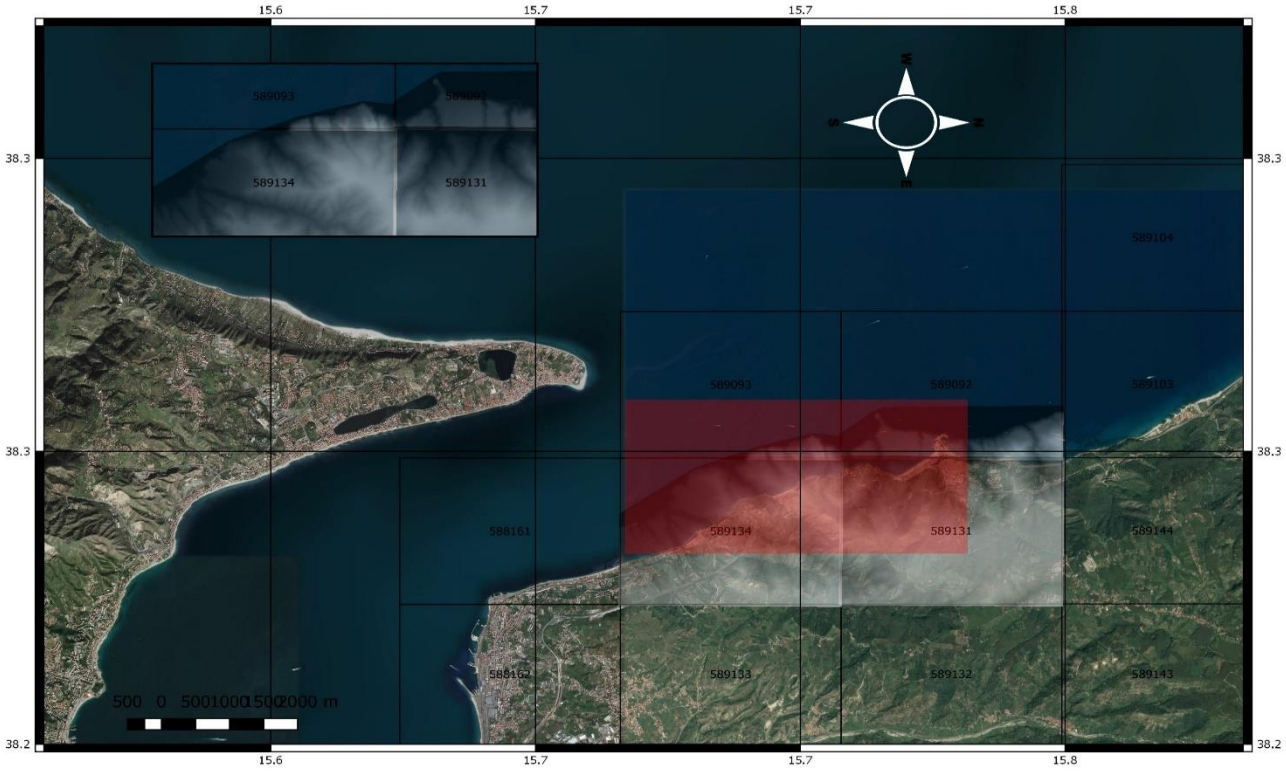

Fig. 2.5 Georeferenced map of the territory obtained from a 5x5 DTM and processed in QGIS software (source QGIS).

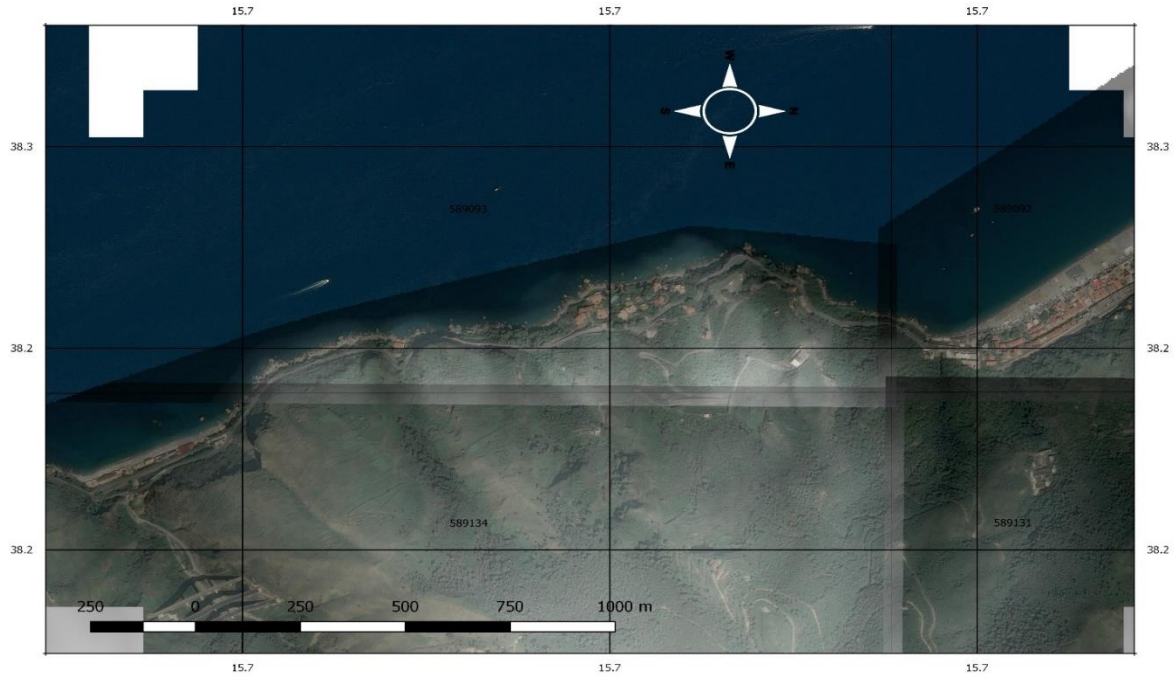

Fig. 2.6 Zoom of the georeferenced map of the territory affected by the landslide obtained from a 5x5 DTM and processed in QGIS software (source QGIS).

The Scilla coastal landslide occurred on February 6th 1783 close to the village of Scilla and was triggered by the second main shock of the ‘‘Terremoto delle Calabrie’’ seismic sequence (Boschi et al. 2000). The phenomenon affected the M. Pacı` slope (Fig. 2.7), where a large subaerial depression is still visible. The slope is quite steep (up to 45°) and intensely jointed gneiss rock and breccias crop out extensively (Bozzano et al. 2008, 2010; Mazzanti 2008a, b).

The landslide was bounded by two faults in the upper and lower part of the scar area and laterally confined (in the left flank) by a major regional fault (Monte Pacı` Fault). This geological and structural conditions of the Monte Pacı` slope represented both a predisposing factor and a kinematic control for the 1783 Scilla landslide. In particular, it is suggested the failure of a wedge of rock which then evolved into a rock avalanche due to the fragmentation of the intensely jointed rock-mass and to the slope morphology (Bozzano et al. 2008, 2010; Mazzanti 2008a, b).

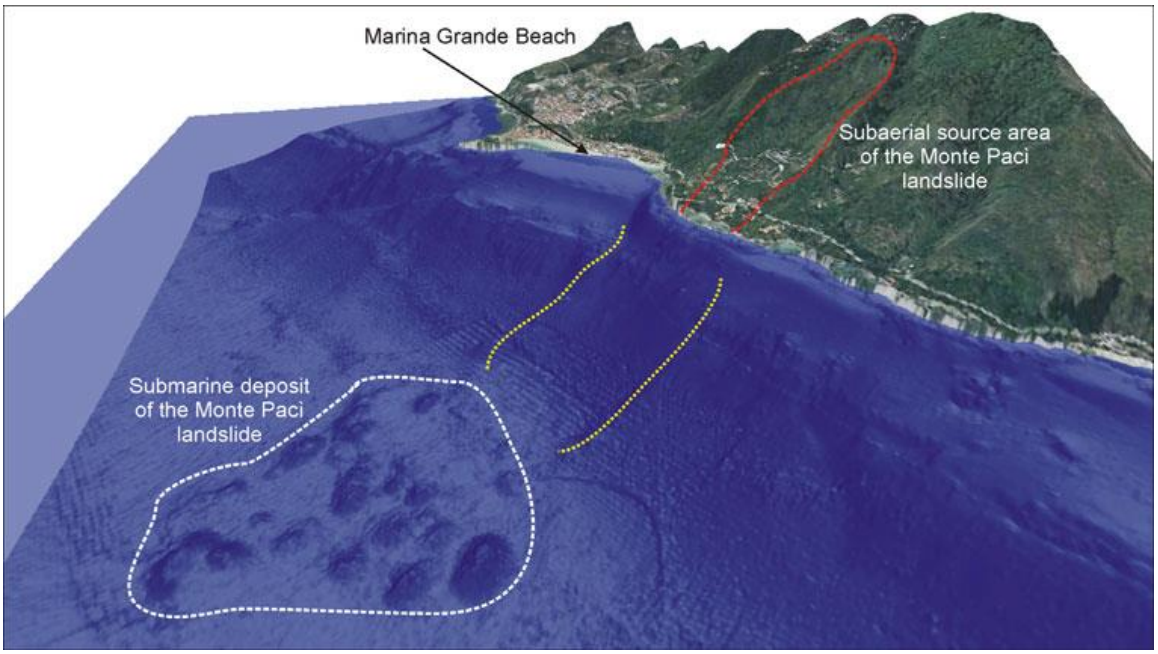

Fig. 2.7 3D perspective view of the Scilla coastal sector. The white dashed line bounds the 1783 landslide deposit. The red dashed line encloses the subaerial landslide. The yellow dotted lines identify the lateral boundaries of the submarine depression (MAzzanti and Bozzano, 2011).

Many coeval and historical reports and studies described the events in detail (Torcia 1783; Hamilton 1783; Sarconi 1784; Minasi 1785; Vivenzio 1788; De Lorenzo 1877; De Lorenzo 1895; Baratta 1901). From these, it is possible to reconstruct some features of the tsunami. Three main waves hit the shore, with heights ranging from 6 to 9 m (Sarconi 1784) (see Fig. 2.8b for location). The land was

inundated for at least 100 m, with a 200 m ingression in correspondence of the Livorno stream, in the center of Marina Grande (point 7 in Fig. 2.8b). The tsunami hit the cliffs of the Scilla Castle and affected the hamlet of Chianalea (point 8, Fig. 2.8b) on the other side of the Scilla promontory, with waves around 3–4 m high.

The tsunami affected a coastal stretch of Tyrrhenian Calabria, about 40 km long, and also the coasts of Sicily and the harbor of Messina on the other side of the Messina Straits (Tinti and Guidoboni 1988; Graziani et al. 2006; Tinti et al. 2007a).

The landslide and the tsunami have been object of scientific investigation since the first years after the event: the subaerial landslide scar, 1 km west of Scilla, extending up to 400 m a.s.l. and still visible today, is the first feature that was immediately described and characterized.

Minasi (1785) hypothesized a flank failure with a submarine front of 450 m located at more than 100 m from the coast. De Lorenzo (1895) agreed with the front position, but estimated a larger mass, with 2 km front and a length from 500 m to 2 km.

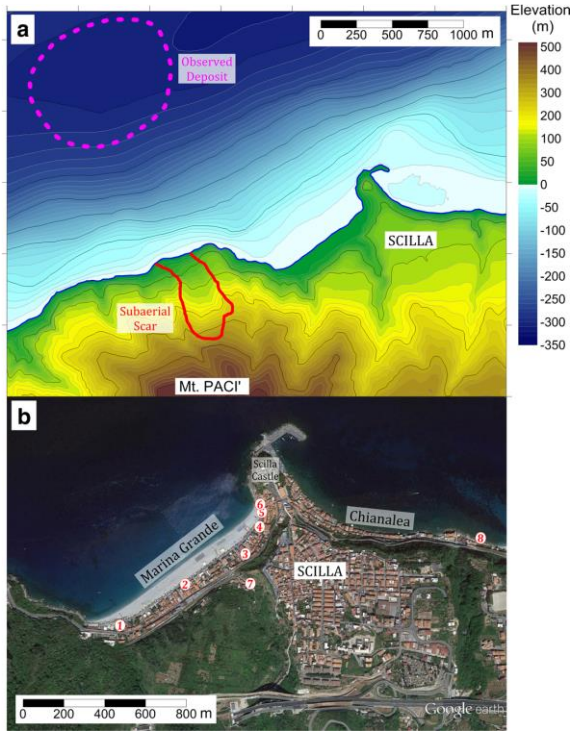

Fig. 2.8 ***a*** *Topo-bathymetry of the region where the slide occurred. The subaerial slide scar (red line) is stillobservable today. The magenta dashed contour encloses the observed deposit, at about 300 m sea depth.* ***b*** *Satellite image from Google Earth_, of Scilla, with the two beaches of Marina Grande and Chianalea (Zaniboni et. al, 2016).*

The time sequence of the earthquake, landslide and tsunami can be seen as the first clear evidence of a landslide source for the tsunami. As a matter of fact, according to historical reconstructions, the landslide occurred about 30 min after the earthquake, and the tsunami hit the adjacent Marina Grande beach 30–60 s after the landslide. Moreover, both the limited area around Scilla affected by the wave and the corresponding wave height distribution confirm the landslide origin of the tsunami (Okal and Synolakis 2004; Gerardi et al. 2008).

Maximum run-up heights ranging from 6 to 9 m according to Sarconi (1784) and up to 16 m according to Minasi (1785) were recorded along the Marina Grande beach. In the Calabrian coastal sector between Nicotera and Reggio Calabria, as well as along the Sicilian coast, several towns and villages, such as Cannitello, Bagnara Calabra, Punta del Faro, and Messina, were hit by the wave. As one can see in Table 1, however, the wave run-up height and the inundation distance (based on historical documents) drastically decrease moving away from Scilla.

Site	Inundation distance (m)	Run-up height (m)
Bagnara Calabra	n.a.	n.a.
Cannitello	50 (r)	0.8–2.9 (c)
Catona	10 (r)	0.3–0.7 (c)
Chianalea	n.a.	5–6
Marina Grande (Scilla)	n.a.	9–16 (r)
Marina San Gregorio	n.a.	n.a.
Messina	50 (r)	2 (r)
Punta del Faro	400 (r)	6–13 (c)

Table 1 *Inundation distance and run-up height in some of the locations along the coast.* ***r*** Historically reported, ***c*** Computed from the reported inundation distance (Gerardi et al. 2008), ***n.a.*** data not available *(Mazzanti and Bozzano, 2011).*

From Table 2, one can observe that the effects of the tsunami were much less in the neighboring area than in Scilla.

This is not surprising since it is typical of landslide-tsunamis to vanish rapidly with distance (see for example Masson et al., 2006; Harbitz et al., 2013, and references therein). However, remarkably the

waves were seen in Calabria from Nicotera (point 1, Figure 2.8), about 40 km north-east of Scilla, to Reggio Calabria (point 5, Figure 2.8), 20 km south-west. On the other side of the Messina Straits, the place closest to the source is the easternmost corner of Sicily, that is Capo Peloro (point 6, Figure 2.8), next to the village of Torre Faro (point 7).

Here the tsunami was strong and disastrous. In addition to historical sources, the impact of high-energy tsunami waves in this area was confirmed by recent geological investigations carried out in a site called Torre degli Inglesi (Capo Peloro, point 6), about 40 m far from the today shoreline, where a 15 cm thick sand deposit in a trench layer sequence was attributed to the 1783 event (Pantosti et al., 2008).

Region	n.	Toponym	Description of the effects	Inundation distance (m)	Run-Up (m)	References
Calabria	1	Nicotera	The sea withdrew and then inundated the beach carrying some fishing boats onshore.			*De Leone, 1783*
	2	Bagnara	Affected by the inundation.			*Minasi, 1785* *De Lorenzo, 1877*
	3	Cannitello	Affected by the inundation.	50	2.9	*Minasi, 1785* *De Lorenzo, 1877*
	4	Punta del Pezzo	Sea covered the beach by one and a half mile, leaving sand on the ground.			*Sarconi, 1784*
	5	Reggio Calabria	The sea inundated the shore carrying a lot of heavy material.	80	3.2	*Torcia, 1783* *De Leone, 1783*
Sicily	6	Capo Peloro	Flooding affected cultivated fields close to the small lake called Pantano Piccolo. Small houses, people and animals were carried seaward. Tsunami deposits identified at Torre degli Inglesi.	>400	6	*Augusti, 1783* *Torcia, 1783* *Gallo, 1784* *Pantosti et al., 2008*
	7	Torre Faro	Tsunami waves flooded the shore, depositing a large amount of silt and a lot of dead fish. Some boats were carried seaward. 26 people drowned.			*Sarconi, 1784* *Torcia, 1783* *Vivenzio, 1788*
	8	Messina	The sea was seen to rise and to noisily inundate the coast. Waves were also quite relevant at the headlight. Sea level rising by about 2 m, reached the fish market, killing 28 people.	50	2	*Minasi, 1785* *Vivenzio, 1783* *Spallanzani, 1795*

Table 2 *Summary of pieces of evidence of the 1783 tsunami in Calabria and Sicily, with the exclusion of local effects in the area of Scilla.*

2.2 LITERATURE REVIEW

2.2.1 The landslide source

In modern times, in addition to geomorphological investigations on land, two marine surveys were conducted in the slide area in 2005 and 2006 to characterize the sea bottom morphology. The first survey found evidence of a deposit made of huge blocks just in front of the subaerial scar, extending up to 1.7 km distance from the coast .

The volume of the deposit was estimated in less than 3 Mm^3 and associated with the 1783 event (Bosman et al. 2006; Bozzano et al. 2006). It was also found that the subaerial scar continues under the sea level down to 100–150 m depth, supporting the idea of an underwater portion of the slide of about 3 Mm^3 (Bozzano et al.2011).

A preliminary analysis of the subaerial scar identified the crown at 425 m a.s.l., quantifying the slide basal area to 190,000 m^2 and the length to 725 m (Bozzano et al. 2011). This leads to a volume of about 5 Mm^3, and, if one includes also the submarine part of the slide, to a total volume of about 8 Mm^3, that is much higher than the observed volume of the deposit. The discrepancy was ascribed to the erosional action of strong sea bottom currents moving parallel to coast from WSW to ENE, carrying away the looser part, easier to mobilize simulations of the slide and the generated tsunami can be found in the literature.

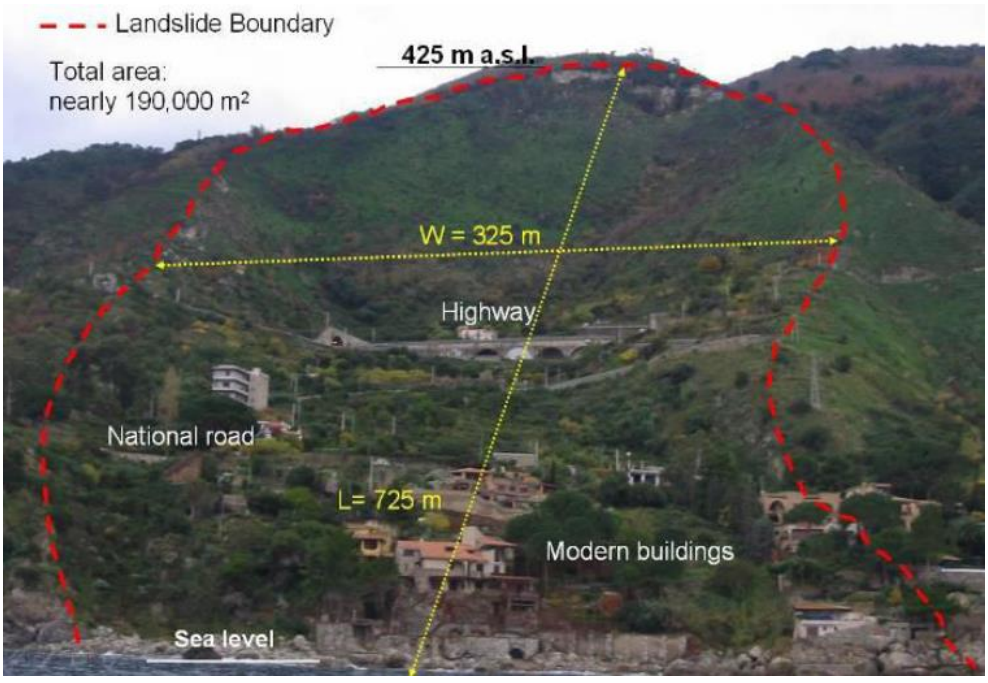

Fig.2.9 View of the Scilla landslide scar area from the Tyrrhenian sea (Bozzano et al., 2008).

Mazzanti and Bozzano (2011) modelled the post-failure propagation of the Scilla landslide using the three dimensional DAN3D code(McDougall and Hungr2004). DAN3D (Hungr and McDougall2009) is one of the most powerful codes for the numerical modelling of subaerial landslide and in the last years has been tested and calibrated over several real cases(e.g. McDougall et al.2006; Sosio et al.2008; Evans et al.2009). The main features of the DAN3D code are listed below.

(1) The material is considered as an ‘‘equivalent fluid’’(Hungr1995), governed by simple rheological relationships (McDougall and Hungr2004; Hungr andMcDougall2009) that can vary along the path of motion according to the characteristics of the land-slide material.

(2) The model considers strain-dependent, non-hydro-static, anisotropic internal stresses due to the 3Ddeformation of material with internal shear strength and centripetal acceleration due to path curvature.

(3) The model simulates mass and momentum transfer due to entrainment of material and allows for the consideration of corresponding changes in flow rheology along the path.

The depth-integrated St. Venant equations are solved usinga Lagrangian numerical method adapted from smoothed particle hydrodynamics (Monaghan1992). The momentum equations consider a fixed frictional internal rheology governed by an internal friction angle and a user-selected basal rheology, as provided by several alternative rheological kernels (Hungr1995).

The rheology is determined by one or two parameters (depending on the selected rheology) which must be adjusted by a trial-and-error calibration procedure per-formed by back-analyzing recorded events. Although the code was specifically designed to simulate the dynamics of subaerial landslides, it has been previously applied to other submarine and coastal mass movements by using the equivalent fluid equivalent medium approach (Mazzanti et al.2009; Mazzanti and Bozzano2009). By this approach, extensively described in Mazzanti and Bozzano (2009), the following basic aspects must be accounted for in the numerical simulation of coastal landslides: 1) the buoyancy effect; 2) drag forces; 3)peculiar mechanisms like hydroplaning (Mohrig et al.1998), and 4) the sudden change of environment (water impact) which can produce an impulsive loss of energy and several modifications in the flow behaviour.

The 1783 Scilla landslide was simulated using a DTMM (Digital Terrain and Marine Model) with 20 m square cells (Fig.2.10), obtained by combining subaerial DTM (based on a 1:5,000 topographic

map) and high resolution bathymetry collected by sonar multibeam surveys (Bosman et al.2006;Mazzanti2008a,b). A detached volume of 5.4 x 10^6 m^3 and a maximum run-out of 2.5 km from the upper scar were considered in the numerical back-analysis. A sensitivity analysis was performed in order to define the best rheological parameters for the simulation (Table 3).

The use of frictional rheology in the subaerial part of the slope is reasonable if we assume that the slope was affected by a rock slide-type landslide and that after the failure the landslide mass was fragmented and became a rock avalanche (Bozzano et al.2008; Mazzanti2008b). A dynamic friction angle of 16° is common for such a landslide in the subaerial (e.g. Hungr and Evans1996; review in Sosioet al.2008; Pirulli and Mangeney2008) and submarine (e.g. Mangeney et al.2000) environment. Along the sub-marine path, the Voellmy rheology (Hungr1995) was used with a dry friction coefficient μ=0.05 and a turbulence coefficient ξ=220 m/s2.

The turbulence coefficient accounts in a fictitious way for either the inner turbulence effects in the landslide's mass (assumed as an equivalent fluid) or for the drag forces that are due to the interaction of the moving mass with the surrounding water. Erosion of the moving mass along the pathway was set to zero since no data were available at this regard and it is reasonable to assume that a small thickness of erodible debris could be present along the landslide pathway.

Subaerial rheology	Frictional
Unit weight (kN/m^3)	17
Friction angle (°)	16
Erosion (m)	0
Subaqueous rheology	**Voellmy**
Unit weight (kN/m^3)	17
Friction coefficient (μ)	0.05
Turbulence coefficient (ξ) (m/s^2)	220
Erosion (m)	0

Table 3 *Parameters used in the best simulation of the Scilla rock avalanche by DAN3D (Mazzanti and Bozano, 2011).*

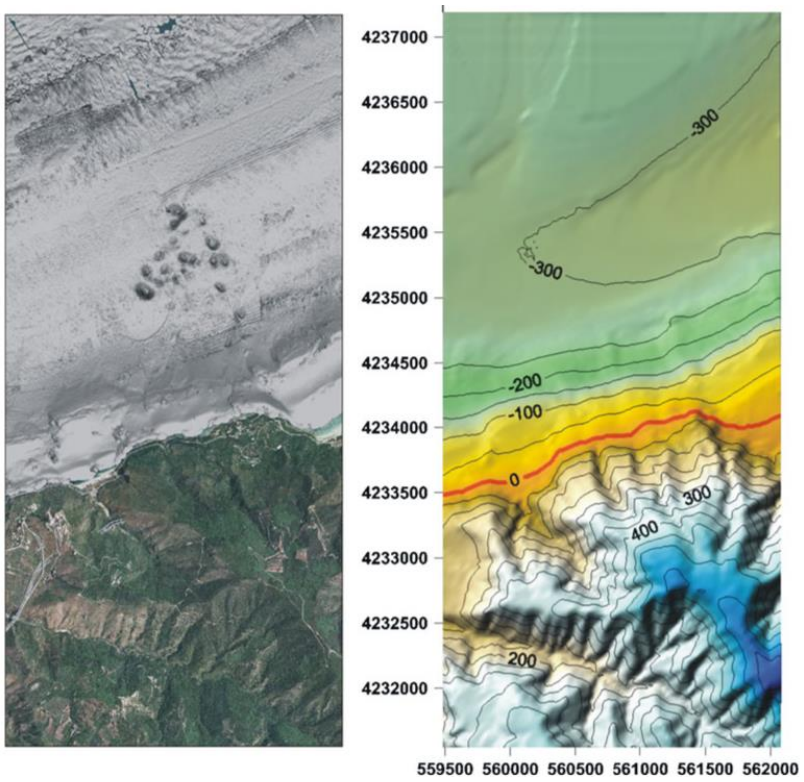

Fig. 2.10 Aerial view and present multibeam bathymetry (left) and pre-landslide 50 m DTMM (right) used in the landslide modelling (Mazzanti and Bozzano, 2011).

The simulation results (Fig. 2.11) show that the mass reaches the flat area in front of Scilla after about 40 s and the final run-out after 80 s; in the following 40 s (from 80 to 120 s),only a lateral spreading of the material is observed. Figure 2.11 shows the agreement between the computed and recorded run-out and the areal distribution of the final deposit.

This noise can be interpreted as the result of the slope failure in the elapsed time between landslide detachment and its complete submergence. This time (also accounting for the uncertainties in the historical report) is comparable to the subaerial propagation period computed by the numerical simulation. Unfortunately, no historical data are available regarding the landslide velocity. Nevertheless, the computed values are in accordance with those proposed in the literature for similar landslides (Sosio et al.2008; Locat et al.2004).

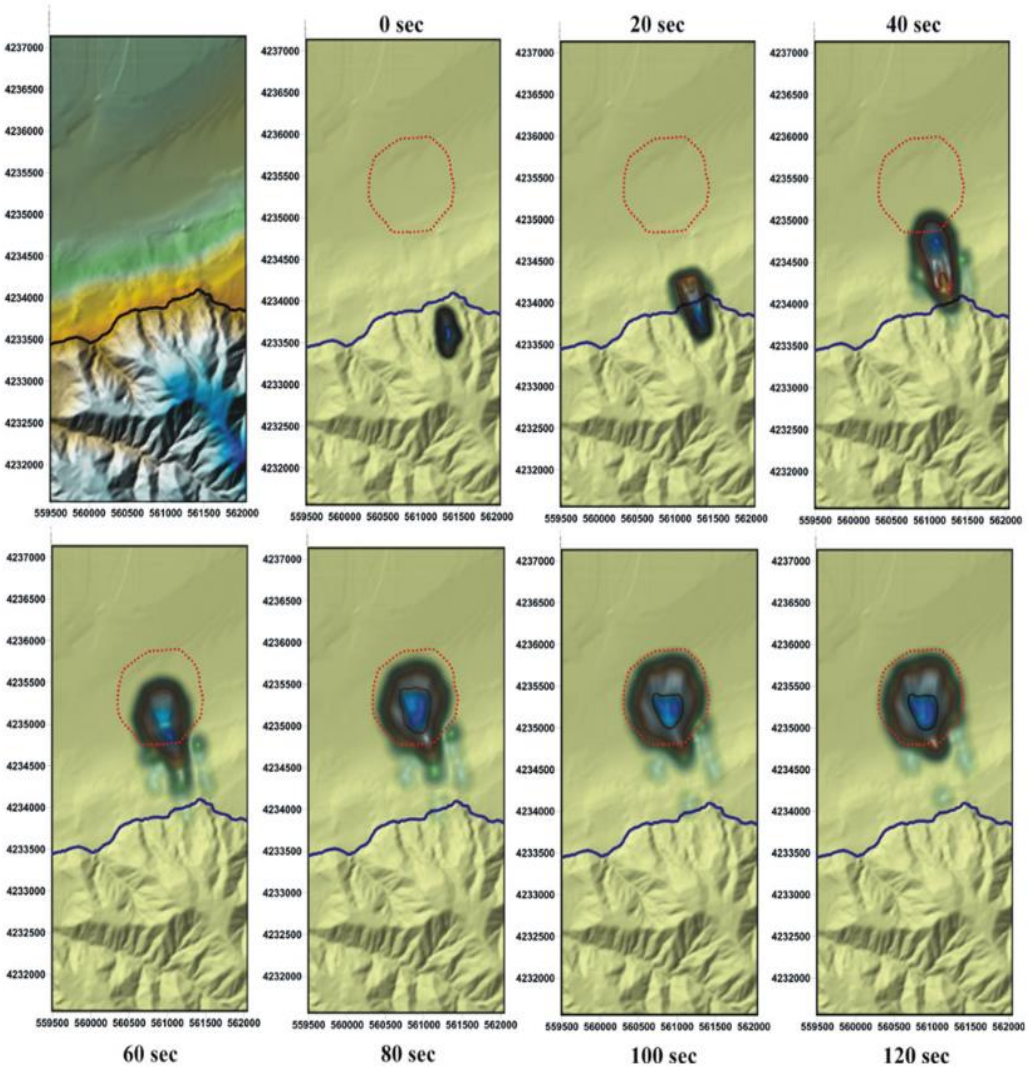

Fig. 2.11 Time sequence of the landslide propagation (plan view). Thered dotted linebounds the real mapped landslide deposit(Mazzanti and Bozzano, 2011).

A maximum landslide velocity of 45 m/s is reached about 15–20 s (Fig.2.12) after the failure in the frontal part of the mass (in the submarine slope). Then, the moving mass maintains a velocity greater than 40 m/s until 30 s that decreases below 20 m/s after 60 s from the collapse. After 70–80 s, the mass moves at a rate lower than 10 m/s. Historical documents testify to an intense 30 s long noise coming from Monte Pacı` before the arrival of the tsunami (Minasi,1785).

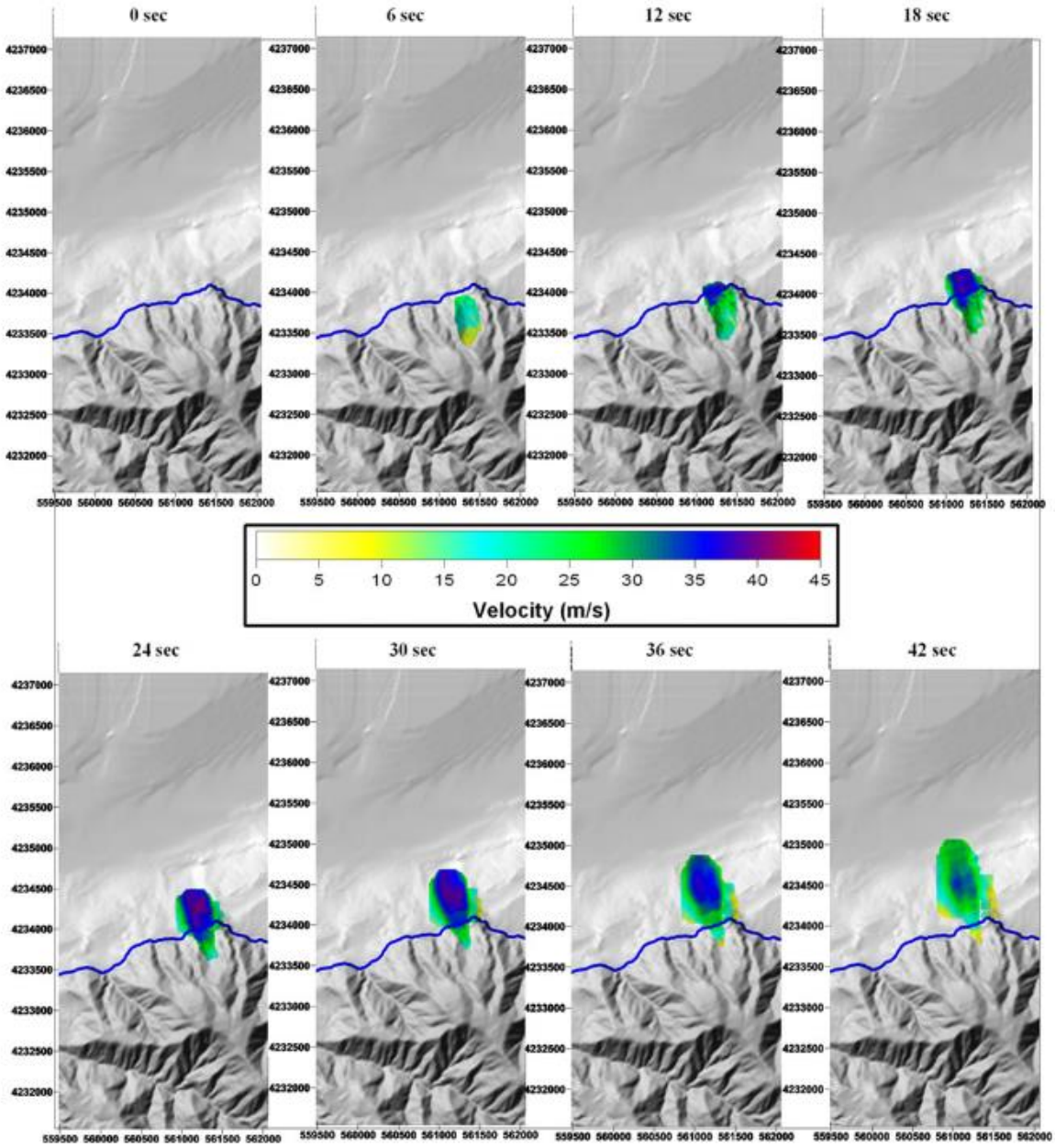

Fig. 2.12 Time sequence of the landslide velocity distribution during the first 42 s of numerical simulation(Mazzanti and Bozzano, 2011).

Figure 2.13 shows time series of the thickness in the first 42 s of the simulation. The thickness is reduced from the initial value (higher than 60 m) down to 40 m during the first 18 s and between 20 and 25 m in the submarine slope during the first 42 s. These thickness values refer to the frontal part of the moving mass. A similar behavior has also been observed for the velocity (Fig. 2.12); in this case, the highest values were recorded just behind the frontal part of the moving mass.

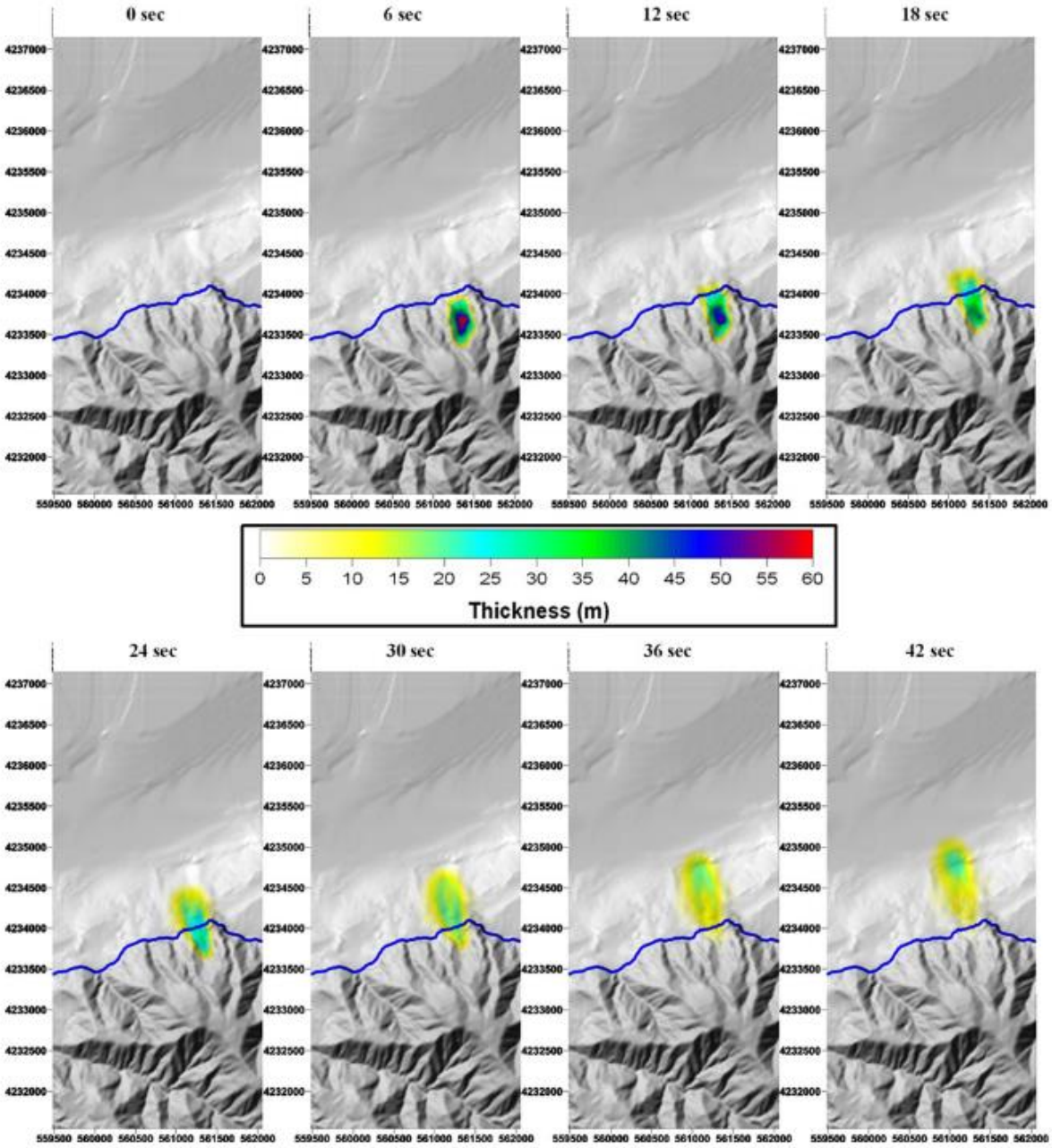

Fig. 2.13 Time sequence of the landslide thickness distribution during the first 42 s of numerical simulation (Mazzanti and Bozzano, 2011).

Zaniboni et al. (2016) reconstructed the geometry of the slide by filling only the subaerial scar, following the Mazzanti and Bozzano (2011) hypothesis, they simulated the slide motion by using the observed deposit as a constraint to calibrate the code parameters; they coupleed the slide and the tsunami by computing the tsunamigenic impulse produced by the landslide; they computed the

tsunami propagation and the tsunami inundation in Scilla by means of a nonlinear shallow-water model, and they compared model outcomes to the observations available from historical records. They restricted their attention only to the tsunami propagation very near to the source, where it had the main catastrophic effects killing more than 1500 persons.

The investigation of the 1783 event followed an already well-tested scheme: after the reconstruction of the initial geometry of the landslide body and of the sliding surface, the overall dynamic process is computed by means of a chain of three numerical codes.

First, the motion of the mass along the slope is simulated by means of the code UBO-BLOCK1. Then an intermediate auxiliary code, UBO-TSUIMP, is used to calculate the time-dependent source of the tsunami from the underwater landslide motion. Eventually the generation, propagation and impact of the tsunami are computed by using the simulation model UBO TSUFD.

In order to simulate the slide and tsunami events, a detailed reconstruction of the morphology of Mount Pacı` flank where the slide took place is required as well as of the topography and bathymetry of the area object of investigation. In this paper, the attention is focused on the village of Scilla, especially on the beaches of Marina Grande and Chianalea, where the most catastrophic effects of the tsunami were observed and reported. The topobathymetry of the area has been obtained by matching data from SRTM database for land morphology, from GEBCO and some nautical charts provided by the IIM (Italian Navy Hydrographic Institute) for the bathymetry.

The computational grid includes some kilometers of coastal stretch of the Tyrrhenian Calabria around Scilla, covering an area of 4 x 4.5 km, that for the tsunami simulation is partitioned in 10 x 10 m cells (see Fig. 2.14). The gray-shaded area of Fig. 2.15 represents the sliding surface. It comprehends the subaerial scar uphill that is well evident even now, and enlarges in the sea, since it includes the observed deposit (magenta dashed line).

The geometry reconstruction of the slide follows the Mazzanti and Bozzano (2011) hypothesis of a subaerial sliding body collapsing into the sea, without involvement of a submarine portion. The subaerial scar has been simply ‘‘filled’’ by extending the outer altitude isolines inside the sliding boundary. In this way, a volume of about 6.4 Mm^3 has been obtained, covering an area of 144.000 m^2 up to the crown placed at over 400 m a.s.l. (Bozzano et al. 2011) for a mean thickness of around 44 m. As can be seen in Fig. 2.14, the slide is about 100 m thick uphill and thinner seaward.

A further input for the code is the predefined trajectory of the center of mass of the slide blocks (dark blue line in Fig. 2.14).

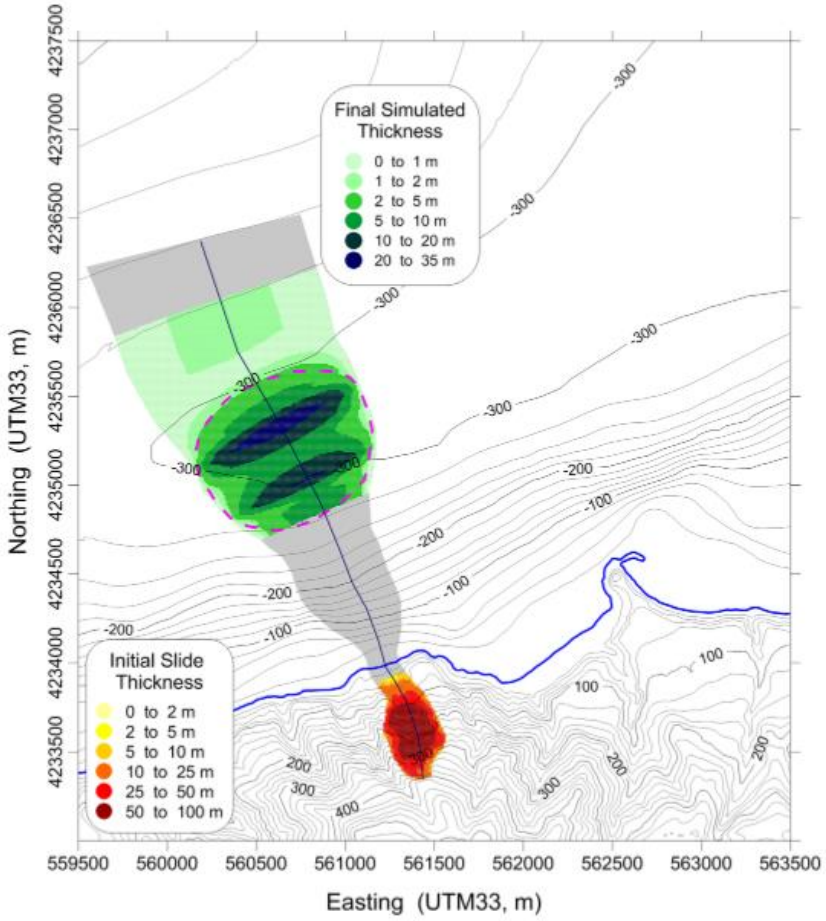

Fig. 2.14 Topography and bathymetry of the simulation computational domain (coordinates expressed in WGS84-UTM, zone 33 N). The initial slide thickness is depicted with a yellow-red palette. The sliding surface is portrayed in light gray. The central dark blue line is the predefined trajectory of the center of mass of the blocks forming the slide. The simulated final deposit is represented in different green tones and refers to the simulation with friction coefficients providing the best misfit. Notice that the most massive part of the simulated slide stops inside the boundary of the observed deposit (magenta dashed contour) (Zaniboni et al., 2016).

The landslide motion has been computed by means of the code UBO-BLOCK1 that requires the specification of parameters governing the interaction between the slide and the environment (e.g. friction coefficient, front and surface drag) and the internal interaction (influencing the degree of slide deformation). The observed deposit, detected in the marine surveys at about 300 m b.s.l., is about 3 Mm^3 in volume (Bozzano et al. 2011), which is only 50 % of the sliding body.

This suggests that the missing part consisted of loose material that was produced by slide fragmentation and removed by the strong coastal currents coming from the Messina Straits

(Bosman et al. 2006). The parameters of the landslide simulation code have been calibrated by optimizing the fit between the observed and simulated deposits. To highlight the procedure, they report the results of a sensitivity analysis carried out on the bottom friction coefficients.

They have varied the subaerial friction coefficient μ_{SA} and the submarine friction coefficient μ_{SM} by steps of 0.01, respectively, in the intervals 0.02–0.45 and 0.02–0.20, which are typical ranges for onshore and offshore landslides (see Legros 2002).

All possible combinations of $\mu_{SA} - \mu_{SM}$ have been taken into account, for a total of 836 runs.

The similarity between the calculated and observed deposits has been measured by means of a misfit parameter introduced by Zaniboni and Tinti (2014) and adapted here to measure superposition of areas. They investigated the 1963 Vajont landslide; this event is well known and was the object of numerous technical and scientific studies, especially in the two decades following the disaster. They proposed a re-examination of the matter, focusing on the numerical modelling of the landslide, and is carried out by using a 1D numerical code based on a Lagrangian approach. The model is properly conceived for cases with slide length prevailing on width. When the slide width is comparable or prevailing on length, as is the case of the Vajont slide, the mass is first partitioned into a number of longitudinal long and narrow sub-slides. The Vajont mass was subdivided into six strips and the motion of each sub-slide was computed. The knowledge of the final deposit position allowed them to constrain the value of some relevant parameters characterizing the slide motion, the most interesting being the friction coefficient μ, that they varied in order to obtain the best-fit between calculated and observed deposits. Taking into account the additional constraint that all sub-slides move with the same or at least with similar speed, and introducing a global misfit based on deposit and velocity misfits, they were able to show that solutions minimizing the global misfit exhibit a relevant difference between the basal friction coefficients of the western and of the eastern sides of the sliding surface, with the former being significantly smaller (0.14–0.16) than the latter (0.32–0.34). The smaller is the misfit, the better is the agreement between the simulation and the observation. Due to the observed deposit lack of mass, mentioned above, they decided to measure the similarity of the two deposits considering only the thicker portion of the simulated slide, i.e., the one exceeding 2 m.

Figure 2.15 summarizes the results, with the yellow star marking the couple of values providing the least misfit, i.e., $\mu_{SA} = 0.23$ and $\mu_{SM} = 0.06$.

Looking at the misfit trend, one can see that (1) there is a strong dependence of the simulation accuracy on μ_{SM}, and much less on μ_{SA}, suggesting that the final landslide position is mainly governed

by the underwater motion phase; (2) in the misfit absolute minimum and in the nearby region, μ_{SM} is much lower than μ_{SA}, confirming a feature that is frequently reported in the literature (see for example, Masson et al. 2006).

Moreover, if we consider the 5 % cases with the lowest misfit, they find that μ_{SM} has the mean value 0.06, with a standard deviation of 0.004, while μ_{SA} ranges 0.20 ± 0.09, with an almost 50 % spread. Consistently with our sensitivity analysis, we have selected the least-misfit friction coefficient combination (μ_{SA} = 0.23 and μ_{SM} = 0.06) for the landslide simulation code. With this choice, the simulated deposit isopachs are shown in Fig. 2.15: a maximum thickness of less than 30 m is found, and less than 5 m on average, with a thinner sheet (<2 m) lying farther in deeper water, in good agreement with the observations (Bozzano et al. 2011).

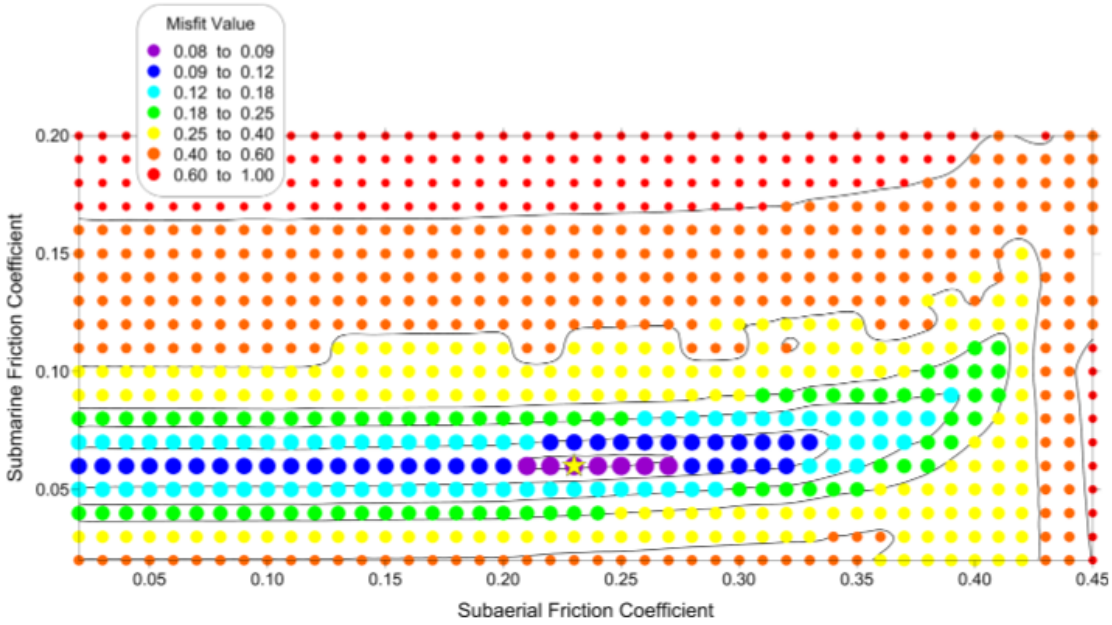

Fig. 2.15 Computed misfit for different combinations of subaerial and submarine friction coefficients. The color scale marks the values, with purple and blue denoting the μ_{SA} – μ_{SM} *pairs providing the least misfit between the simulated and the observed deposit (Zaniboni et al., 2016).*

The calculated mean velocity of the slide blocks vs. time is plotted in Fig. 2.16. A fast acceleration phase is observed first, which is typical of coastal collapses where the mass moves initially along steep slopes. Within 17 s the sliding mass reaches the peak speed of about 35 m/s (red line, Fig. 2.16); then, it decelerates gently.

The black-circle lines are the time histories of the individual blocks' velocities. In the acceleration phase, the mass is compact, all blocks moving approximately with the same speed. Velocities become different when blocks start interacting with water, which occurs between 10 and 30 s, as the effect of buoyancy, drag and bottom friction forces. The landslide simulation is stopped after 110 s, when the mean velocity becomes less than a predefined threshold. Such findings are not dissimilar from the results by Mazzanti and Bozzano (2011).

The blue line of Fig. 2.16 is the plot of the Froude number (Fr) vs. time. By definition, Fr is the ratio between the horizontal velocity of the portion of the slide that is underwater and the phase velocity of the wave, that in the shallow-water theory equals $\sqrt{gh}$ (with g = gravity acceleration and h = sea depth). When this value is close to 1, the mass and the wave move with the same velocity and the tsunami generation process has the highest efficiency; in supercritical (mass faster than wave) and subcritical (mass slower than wave) regimes, the tsunami excitation is less efficient. In cases like the 1783 collapse, the slide starts moving out of the water (so no Froude number is computed) and when it penetrates into the sea, its velocity exceeds by far the tsunami phase velocity.

Therefore, Fr attains very high supercritical values. Soon later, since the mass starts to decelerate and the sea depth increases, the two velocities come closer to one another and Fr reaches the critical unit value, which occurs at about 27 s (Fig. 2.16). This instant does not correspond to the instant of velocity peak in the velocity time history. For larger times, the motion is subcritical: the Froude number keeps decreasing, since the wave travels faster and faster (in deeper sea) and the mass slows down on flatter sea floor. In Fig. 2.16 we have also superposed triangles to the Froude number curve to show the instants when the blocks enter the water.

Each time the COM of a new block reaches the sea, a new higher contribution is added to the computation of the Froude number (due to high velocity of the CoM and low depth, both factors producing high Fr value), which causes some perturbation in the curve. On the contrary, when all blocks move underwater, Fr decreases with a regular trend.

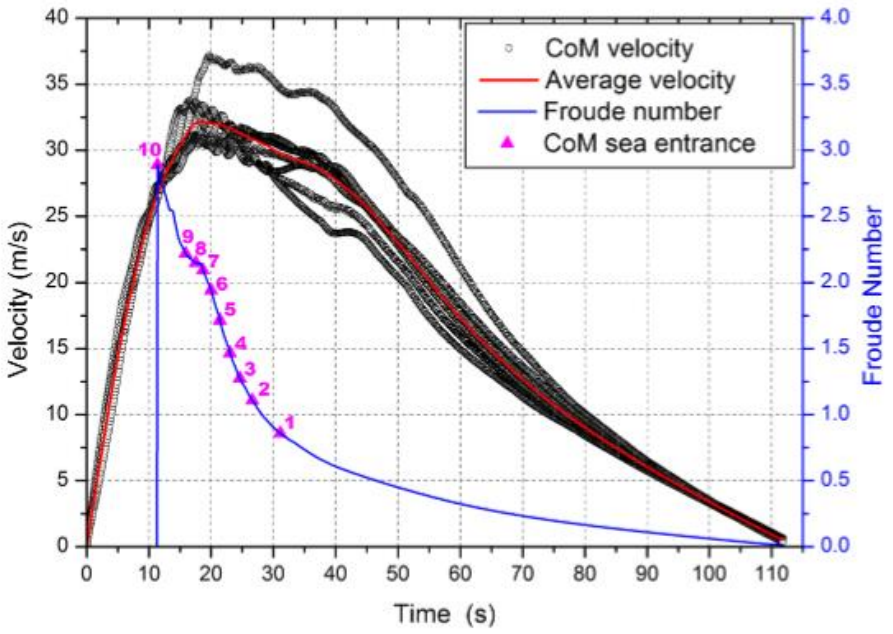

Fig. 2.16 Mean velocity (red line), CoM velocity (black circles) and Froude number (blue line) time histories. The Froude number is computed in terms of the average velocity and average depth of the underwater blocks .Magenta triangles mark the instants when block n enters the water. The velocity peak occurs at17 s. The Froude number curve crosses the critical value around 27 s (Zaniboni et al., 2016).

Zaniboni et al. (2019) using the simulation of the sliding motion of Zaniboni et al. (2016) showed the acceleration and velocity of the CoM of the landslide blocks (black dots) (see Fig. 2.17) as a function of the distance along the profile, together with the average values (green line). The initial positive acceleration phase, with values around 3 m/s^2, is limited to the subaerial part of the motion (the first 700 m of the profile approximately), while, once underwater, the acceleration adjusts around slightly negative constant values, entailing a slow uniform deceleration phase.

This is confirmed by the velocity profile: the average velocity peak is reached just before the entrance of the mass into the water. All the CoMs have a similar velocity evolution with distance. The mass has an initial length of around 700 m. For most blocks, the runout is about 2 km, with the exception of the frontal one that travels more than 2.2 km, which results in a lengthening of the slide by about 200 m.

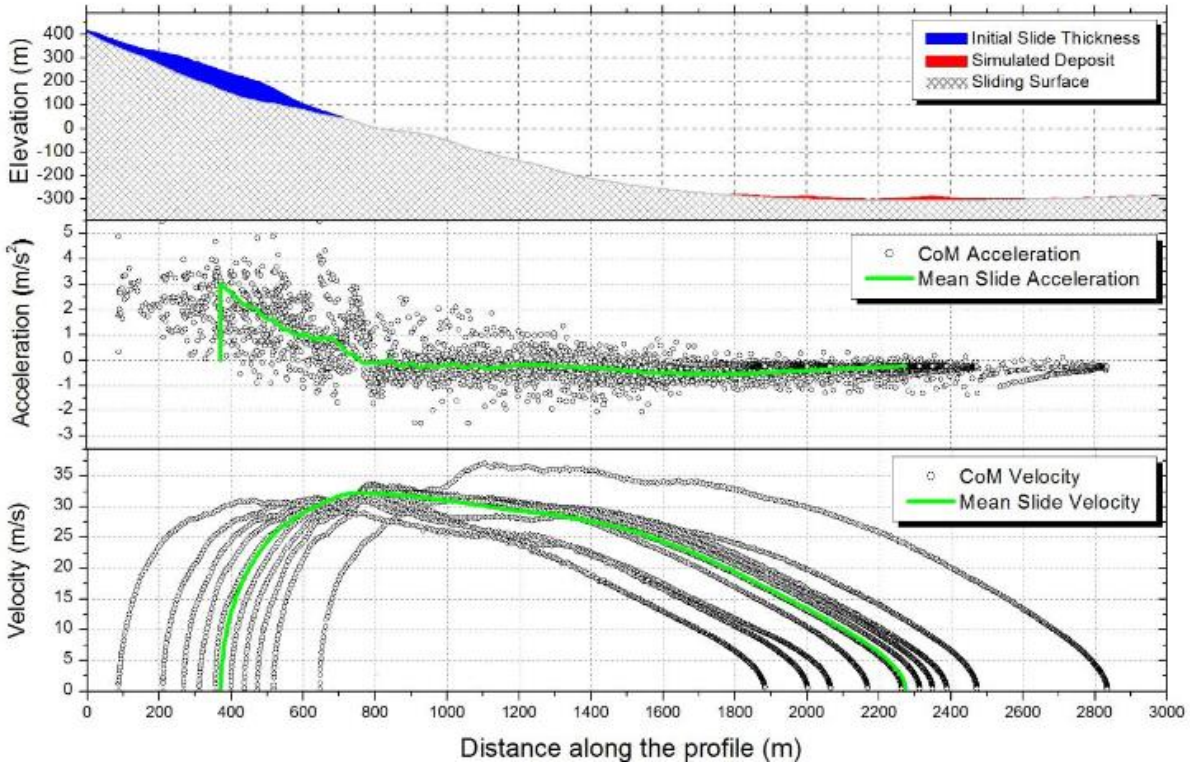

Fig. 2.17 Scilla 1783 slide simulation by means of the code UBO-BLOCK1. Upper Panel) profile of the initial sliding body (in blue) and of the final simulated deposit at about 300 m depth (in red) over the undisturbed sliding surface (grey area). Middle panel) acceleration of the individual CoMs (black circles) and of the CoM of the whole slide (green line) vs. distance along the sliding profile. Lower panel) CoM velocities (black dots) and average velocity (green line) plotted on the sliding track distance (Zaniboni et al., 2019).

2.2.2 The catastrophic tsunami

Mazzanti and Bozzano (2011) performed the Numerical modelling of the 1783 Scilla tsunami with a linear shallow water model, which was applied to both tsunami generation and propagation as described by Harbitz and Pedersen (1992). In this model, the landslide is simplified and described as a flexible box with a pre-defined velocity progression.

The dimensions of the box are defined by the physical extensions of the slide and are given as input to the numerical model (length, width, and height). The box is rounded to avoid numerical noise due to sharp edges, and the landslide propagation follows a straight line. The travel distance of the slides(t) at time t describes an acceleration phase, a constant speed phase, and a deceleration phase:

Acceleration phase:

$$s(t) = R_a\left(1 - \cos\left(\frac{U_m}{R_a}t\right)\right), 0 < t < T_a \quad (2.1)$$

Constant speed phase:

$$s(t) = R_a + U_m(t - T_a),\ T_a < t < T_c + T_a \quad (2.2)$$

Deceleration phase:

$$s(t) = R_a + R_c + R_d \sin\left(\frac{U_m}{R_d}(t - T_a - T_c)\right),\ T_c + T_a < t < T_a + T_c + T_d \quad (2.3)$$

Where U_m is the maximum slide velocity, T_a is the acceleration time, R_a is the acceleration distance, T_c is the constant speed time, R_c is the constant speed distance, T_d is the deceleration time, and R_d is the deceleration distance. The total travel time is $T=T_a+T_c+T_d$, while the run-outdistance of the slide is $R=R_a+R_c+R_d$. Further details on the landslide representation can be found in Harbitz (1992) and Løvholt et al. (2005). The model is validated among others against observations of the catastrophic 1934 Tafjord rock slide tsunami event, Western Norway (Harbitz et al.1993).

The following input data were used in the tsunami simulation based on the available dataset and the aforementioned analyses (Table 4).

Landslide geometry				
Length (m)	Width (m)	Height (m)	Assumed volume[a] ($10^6 \times m^3$)	
700	280	25	5.4	
Landslide dynamics				
Acceleration length (m)	Constant speed length (m)	Retardation length (m)	Max. velocity (m/s)	Run-out distance (m)
350	350	1,000	45	1,700

[a] The volume of the landslide is slightly larger than the product of length, width, and height owing to a rounding of the slide box to avoid numerical instabilities

Table 4 *The landslide features used in the tsunami modelling (Mazzanti and Bozzano, 2011).*

The DTMM (Digital Terrain and Marine Model), achieved by combining high resolution multibeam bathymetry with a grid spacing of 20 m in the nearshore(merged with a 100 m-grid bathymetry in the offshore) has been used as the topography for the simulation. Landslide propagation features

have been inferred by detailed field surveys, geophysical landslide investigations and in particular by the landslide numerical simulation.

Specifically, in order to apply the simplified tsunami model to the 1783 Scilla landslide, the 3D landslide geometry during the propagation achieved by DAN3D simulation (Fig. 2.13) have been converted into a non-deformable block (Fig. 2.18), the size and thickness of which were as representative as possible for the simulated landslide geometry during the early stages of the submerged propagation (the most important phases in the tsunami generation).

With regard to the velocity a simplified profile with a constant acceleration phase, a constant velocity phase and a constant deceleration phase has to be achieved from the landslide simulation performed by DAN3D (Fig. 2.12); this profile should represent the best approximation of the simulated landslide velocity distribution for tsunami modelling purposes (Fig. 2.18).

Furthermore, the Froude number analysis described above, was also performed with the aim of achieving a combination of thickness and velocity so that the non-deformable block had the ''equivalent'' tsunami-genic power as the simulated landslide (i.e. the thickness and velocity should be comparable over the time of critical Froude number conditions).

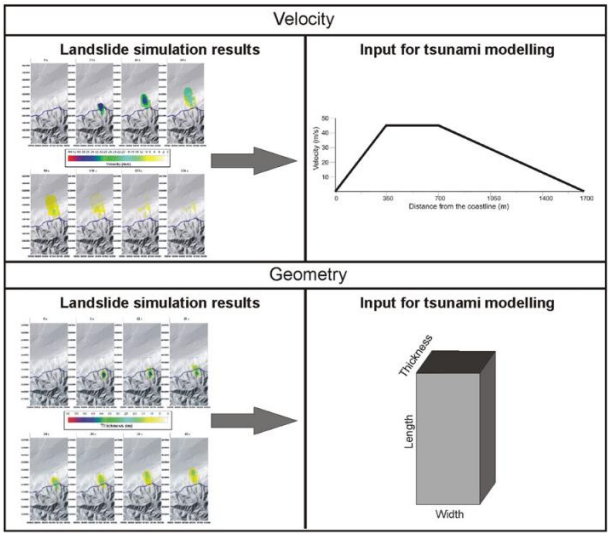

Fig. 2.18 Sketch explaining how the landslide simulation results (in terms of velocity and geometry) are converted in order to be used as input parameters for the tsunami modelling (Mazzanti and Bozzano, 2011).

Simulation results consist of 2D maps of the wave distribution in the investigated area and time series of wave elevation over time at specific points (gauge points) which are showed in Fig. 2.19.

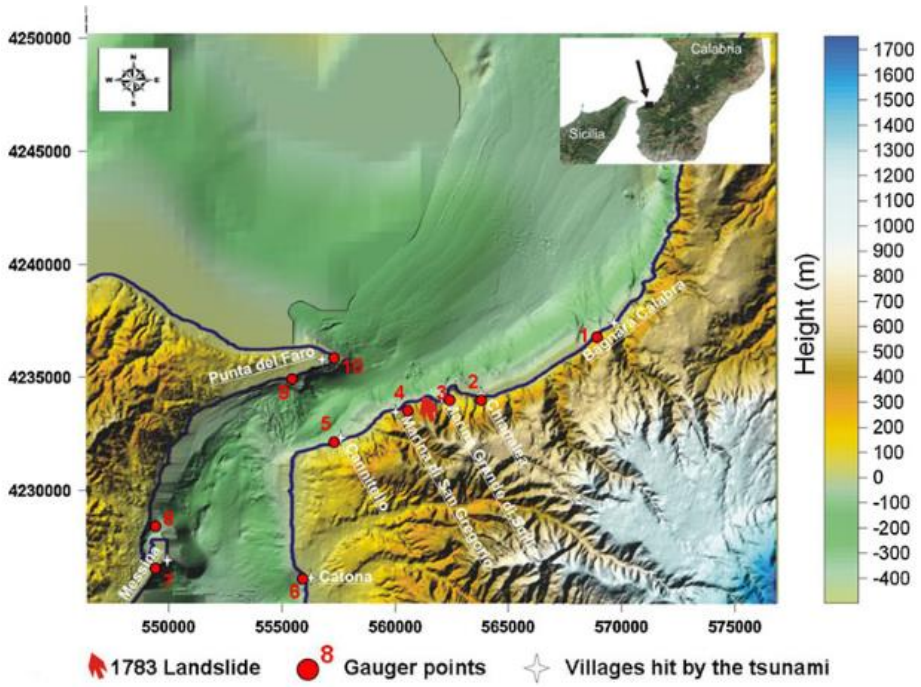

Fig. 2.19 DTMM (Digital Terrain and Marine Model) of Southern Calabria and the sector of Sicily overlooking the Messina Straits with indicated the location of the 1783 Scilla landslide, the villages affected by the Tsunami and the gauge points used in the tsunami simulation (Mazzanti and Bozzano, 2011).

For each location there are three gauge points (at depths of 100, 50 and 20 m) in order to monitor the amplification of the wave towards the coast. The perimeters of the landslide at the start and end positions are drawn in yellow and white, respectively. Figure 2.20 shows pictures of the surface elevation after 2, 5 and10 min, while Fig. 2.21 shows the maximum surface elevation during the first 20 min of simulation. The wave front starts to propagate radially from the landslide, with the highest waves in the sliding direction, i.e. perpendicular to the coast of Scilla.

After 5 min the wave front reaches the NE Sicily coast, and it moves along the coast of Calabria and Sicily. After 10 min the wave front approaches Bagnara Calabra, north of Scilla, (Fig. 2.19) and enters in the Messina Straits. One can observe reflection, refraction and interference effects in the wave pattern. The surface elevation in open water is about 6–8 m (Fig. 2.20).

The run-up values at the coastline were determined by using the simulated surface elevation of the highest wave of the leading part of the wave train. Here, the surface elevation at a depth of 100 m (before the wave starts to amplify due to shoaling) was used in the run-up calculations. Based on the run-up factors of non linear waves found in laboratory experiments (Pedersen and Gjevik 1983),

the run-up was determined by multiplying the measured surface elevation with these factors. The factor chosen depends on the bathymetric slope and varies from 2 (vertical slopes) to 5 (extreme cases with gentle slopes).

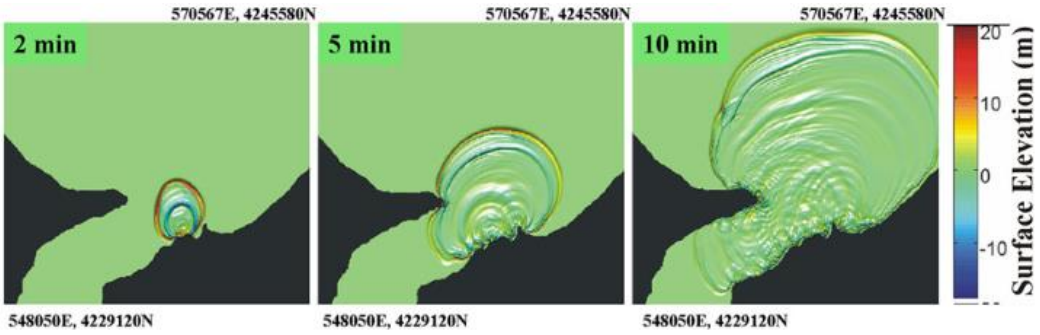

Fig. 2.20 Time sequence of the wave surface elevation during the first 10 min after the landslide occurrence (Mazzanti and Bozzano, 2011).

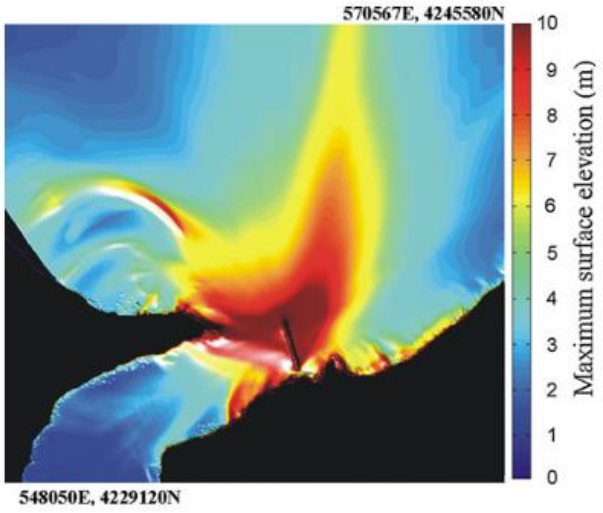

Fig. 2.21 Maximum surface elevation of the wave during the first20 min after the slide. Values higher than 10 m are reported as thedark red color (Mazzanti and Bozzano, 2011).

The bathymetric slopes offshore the selected locations (Fig. 2.19) are characterized by average inclination angles from 100 m of depth to the coastline from 6°to 19° (Table 5). The factors were reduced for locations close to the landslide, where the amplification was weaker due to waves propagating more parallel to the shoreline (NGI2008). In particular, for the location Punta del Faro 2, where a low-gradient slope is present from the coast to about 20 m water depth, the factor was further reduced since the model overestimates the waves in the areas in front of the slide for slides

moving with such high velocities (NGI2008). Estimates of run-up heights for the pre-scribed landslide volumes and velocity profiles are presented in Table 5 where the estimated values of the run- up height for each location are given as intervals to reflect the uncertainty in the calculation procedures.

Location ID	Location	Average inclination angle from 100 m depth (°)	Computed run-up interval (m)	Historically reported run-up interval (m)
8	Messina	19.1	1–2	2
7	Messina 2	6.7	2–3	2
6	Catona	9.0	About 1	0.3–0.7
3	Marina di Scilla	8.7	25–35	9–16
4	Marina San Gregorio	10.0	25–35	
5	Cannitello	12.9	6–8	0.8–2.9
1	Bagnara Calabra	8.2	7–9	
9	Punta del Faro	16.1	10–15	6–13
10	Punta del Faro 2	8.1	25–40	6–13
2	Chianalea	6.3	15–20	5–6

Table 5 *Run-up estimates for the locations in the study (Mazzanti and Bozzano, 2011).*

Zaniboni et al. (2016) simulated the generation and propagation of the tsunami by the finite difference code UBO-TSUFD (Tinti and Tonini 2013) solving frictionless nonlinear shallow-water equations with a staggered-grid technique and dynamic boundary conditions at the coastal lowing flooding computations. Figure 2.23 shows the propagation fields in the initial 90 s of tsunami life that starts when the landslides enters the sea water, at 10-s intervals. A first semi-circular front is evident in the 20 and 30 s plots, corresponding to the landslide (in green) entering the water.

A positive wave signal is generated (yellow to red scale) that moves together with the sliding mass at least for the first 30–40 s. Later, the main wave front travels faster than the mass and the resonance condition falls. The tsunami attacks the Marina Grande beach about 60 s after the slide initiation. This is in perfect agreement with the reconstruction by Minasi (1785), reporting 30 s of intense long noise preceding the tsunami that arrived within 1 min. Here, the wave front, about 4 m high and almost parallel to the coast, attacks first the western side of the beach.

Within 10 to 20 s, the whole beach, where most of the Scilla people were escaped after the earthquakes, is flooded by waves that reach areas at 6 to 10 m elevation (red areas in Fig. 2.22). The simulations show also a negative front, meaning sea withdrawal, following the first positive signal and with about the same magnitude, and further crest sand troughs, propagating mainly along the coast.

This suggests a trapping of the tsunami energy in the near-shore zone. At about 80 s, the tsunami positive front crosses the harbor pier (not existing in 1783), heading eastward toward the Chianalea hamlet.

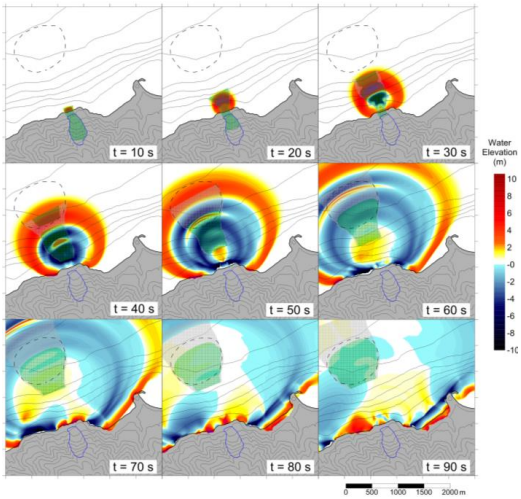

Fig. 2.22 Propagation fields of the 1783 tsunami, given every 10 s. Sea level positive (negative) elevation is reproduced with a yellow-red (cyan-blue) palette. In each snapshot, the instantaneous position of the slide with thickness larger than 2 m (less than 2 m) is reported in green (gray) and the observed deposit in dashed black (Zaniboni et al., 2016).

The computed maximum water elevation is depicted in Fig. 2.23a. One may observe that the highest water elevation is found just in front of the source, decreasing with distance. Moving eastward, run-up heights from 6 to 10 m can be noticed in the Marina Grande beach and in the cliffs under the Scilla Castle. The pier provides a good protection for the harbor reducing maxima significantly. Continuing to east of the harbor, toward Chianalea, a higher tsunami beam is clearly visible, about 4–5 m high. In general, with the exception of the Marina Grande beach and Chianalea, the tsunami penetrates only a few tens of meters inland all along the coast included in the computational domain, due to the steep morphology.

Panel b of Fig. 2.23 focuses on Marina Grande, where most of the historical reports are available. The western side is the first to be attacked by the tsunami that climbs up to 7 m height at its end. In correspondence of points 1 and 2, the agreement between simulation results and the reports by Sarconi (1784) is very good. The simulated tsunami reaches 5 m in point 1 (see Table 6).

In node 2, where Santa Maria delle Grazie church was reported to be inundated and seriously damaged by the waves, the tsunami exceeds 6 m. On the eastern part of the beach, points 3–5 are subject to more severe inundation, which fits very well with the observations (Table 6).

Point 5 corresponds to the Santo Spirito church that was destroyed by the tsunami.

At point 6, where the Prince's house was located, the waves reach almost 7 m and where the tsunami impacts the cliffs of Scilla castle they are even higher. What is missed in our simulation is the sea inundation along the Livorno stream (point 7) that is largely underestimated (95 vs. 200 m, see Table 6). This is probably due to the fact that the present morphology (on which the computational grid is built) differs substantially in this area from the one of 1783. Now the small river is buried and covered by a coastal road, while in the past the riverbed was probably lower, facilitating water ingression.

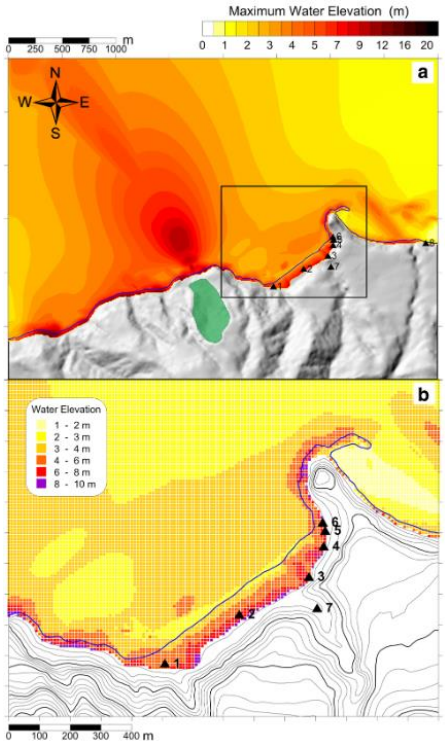

Fig. 2.23 ***a*** *Maximum sea surface elevation. The green area is the initial landslide position. Places with tsunami observations (see Table 6) are marked by black triangles.* ***b*** *Zoom over the Marina Grande beach [delimited by th eblack rectangle in (a)] (Zaniboni et al., 2016).*

No.	Toponym	Run-up (m)		Inundation (m)	
		Observed	Simulated	Observed	Simulated
1		5.2	5.4		50
2	S. Maria delle Grazie church		6.7	90	80
3	S. Nicola church	> 5	6.5	100	100
4	Gornelle's fountain	8.3	8.9		75
5	S. Spirito church	8	7.6	40	35
6	Prince's house	6.2	7.2		30
7	Livorno stream		9.0	200	95
8	Chianalea	3.5	3.3		9

Nodes from 1 to 7 are located to the west of the Scilla promontory, at the beach of Marina Grande. Node 8 is to east of the today Scilla harbor

Table 6 *Number and toponyms of the places where tsunami run-up heights and inundation distances are available from historical reports (modified after Graziani et al.2006) compared with the respective values obtained in the numerical simulations (Zaniboni et al., 2016).*

A set of four virtual marigrams computed in near-shore locations is shown in Fig. 2.24.

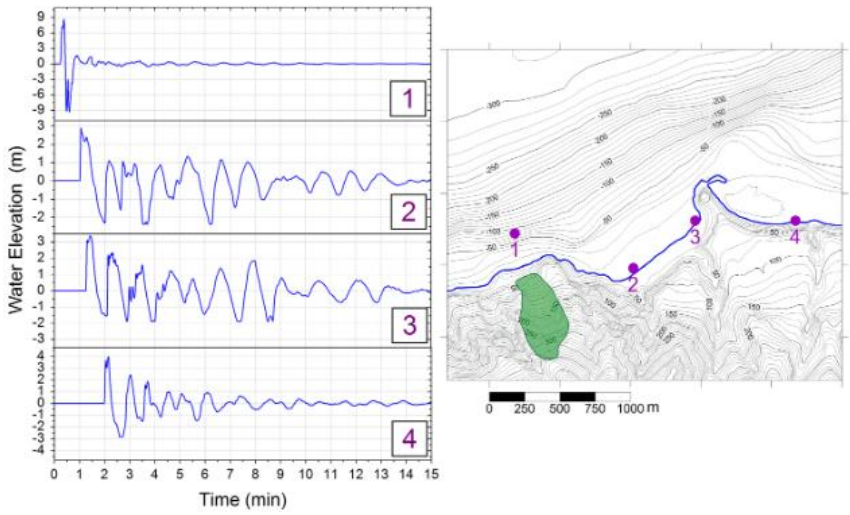

Fig. 2.24 Synthetic marigrams computed in four different locations shown in the right map as purple circles. The green area shows the landslide initial position (Zaniboni et al., 2016).

The first is placed just in front of the zone where the slide enters into the water. The time history displays a dipole-like perturbation of the sea surface. As already observed in commenting the propagation fields of Fig. 2.22, the first signal is positive (almost 9 m), followed by a slightly stronger trough (about 9 m) and then by lower oscillations (less than2 m).

Marigrams 2 and 3 depict the tsunami behavior at the two western and eastern ends of the Marina Grande beach. As already observed, the western side is affected by lower waves (less than 3 m) than the rest of the beach (over 3 m). A series of 3 relevant waves with crest-to trough height in excess of 3 m and a period of 1 min is followed by further 4 relevant oscillations. This rapid sequence of strong waves can be considered responsible for the high run up and for the catastrophic effects on population and buildings.

The tsunami continues to affect the shore for at least 15 min (final time of simulation for this small domain). In the place of marigram 4, located at a larger distance from the source, the tsunami attenuates more quickly. Here, in the area of Chianalea, the first tsunami wave reaches almost 4 m height, fitting the historical reports (Tinti et al.2007a). As regards the simulated period of 1 min, it is worth noting that this is not very different from the 90 s period that was both measured and simulated for the 2002 Stromboli tsunami, induced by a landslide with volume about 2–3 times larger (see La Rocca et al.2004; Tinti et al.2005).

Zaniboni et al. (2019) extended the study also for the area of Capo Peloro and Punta Faro in Sicily by using the same numerical models both for landslide and tsunami simulation of the previous investigation (Zaniboni et al.,2016).

The first step of tsunami simulations is the assemblage of the computational grids, the area covered and the adopted grid resolution depending deeply on the goal of the simulation. In general, the higher the grid resolution, the more accurate are the results, but also the heavier is the related computational effort. T

The tsunami simulations in Zaniboni et al. (2016) were concentrated in the town of Scilla, and the extent of the very local regular mesh was of a few kilometers in length and width with 10-m spaced nodes (see Grid 1, in green, Figure 2.25). The purpose is two-fold, namely: i) to compute tsunami propagation on a wider area, involving tens of km of Calabria and Sicily coasts, and ii) to compute detailed inundation in the specific area of Capo Peloro, located in front of Scilla. For the first goal, they have built a lower resolution grid (50-m space step) denoted in Figure 2.26 in red as Grid 2, by using the SRTM database (for topography), the GEBCO dataset and nautical charts (for bathymetry). It covers an area of 30x27 km^2.

As concerns the Calabria coast, it runs from Bagnara, 10 km west of Scilla to Reggio Calabria, about 20 km south-westward. Regarding Sicily, the grid includes the city of Messina and 7-8 kilometers of coast southward as well as a piece of the northern coast facing the Tyrrhenian Sea by an extension of at least 10 km.

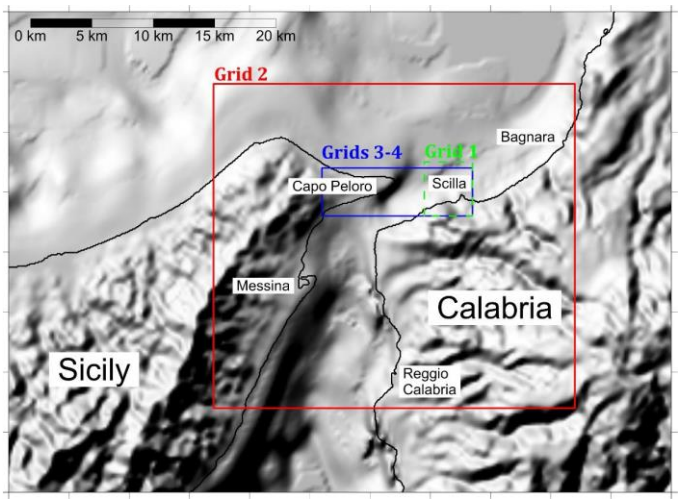

Fig. 2.25 Computational grids adopted for numerical simulation of tsunami propagation: Grid 1 (dashed green) was used for the tsunami simulations by Zaniboni et al. (2016); Grid 2 (in red) has been used in the first simulation of this paper; Grid 3 and 4 (in blue) are an extension of Grid 1 covering the target area of Capo Peloro (Zaniboni et al., 2019).

Figure 2.26 shows the maximum water elevation, obtained by considering the maximum value of the sea surface height reached during the simulation time span in each node of Grid 2. This category of plots provides a general spatial pattern of the tsunami energy distribution that, in the intermediate and far field depends more on the bathymetry than on the source type. Therefore, it allows one to distinguish the areas that are more prone to tsunami attacks.

The area close to the slide shows, as expected, the highest water elevations with more than 8 m in Scilla and waves at least 4 m high (in red) affecting the surroundings coast for about 6 km. The picture of Figure 2.26 provides also indications on the extension of the coast affected by 1.5-2 m (yellow), and 1 m wave (green), resulting in approximately 10 km and 20 km respectively along the Calabrian coasts.

South-westward, in the Messina Strait, maximum height ranges 0.5 m. Moving to the coast of Sicily, especially north of the Messina Strait, some significant features are observed.

First, a strong tsunami energy concentration can be noted towards the easternmost end of Sicily, named Capo Peloro, where waves higher than 6 m hit the coastline. Along the Tyrrhenian coast of Sicily other tsunami beams are clearly visible (in green, meaning at least 1 m heights), the most interesting of which is the western one, affecting the coastal stretch close to the small village of San

Saba. Overall, the simulation confirms the generally known feature that landslide-tsunamis wave height decays rapidly with distance.

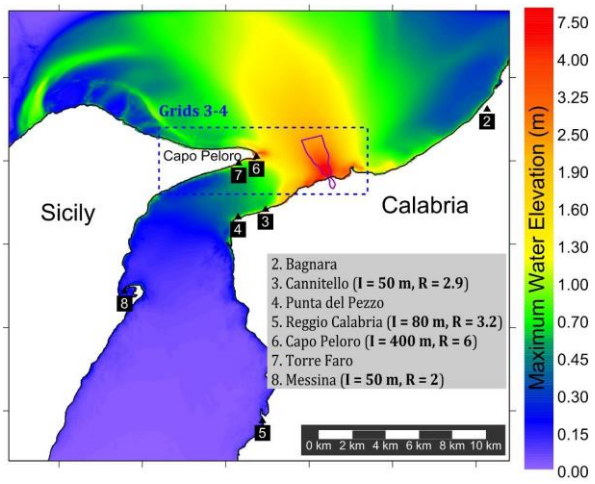

Figure 2.26. Maximum tsunami elevation, computed for each point of Grid 2. Numbers represent the positions of the available observations (see Table 2). The respective toponyms are reported in the legend together with the inundation distance (I) and runup (R). The blue dashed rectangle marks the limits of the 10 m resolution Grids 3 and 4, zooming on the area of Capo Peloro, that differ from one another only for a small part of their topography. The purple boundary delimits the sliding surface of the 1783 Scilla landslide (Zaniboni et al., 2019).

The characteristics of the different grids are summarized in the following table (Table 7):

GRID	Length (m)	Width (m)	Covered Area (Km^2)
Grid 1	10	10	4x2
Grid 2	50	50	30x27
Grid 3	10	10	12.5x4

Table 7 *Characteristics of the different grids described in the case study of Zaniboni et al. (2019).*

When comparing the simulation results with the observed effects a general underestimation can be noticed: for example, in point 3 (Cannitello) of the map of Figure 5 a runup of 2.9 m has been reported, higher than the 1 m maximum height obtained in the simulation.

The same holds for Messina (#8) and Reggio Calabria (#5), the most important towns in the Messina Strait, where the difference is by far bigger. Only the area of Capo Peloro (#6 and #7) seems to fit

the observations. Such discrepancies can be ascribed to the low resolution of the computational domain (50 meters) not allowing one to describe properly the coastal zone and all the non-linear effects prevailing in shallow water, such as the inland inundation.

Further, low-resolution simulations often cannot account for tsunami wave amplification caused by resonances induced inside coastal basins, such as harbors (see for example Dong at al., 2010; Vela et al., 2010). This latter can explain, for example, the underestimations of the observations reported in Messina and Reggio Calabria.

These considerations pushed to the use of a more detailed computational grid for the sites of major interest, suggesting that the optimal approach is: 1) to assess the general tsunami energy distribution in the first run of simulations carried out in a wider low-resolution domain 2) to pick up the areas most exposed to tsunami attack (e.g. areas hit by energy beams) to perform higher-resolution investigations.

With this approach, the focus has been moved to the area enclosed in the blue dashed rectangle of Figure 2.25, including Capo Peloro, where most of the devastating effects of the tsunami outside the source zone were reported (see Table 1, #6 and #7).

An additional computational grid (Grid 3) has then been built to simulate the tsunami propagation and inundation in this zone.

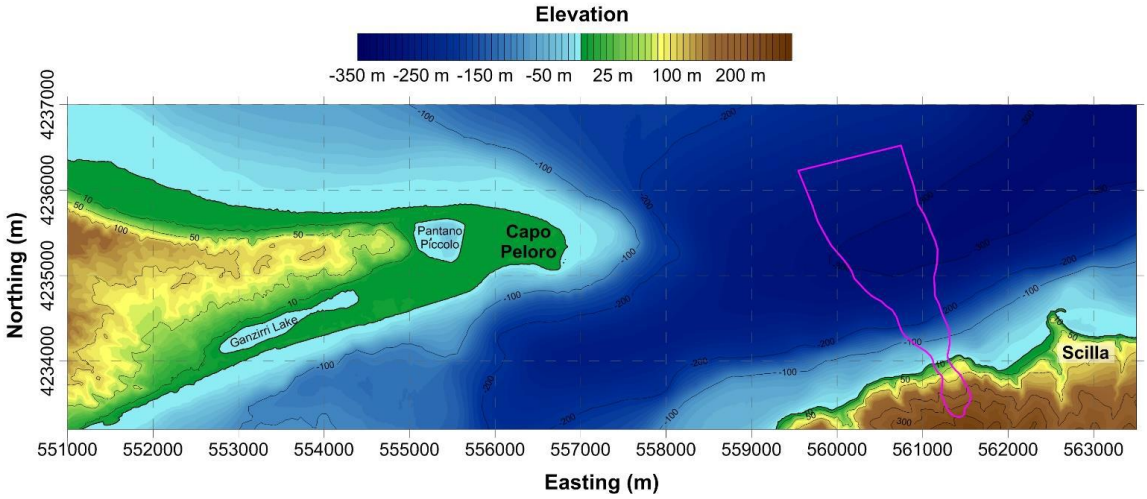

Fig. 2.27. Area covered by Grids 3 and 4 employed to simulate the impact of the 1783 tsunami in Capo Peloro, the easternmost point of Sicily. The magenta contour delimits the strip swept by the landslide (Zaniboni et al., 2019).

The choice was to build Grid 3 by extending westward the high-resolution grid (Grid 1, 10 m node spacing) used by Zaniboni et al. (2016) for the simulation of the local tsunami effects in Scilla. The relevant data for the Sicilian region was provided by the Civil Protection Department of Sicily and retrieved from the regional cartography service, SITR (Sistema Informativo Territoriale Regionale) in the form of a DTM describing the present topography of the coastal zone with high detail.

Grid 3 covers an area of 12.5 km (E-W) by 4 km (N-S), for a total of more than 500,000 nodes. As can be noticed from the map in Figure 6, the Capo Peloro presents a morphology that is radically different from the Calabrian coasts. If in Calabria coasts are steep, rapidly ascending to 400 m a.s.l., in the area of Capo Peloro a wide lowland is found, extending for about 2x1 km with elevation in the order of 1 to 5 meters.

This area is now densely inhabited, with many houses facing the sea especially along the southern coast. Another interesting feature is the presence of two brackish lakes, called Ganzirri Lake and Pantano Piccolo (also known as Faro Lake), characterized by maximum 6 m and 29 m water depth respectively.

They are connected to the sea (and to each other) by narrow channels, built under the English authority at the beginning of XIX century (Leonardi 5 et al., 2009; Manganaro et al., 2011; Ferrarin et al., 2013). One of the most relevant observations reported in the historical reconstruction of the tsunami effects is that the basin of Pantano Piccolo was reached by the sea water in 1783 (Minasi, 1785).

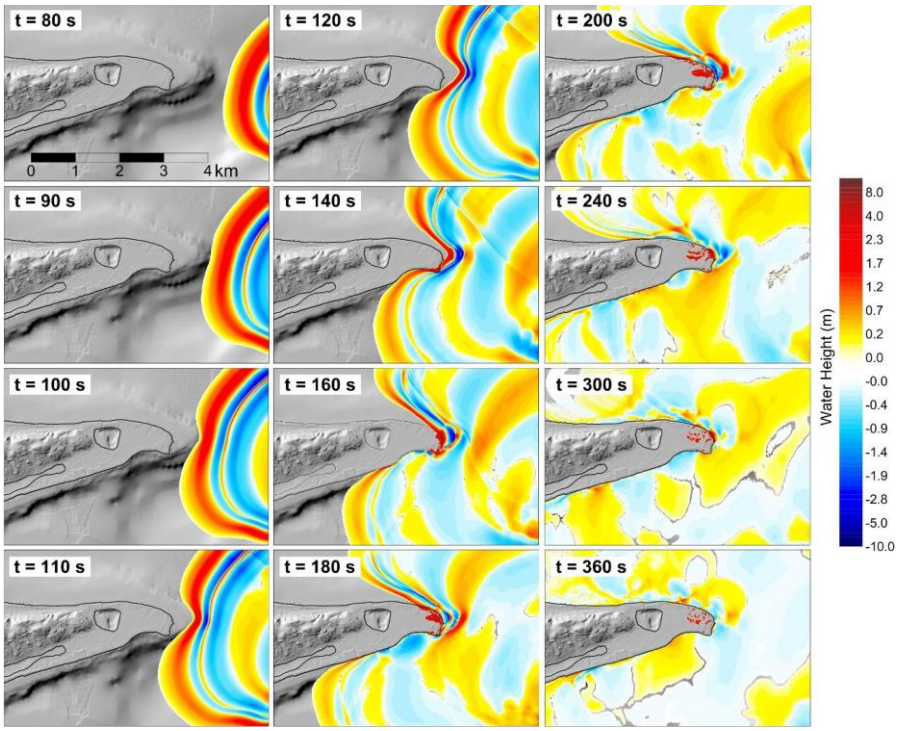

Fig. 2.28. Propagation frames for the 1783 Scilla landslide-tsunami in the target area of Capo Peloro, eastern Sicily (Zaniboni et al., 2019).

The landslide-generated wave heads towards Capo Peloro with a strong positive front 5 m high, directly originated by the slide entering the sea and characterized by an almost circular shape when moving in deep water.

At t=100 s the wave begins changing form, due to the interaction with the platform characterizing the seabed east of Capo Peloro. When meeting shallow water, the tsunami is intensely decelerated and begins to deform. Frames at 100 s, 110 s and 120 s display the subdivision of the wave into two fronts, north and south of the Capo Peloro end, attacking the coast obliquely.

At 140 s the southern coast of the cape is reached by the tsunami, that floods the mainland by some tens of meters. The eastern extreme of the area is reached only after, around 20 s later. Here the water penetration is maximum, reaching 600-700 m distance (as visible from 200 s frame). Contemporarily, the northern branch of the tsunami reaches the coastline with a positive 2 m high front that tends to align to a direction parallel to the shoreline.

The following oscillations constituting the train of waves (already visible behind the tsunami front in the first snapshots) do not produce relevant effects on the coast, apart from the cape, where a second relevant positive signal, exceeding 2 m, can be noticed at t=240 s.

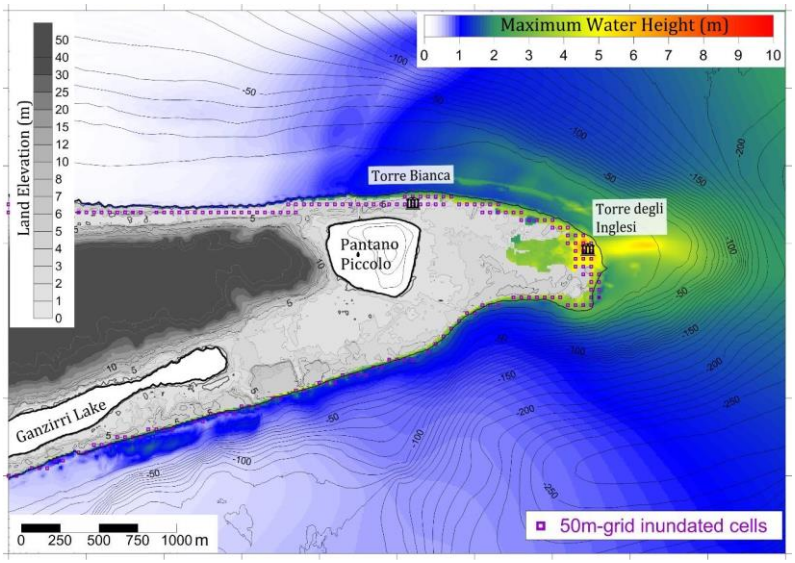

Fig. 2.29. Maximum water inundation in Capo Peloro for the high-resolution Grid 3 (western portion). The purple squares mark the cells inundated in the simulation with the low-resolution Grid 2. The black symbols represent the positions of historical buildings: Torre degli Inglesi, the site where tsunami deposits were recognized and associated with the 1783 event (Pantosti et al.,2008); Torre Bianca, partially buries by sand deposits (Bottari and Carveni, 2009) (Zaniboni et al., 2019).

The maximum water elevation for each node of the western portion of Grid 3 is reported in Figure 2.28. Some of the features already observed in the 50 m grid (#1) are confirmed, such as the maximum wave height concentration in the easternmost zone of Capo Peloro. Here, in correspondence with the edifice named Torre degli Inglesi ("English Tower", referring to a building realized during the English domination, marked in black in Figure 2.29), some tsunami deposits were recognized and associated to the 1783 event (Pantosti et al., 2008).

The simulation shows exactly for this spot the maximum water elevation, exceeding 6 m, and the maximum inland penetration, more than 700 m. Furthermore, here the main discrepancy between the low-resolution Grid 2 and the high-resolution Grid 3 can be noted: in the former case, only a few 5 inland cells (purple in Figure 2.29) are inundated (corresponding to an inundation distance of 150 m), while in the latter the inland penetration is by far larger.

For the remaining coastal stretch, the water flooding is limited to some tens of meters or less, showing little differences between the two simulations. It is very relevant to stress that, concerning the small lake of Pantano Piccolo, the simulations exclude that it is reached by the tsunami, contrary to what reported in the historical reconstructions.

3. SIMULATION SOFTWARE COMSOL MULTIPHYSICS

3.1 INTRODUCTION

COMSOL Multiphysics is a cross-platform finite element analysis, solver and multiphysics simulation software. When solving the models, COMSOL Multiphysics uses the proven *finite element method (FEM)*. The software runs the finite element analysis together with adaptive meshing (if selected) and error control using a variety of numerical solvers. The studies can make use of multiprocessor systems and cluster computing, and you can run batch jobs and parametric sweeps.

It creates *sequences* to record all steps that create the geometry, mesh, studies and solver settings, and visualization and results presentation. It is therefore easy to parameterize any part of the model: Simply change a node in the model tree and re-run the sequences. The program remembers and reapplies all other information and data in the model. Partial differential equations (PDEs) form the basis for the laws of science and provide the foundation for modeling a wide range of scientific and engineering phenomena.

COMSOL Server is a distinct software for the management of COMSOL simulation applications in companies. Several modules are available for COMSOL, categorized according to the applications areas of Electrical, Mechanical, Fluid, Acoustic, Chemical, Multipurpose, and Interfacing.

In this work, the interface equation-based model was used to perform the simulations , in particular *Coefficient Form PDE Interface (c).*

3.2 EQUATION-BASED MODELS

3.2.1 Mathematics Interfaces

The *mathematics interfaces* are physics interfaces for equation-based modeling. They support several PDE formulation as well as general ways of adding ODEs, algebraic equations, and other global (space-independent) equations. The following mathematics interfaces are found under the Model Wizard's **Mathematics** branch:

- *PDE Interfaces*. These are interfaces for solving PDEs in different forms:
  - *Coefficient form* for linear or almost linear PDEs, explained in detail in Coefficient Form PDE Interface (c).
  - *General form* for nonlinear PDEs, explained in detail in General Form PDE Interface (g).
  - *Weak form* using the weak formulation of the PDE for maximum flexibility. See Weak Form Modeling.

All of these PDE interfaces are available in domains and also on boundaries and edges and at points).

- *ODE and DAE Interfaces*. Use these interfaces to solve space-independent equations that include ordinary differential equations (ODEs), differential-algebraic equations (DAEs), algebraic equations, and transcendental equations, either as global equations or as distributed ODEs/DAEs (on domains, boundaries, edges, or at points). For more information about global equations and ODEs, see Solving ODEs and DAEs.
- *Events Interface*. This is a specialized interface to create solver events. For more information about using events, see The Events Interface.
- *Optimization*. This interface requires an Optimization Module license. See the Optimization Module User's Guide for details.
- *Sensitivity*. This interface is for Sensitivity Analysis.
- *Classical PDEs*. These specialized instances of the coefficient form PDE provide interfaces for a number of Classical PDEs.
- *Moving Interface*. The Level Set interface and the Phase Field interface provide the possibility to track fluid-fluid interfaces or other moving interfaces for multiphase applications, for example. See the Microfluidics Module or the Chemical Reaction Engineering Module documentation as moving interfaces require these modules.
- *Deformed Mesh*. The Deformed Geometry Interface makes it possible to model prescribed deformation of the mesh that represents the model domain. The Moving Mesh Interface is vital for modeling moving meshes using the ALE (arbitrary Lagrangian-Eulerian) technique in applications such as fluid-structure interaction (FSI).
- *Wall Distance*. This interface, which computes the distance to the boundary (wall), is primarily intended for use in connection to turbulence modeling for fluid flow.

3.2.2 Coefficient form PDE Interfaces (c)

The PDE interface (Δu) in coefficient form, *Coefficient Form PDE*, found under the Mathematics>PDE Interfaces branch (Δu) in the Model Wizard, covers many well-known PDEs. This section covers the formulation and settings pertaining to the coefficient form, as well as the general PDE terminology used in COMSOL Multiphysics.

When this interface is added, these default nodes are also added to the *Model Builder—Coefficient Form PDE, Zero Flux*, and *Initial Values*. Right-click the PDE node to add other nodes that implement other boundary conditions, for example. The following sections provides information about all nodes available in the Coefficient Form PDE interface.

The Coefficient Form PDE interface is also available as Coefficient Form Boundary PDE, Coefficient Form Edge PDE, and Coefficient Form Point PDE for PDEs in coefficient form on boundaries and edges and at points.

A single dependent variable *u* is an unknown function on the computational domain. COMSOL Multiphysics determines it by solving the PDE problem specified. In coefficient form, the PDE problem reads

$$
\begin{aligned}
& e_a \frac{\partial^2 u}{\partial t^2} + d_a \frac{\partial u}{\partial t} + \nabla \cdot (-c\nabla u - \alpha u + \gamma) + \beta \cdot \nabla u + au = f && \text{in } \Omega \\
& \mathbf{n} \cdot (c\nabla u + \alpha u - \gamma) + qu = g - h^T \mu && \text{in } \partial\Omega \\
& u = r && \text{in } \partial\Omega
\end{aligned}
\qquad 3.1
$$

where

- Ω is the computational domain—the union of all domains
- δΩ is the domain boundary
- **n** is the outward unit normal vector on δΩ

The first equation in the list above is the PDE, which must be satisfied in Ω. The second and third equations are the boundary conditions, which must hold on δΩ. The second equation is a generalization of a *Neumann* boundary condition, whereas the third equation is a *Dirichlet* boundary condition. In finite element terminology, the boundary condition corresponding to a Neumann boundary condition is called a *natural boundary conditions*, because it does not occur explicitly in the weak form of the PDE problem.

In the PDE interfaces, the corresponding condition is called a *flux* or *source*, because it specifies the value of the numerical flux at the boundary. Dirichlet conditions are also known as *essential boundary conditions* in finite element theory, because they impose a restriction on the trial space which is not part of the main equation.

In the PDE interfaces, a distinction is made between Dirichlet boundary conditions and *constraints*. The former directly specify the value of the dependent variable at the boundary, while the latter force an arbitrary function of the dependent variables to equal zero on the boundary. This makes the constraint a more general feature.

Within COMSOL Multiphysics, the coefficients *c*, α, β, γ, *a*, and *h*, and the terms *f*, *g*, and *r* are specified. They can all be functions of the spatial coordinates.

- A PDE is *linear* when the coefficients depend only on the spatial coordinates (or are constants).
- A PDE is *nonlinear* if the coefficients depend on *u* or its derivatives (for example, the components of ∇u).
- All the coefficients in the above equation are scalars except α, β, and γ, which are vectors with *n* components. The coefficient *c* can alternatively be an *n*-by-*n* matrix to model anisotropic materials.

The e_a coefficient in Equation 3.1 is a scalar or a matrix for time-dependent systems called the *mass matrix* (or mass coefficient). The d_a coefficient represents a damping term (however, if $e_a = 0$, then *da* is often called the mass coefficient).

The interface identifier is a text string that can be used to reference the respective physics interface if appropriate. Such situations could occur when coupling this interface to another physics interface, or when trying to identify and use variables defined by this physics interface, which is used to reach the fields and variables in expressions, for example. It can be changed to any unique string in the *Identifier* field.

The default identifier (for the first interface in the model) is c (in domains), cb, ce, or cp (on boundaries, edges, and at points, respectively). The default setting is to include *All domains* in the model to define the PDE. To choose specific domains, select *Manual* from the *Selection* list. By default, the PDE interfaces are unitless, but you can define units for the dependent variable and the source term (that is, the overall left and right side of the equation).

The units for these quantities—in combination with the units for length and time— fully define the units for all other terms in the equations. To select the units you select the corresponding quantity from a list of physical quantities or enter the unit directly. Select the quantity that defines the unit for the dependent variable *u* from the *Dependent variable quantity* list.

The default is *Dimensionless [1].* Select *None* to enter a unit (for example, K, m/s, or mol/m^3) in the *Unit* field that appears. Select the quantity that defines the unit for the source term *f* (the unit for

the right— and left—side of the PDE) from the *Source term quantity* list. Select *None* (the default) to enter a unit (for example, W/m^3 or A/m^3) in the *Unit* field that appears. The default unit is m^-2, which is a consistent with a dimensionless dependent variable.

This is the default equation for a Coefficient Form PDE interface. Specify the coefficients for a coefficient form PDE (see Equation 3.1), with the following equation coefficients:

$$e_a \frac{\partial^2 u}{\partial t^2} + d_a \frac{\partial u}{\partial t} + \nabla \cdot (-c\nabla u - \alpha u + \gamma) + \beta \cdot \nabla u + au = f \qquad 3.2$$

- e_a is the *mass coefficient*.
- d_a is a *damping coefficient* or a *mass coefficient*.
- c is the *diffusion coefficient*.
- α is the *conservative flux convection coefficient*.
- β is the *convection coefficient*.
- a is the *absorption coefficient*.
- γ is the *conservative flux source* term.
- f is the *source term*.

4. MODELING LANDSLIDE AND TSUNAMI

In this chapter the event of 6th February 1783 in Scilla (Italy) will be modeled and simulated using the numerical model developed by Bellotti (2008) and based on the mild-slope equation to reproduce the propagation of small-amplitude transient waves.

The model make use of the Fourier Transform to convert the time-dependent hyperbolic equation into a set of elliptic equations in the frequency domain. It is described in Chapter 1.

The software used to perform this simulation is COMSOL Multiphysics and its features are described in Chapter 3.

In order to simulate the event, the preliminary step is the definition of the geographical domain based on topographic and bathymetric data by using QGIS software, wich was chosen because the data are available in ASCII file and must be georeferenced.

Once bathymetric data have been georeferenced, they are available in X, Y and Z coordinates, so the software package MATLAB was used in order to create a regular meshgrid that interpolate all the data.

The second step, once the domain has been reconstructed, is to model the landslide that caused the tsunami by using MATLAB.

The earthquake, witnessed and described by contemporary sources, triggered the landslide which detached from the front of Monte Pacì and settled in the sea.

It consisted, therefore, of an aerial and a submarine phase. In this study only the movement in its submarine phase is considered.

The third step is the definition of the computing domain. Firstly it was built on GIS through a shapefile; later it was imported into the software package COMSOL.

Working on this type of domain with QGIS is convenient because all the results obtained are already georeferenced and therefore no further steps are required in the output processing phase with MATLAB.

The simulation, as previously mentioned, is based on the numerical model of Bellotti (2008); the results are in the frequency domain and in the post-processing phase they are converted into the time domain to obtain the wave progressive propagation.

4.1 Methodology

In order to deal with the numerical modeling of the phenomenon, there were several preparatory steps for the simulation that can be summarized in 11 points:

1. Acquisition of geographic data from IGM (Military Geographic Institute);
2. Construction of the geographical domain by using QGIS;
3. Creation of a single file with all the georeferenced bathymetric data available and importation into MATLAB to be processed. A grid was created to interpolate the data, which were not structured, with $\Delta x = \Delta y = 10$ m, the interpolation concerned the three coordinates x, y and z;
4. Extrapolation of a subdomain, the one corresponding to the passage of the landslide, to evaluate its displacement over time. The domain concerned had dimensions of X=360 m axis parallel to the coast and Y=1400 m approximately orthogonal axis to the coast and reached a depth of -300 m in which the landslide was deposited in its final position;
5. Evaluation of the geometric shape of the landslide; the simulation of the landslide over time undertaken by Mazzanti and Bozzano (2011) was taken as a reference (see Fig. 2.11 on the Chapter 2);
6. The bathymetric subdomain extracted corresponding to the passage of the landslide is reworked in MATLAB in order to create an ellipsoidal grid;
7. Estimation of the simulation of the displacement of the landslide at different time points;
8. Identification of the geographic domain to be included in COMSOL, where the characteristics of the model were then assigned;
9. Creation in MATLAB of an array that represents the position of the landslide in the spatial dimensions x and y at various time points. The result was, therefore, a set of matrices that represent the spatial position and in the third dimension there was the spatial variation over time.
10. Insertion of boundary conditions and mesh COMSOL;
11. Wave propagation simulation in COMSOL software and extrapolation of the results.

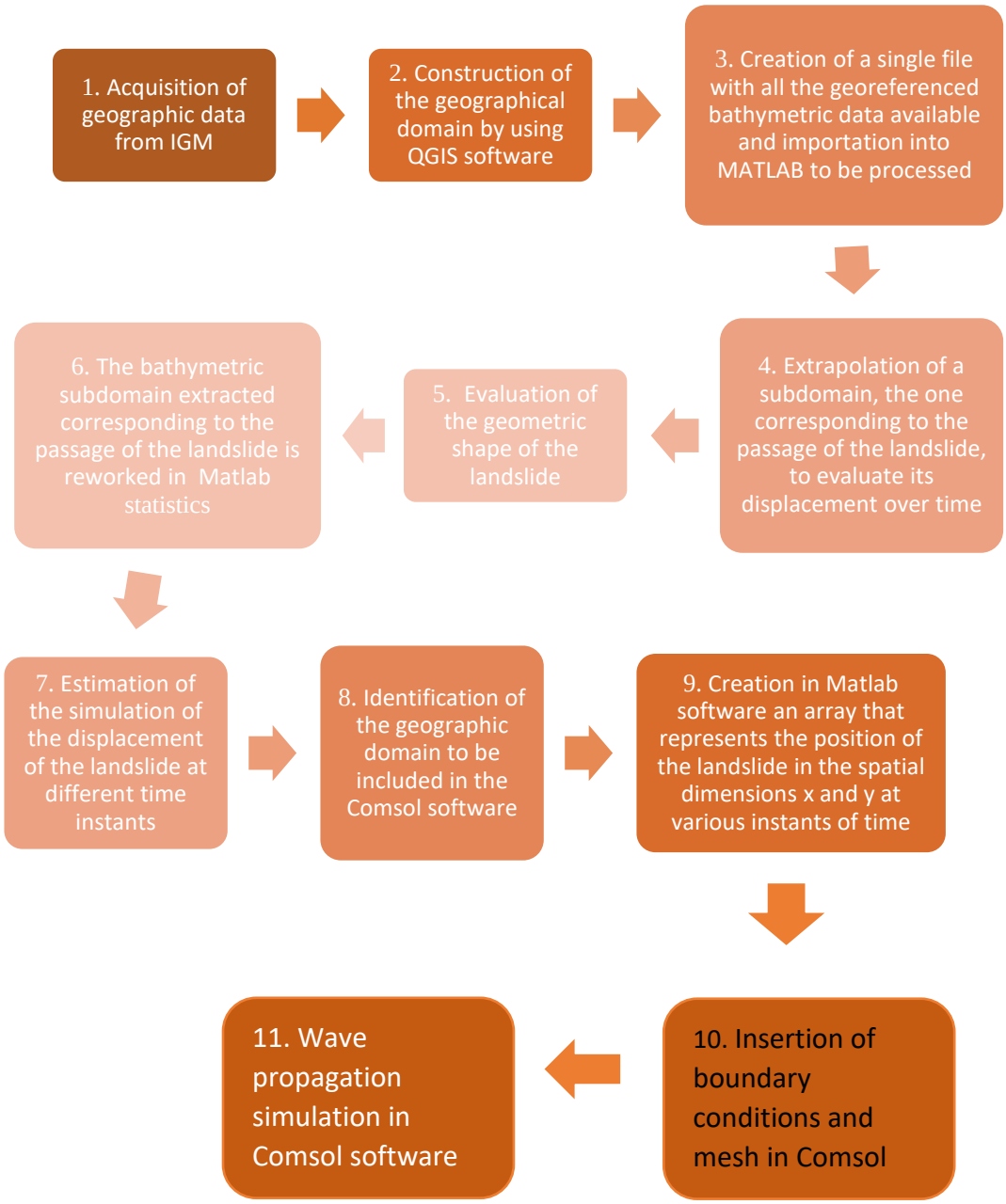

4.2 Geographic data and domain

The model grid requires a depth matrix that is developed by interpolating bathymetric and topographic data of the resolution that is commensurate with that of the grid.

Bathymetry and topography for the grid was interpolated for the most accurate sources available.

In Fig. 4.1 the domain for which bathymetric data are available is identified.

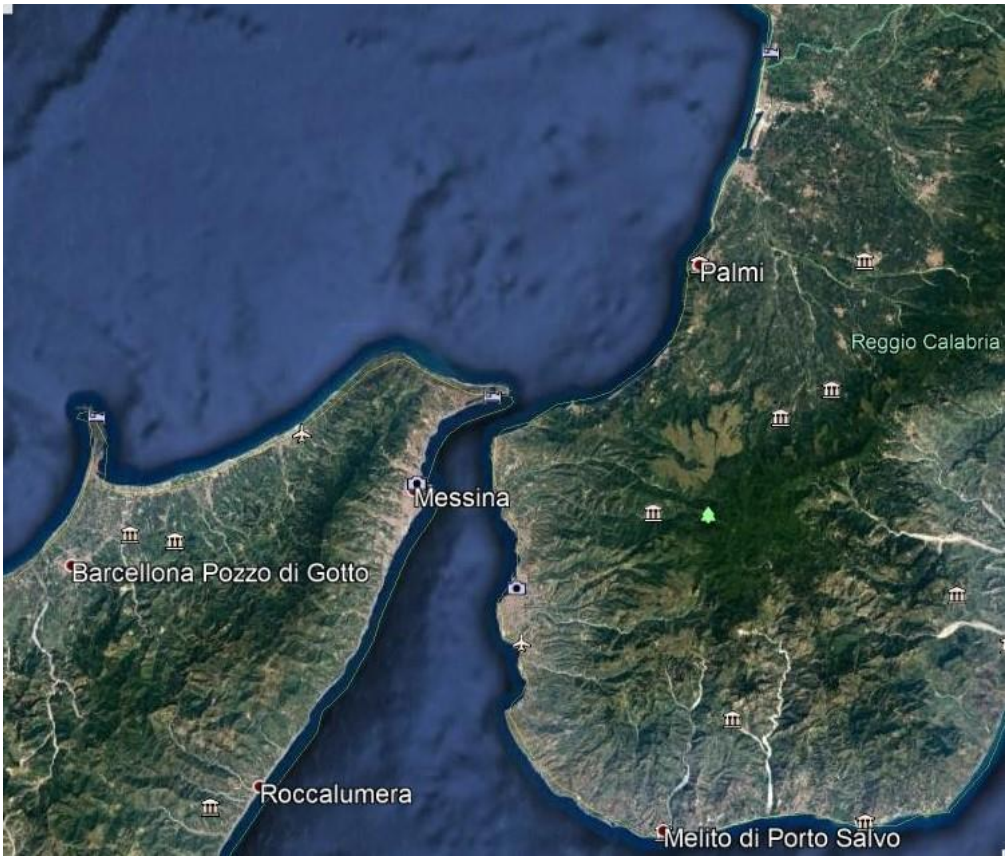

Fig. 4.1 Reference domain for the event of 1783 (source Google Earth).

The IGM (Military Geographic Institute) provided the bathymetry as 80 vector files with unstructured data. The original reference system was WGS 84/UTM zone 33N, so each file was first converted to a shapefile by using QGIS while maintaining the same georeferencing.

The following figures (Fig. 4.2 and Fig. 4.3) are extrapolated from the software and represent the shapefile created through the available points.

Fig. 4.2 QGIS shapefile that identifies bathymetric data (source QGIS).

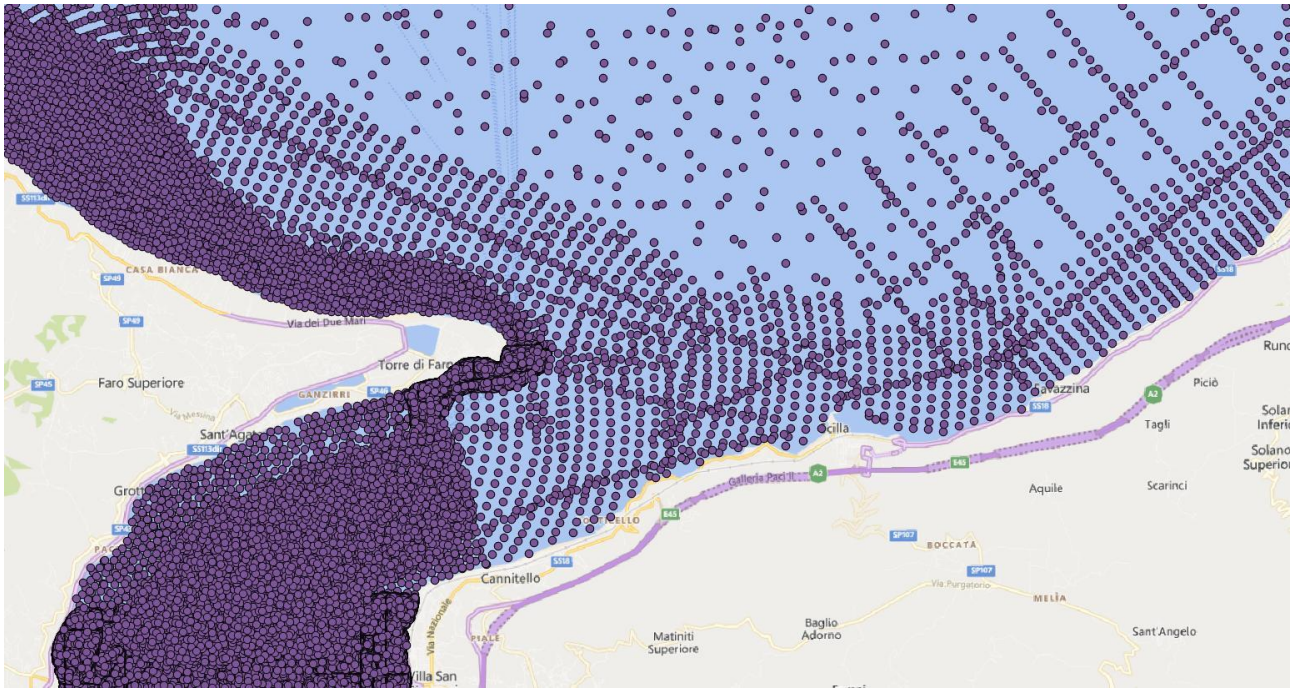

Fig. 4.3 QGIS shapefile that identifies a zoom of the area most affected by the tsunami (source QGIS).

Once a single file was created with all the georeferenced bathymetric data available, they were imported into MATLAB to be processed. A grid was created to interpolate the data, which are not structured, with $\Delta x = \Delta y = 10$ m, the interpolation concerned the three coordinates x, y and z.

The meshgrid features are summarized in the following table:

Δx (m)	Δy (m)	N_x	N_y	X_{min} (m)	X_{max} (m)	Y_{min} (m)	Y_{max} (m)
10	10	2500	2650	5.4730e+05	5.7247e+05	4.2229e+06	4.2494e+06

Table 8 *Meshgrid features interpolating bathymetric data.*

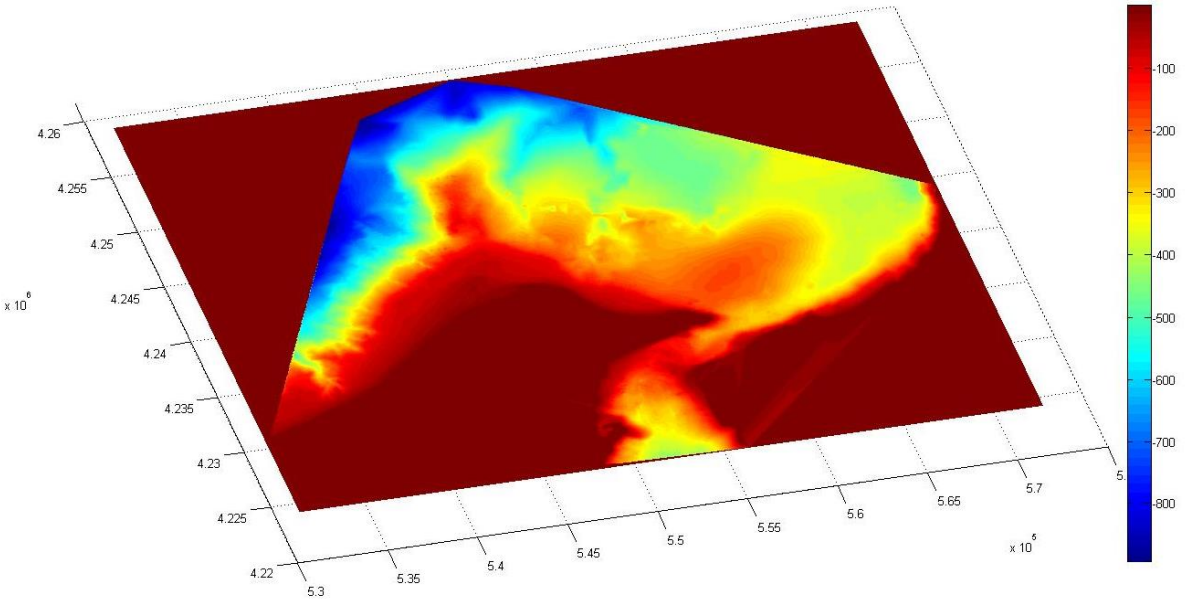

Fig. 4.4 2D plane view of meshgrid interpolating bathymetric data.

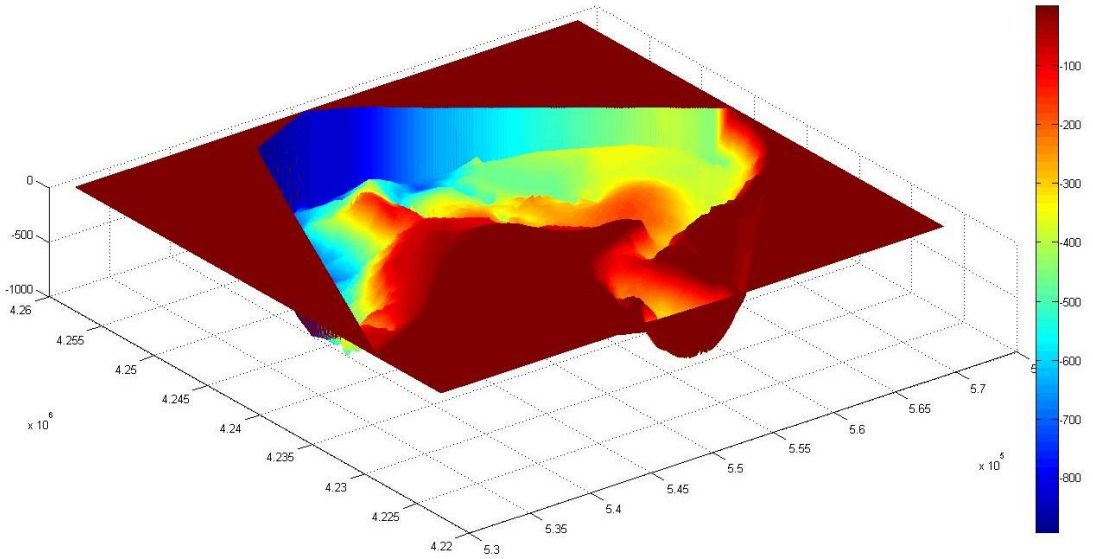

Fig. 4.5 3D plane view of meshgrid interpolating bathymetric data.

4.3 Landslide modeling

Once the domain was created, a subdomain was extrapolated, corresponding to the passage of the landslide, to evaluate its displacement over time. In Fig. 4.6 the position of the subdomain is shown.

Fig. 4.6 Identification of the subdomain affected by the landslide in QGIS.

The domain concerned had the dimensions X=360 m axis parallel to the coast and Y=1400 m approximately orthogonal axis to the coast and reaches a depth of -300 m in which the landslide was deposited in its final position.

The first step was the evaluation of the geometric shape of the landslide. The simulation of the landslide over time undertaken by Mazzanti and Bozzano (2011) was taken as a reference (see Fig. 2.11 in Chapter 2) .

Using that simulation as a starting point, the geometric quantities were taken for each simulated time point (length, width and height) and then an ellipsoidal profile was reconstructed on MATLAB given by the average value of these quantities. The landslide had a maximum height of 25 m, a length of 740 m and a width of 360 m.

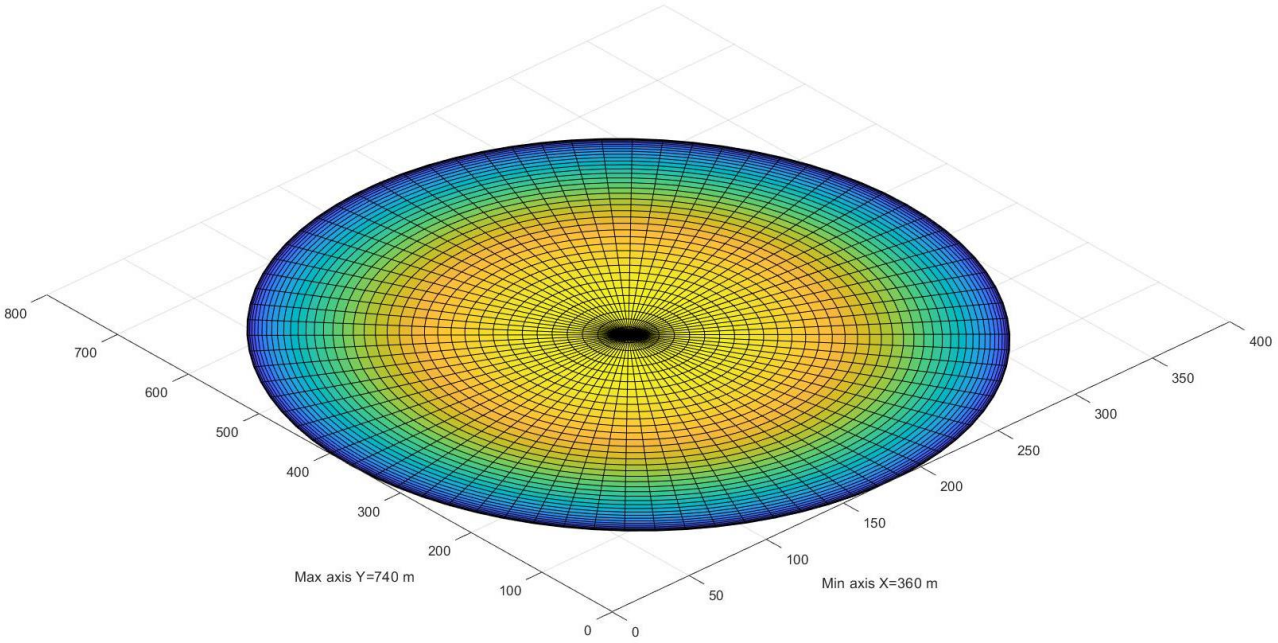

Fig. 4.7 2D plane view of the landslide geometric shape.

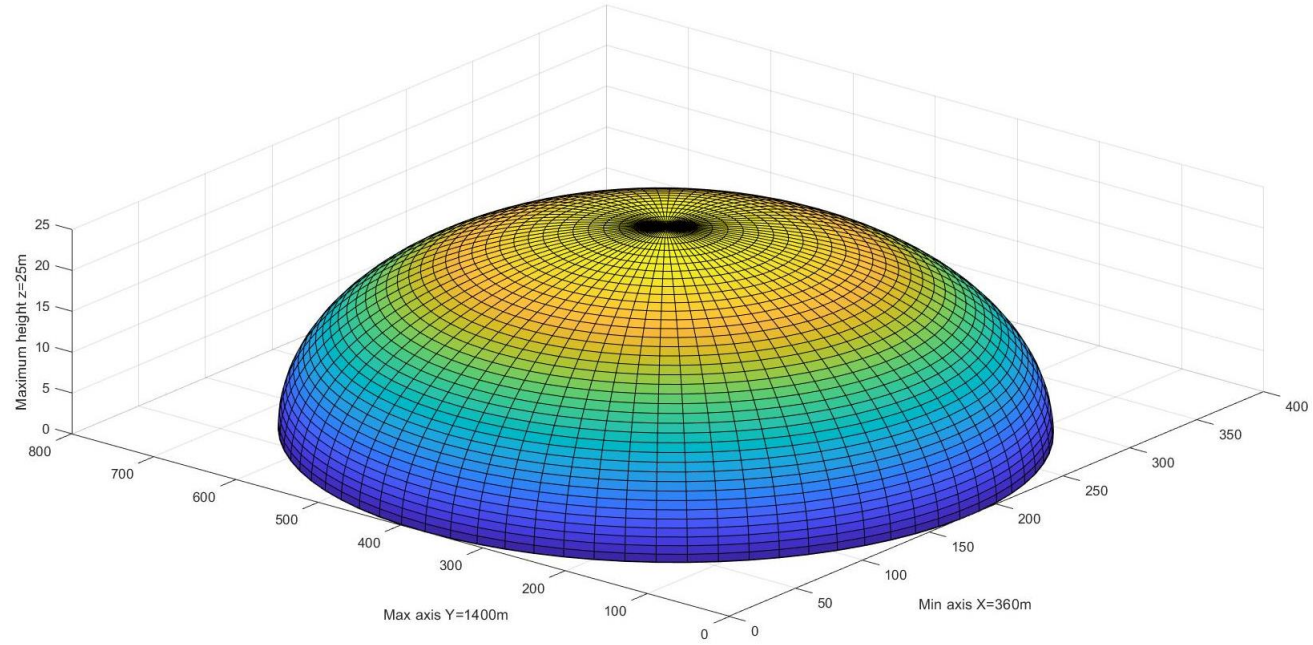

Fig. 4.8 3D plane view of the landslide geometric shape.

Since an ellipsoidal geometric shape of the landslide was hypothesized, the bathymetric subdomain extracted corresponding to the passage of the landslide was reworked in MATLAB in order to create an ellipsoidal grid.

This made it possible to obtain the correspondence between the points of the bathymetric grid and those of the landslide which is necessary for the subsequent calculation of the source term.

In order to work on the displacement, the domain on which the landslide moves was always modeled with $\Delta x = \Delta y = 10m$.

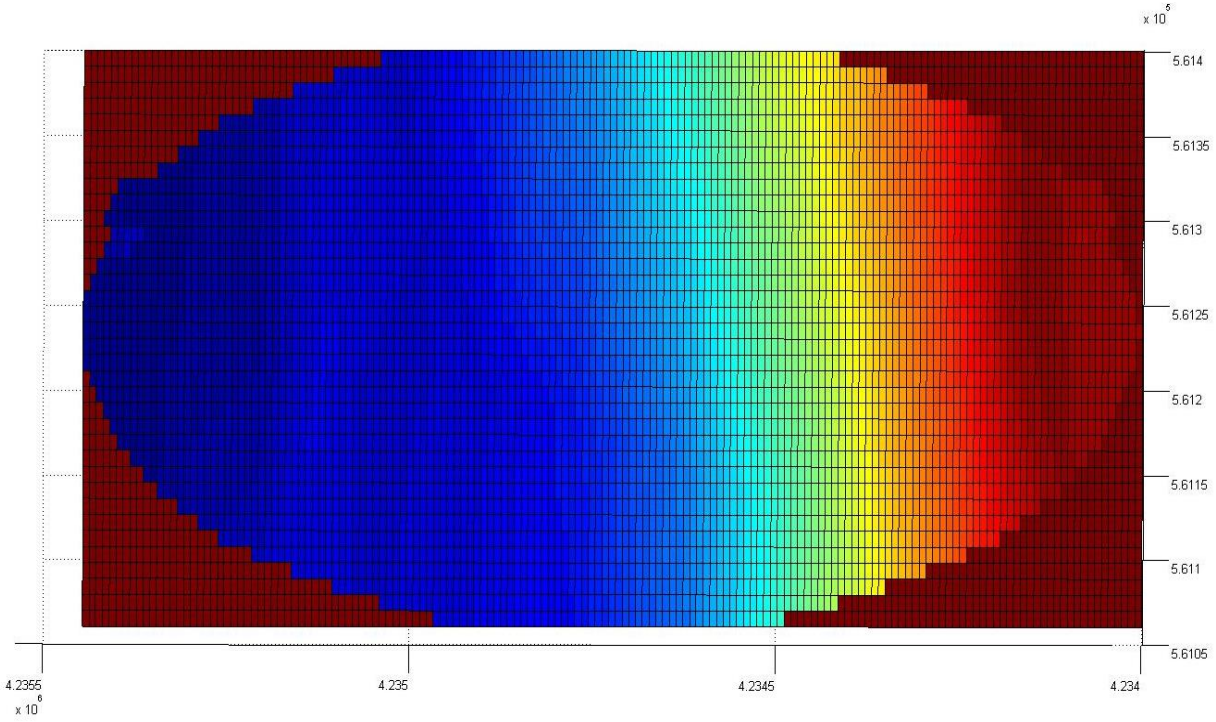

Fig. 4.9: 2D plane view of the ellipsoidal bathymeric subdomain.

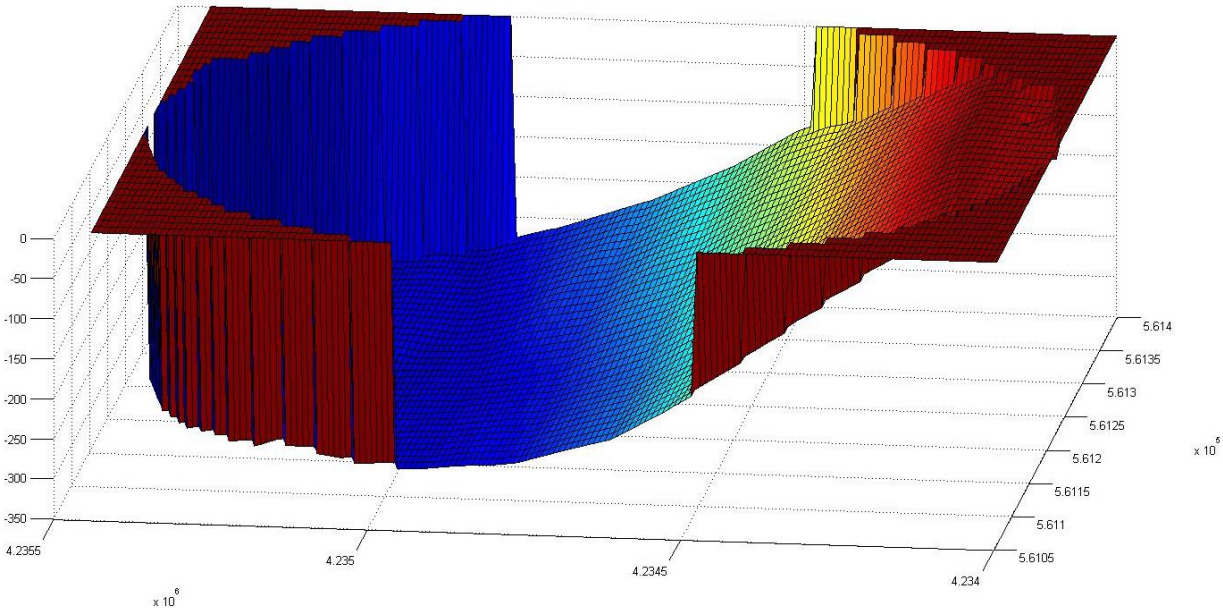

Fig. 4.10: 3D plane view of the ellipsoidal bathymeric subdomain.

The following table summarizes the geometric features of the bathymetric subdomain:

Δx (m)	Δy (m)	N_x	N_y	X_{min} (m)	X_{max} (m)	Y_{min} (m)	Y_{max} (m)
10	10	37	158	5.6105e+05	5.6150e+05	4.2340e+06	4.2356e+06

Table 9 *Meshgrid features of the bathymetric subdomain.*

Once the domain had been created, the time and velocity of movement of the landslide were evaluated; to do this, reference was always made to the article by Mazzanti and Bozzano, (see Fig. 2.11 and Fig. 2.12 on Chapter 2).

It starts with the simulation after 10 s, which is the instant in time when the landslide arrives in the sea and it begins to feel the effect of it. After about 30 s it is completely immerged, and after 40 s it settles in its final position; in the remaining time (80-120 sec) there is only an expansion of the material that constitutes it.

The following table summarizes the time features of the landslide displacement in its subaerial phase and in its submerged phase:

Total time of displacement (s)	ΔT (s)	N_t
30	0.5	79

Table 10 *Time features of the landslide displacement in its subaerial phase.*

Total time of displacement (s)	ΔT (s)	N_t
40	0.4	79

Table 11 *Time features of the landslide displacement in its submerged phase.*

The simulation of the displacement of the landslide at different time points takes place, therefore, by calculating the following quantity for each spatial point and at each time point:

$h(x,y,t)=h_f(x,y)-h_l(x,y,t)$;

the water depth function defined as the fixed sea floor depth (h_f) minus the thickness of the moving landslide (h_l).

The displacement at various time points is shown in the following figures, which represent the photographs of the movement of the landslide every 5 sec:

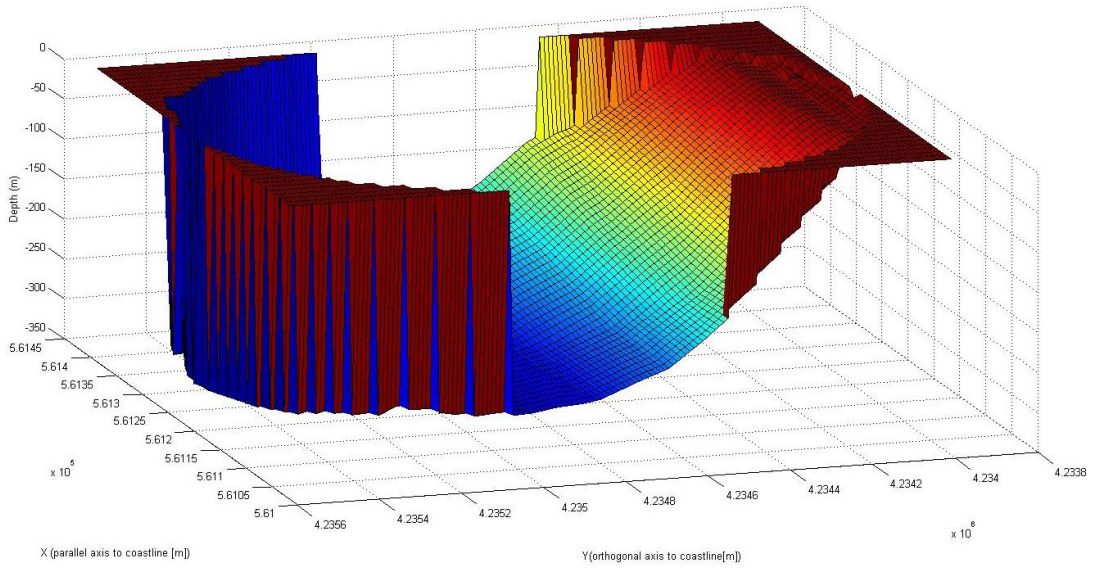

Fig 4.11 Landslide modeling at time T= 5 sec.

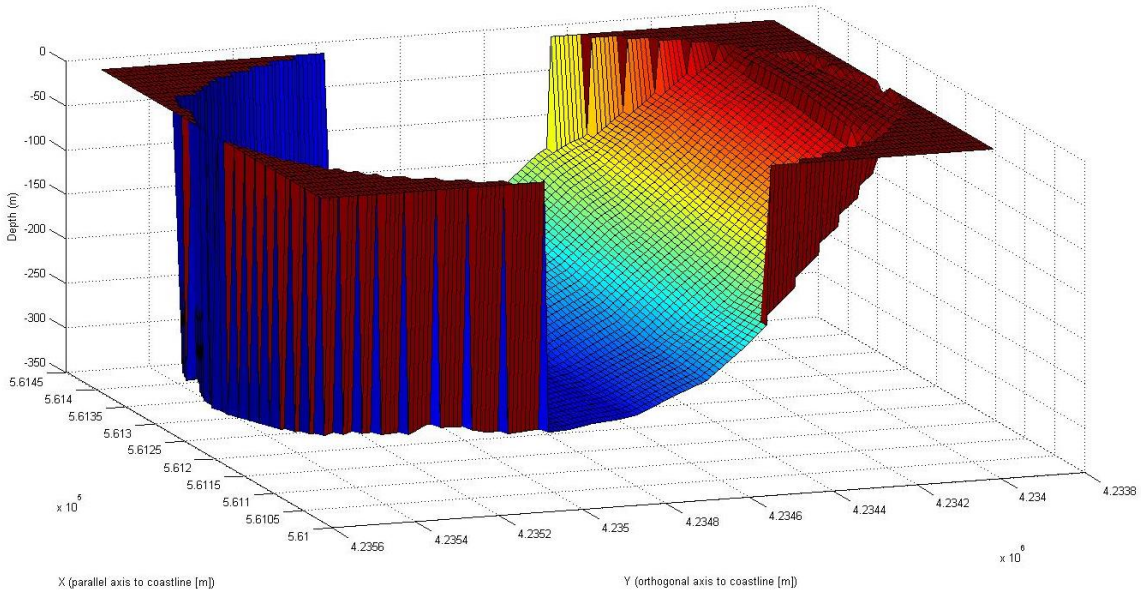

Fig 4.12 Landslide modeling at time T= 10 sec.

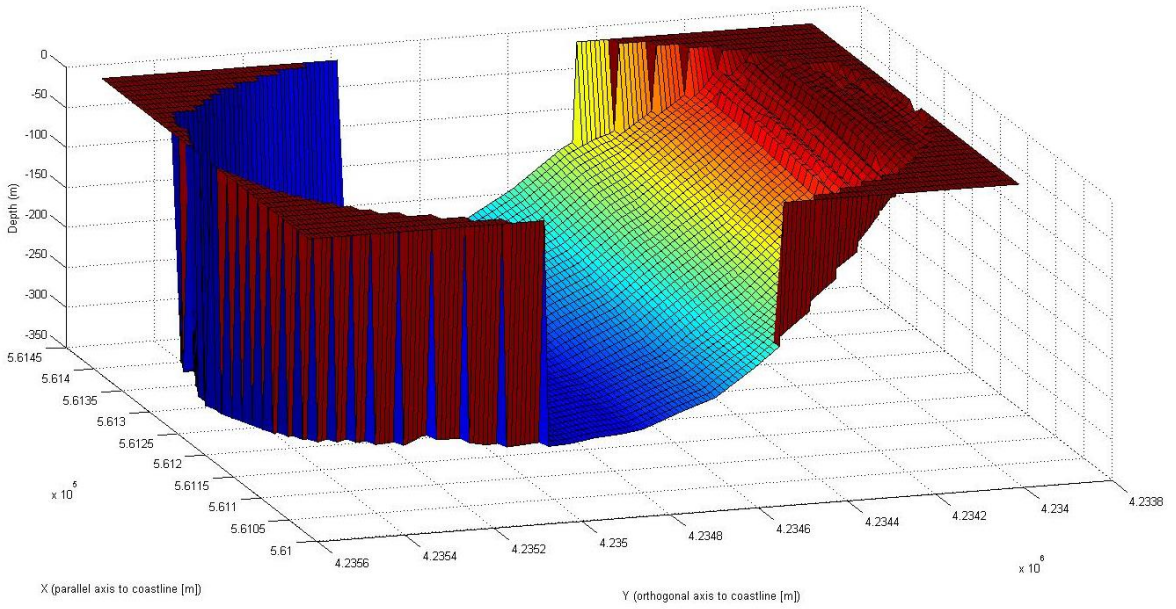

Fig 4.13 Landslide modeling at time T= 15 sec.

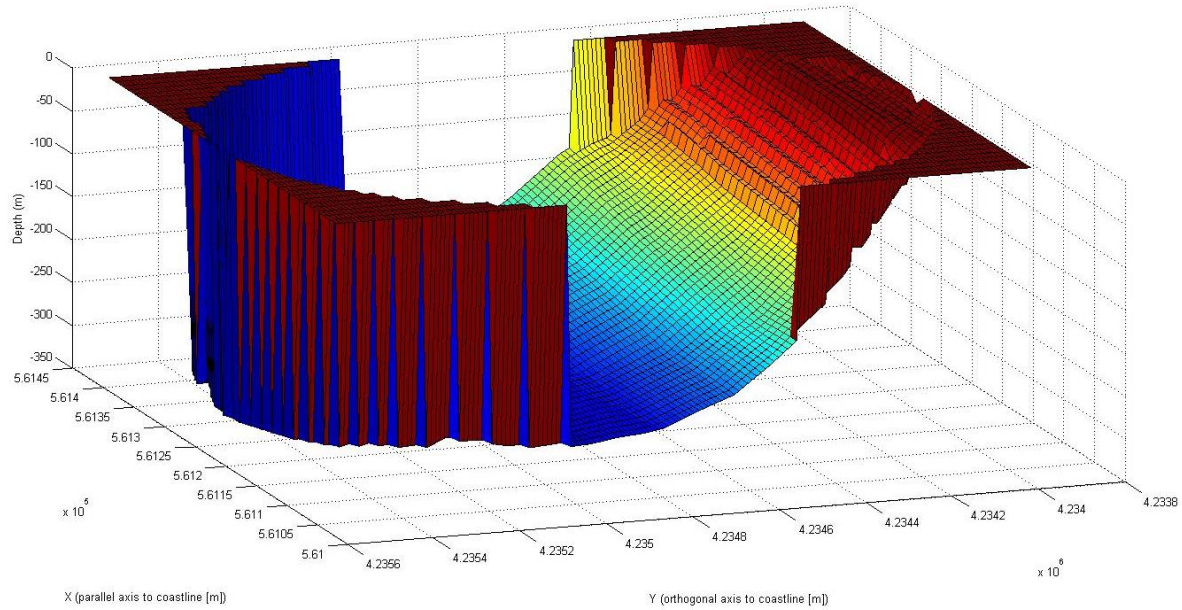

Fig 4.14 Landslide modeling at time T= 20 sec.

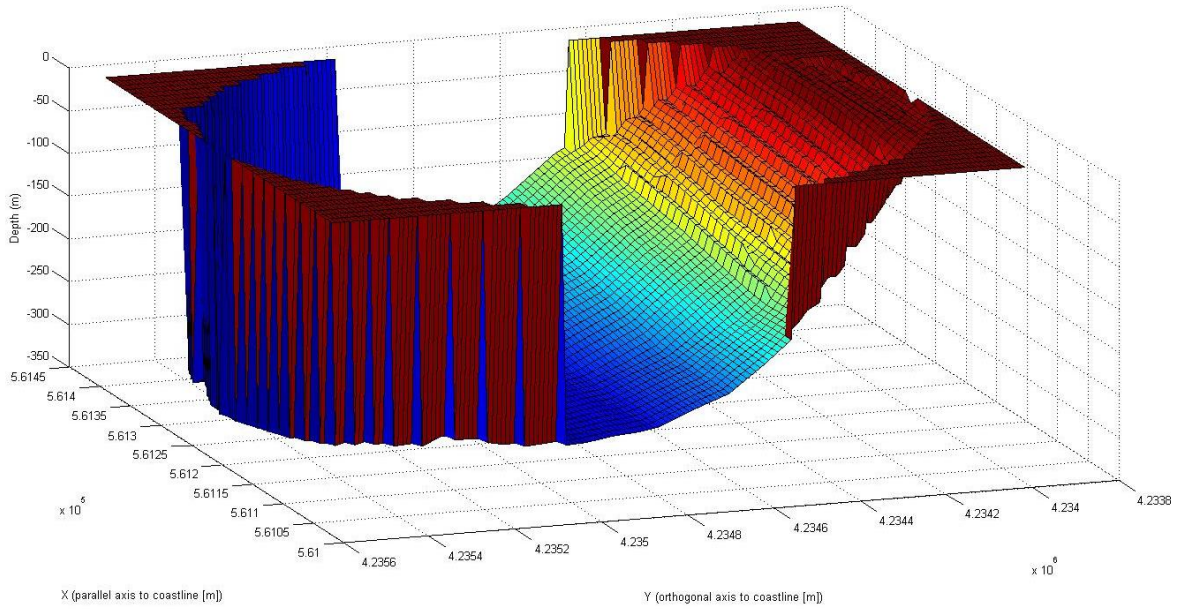

Fig 4.15 Landslide modeling at time T= 25 sec.

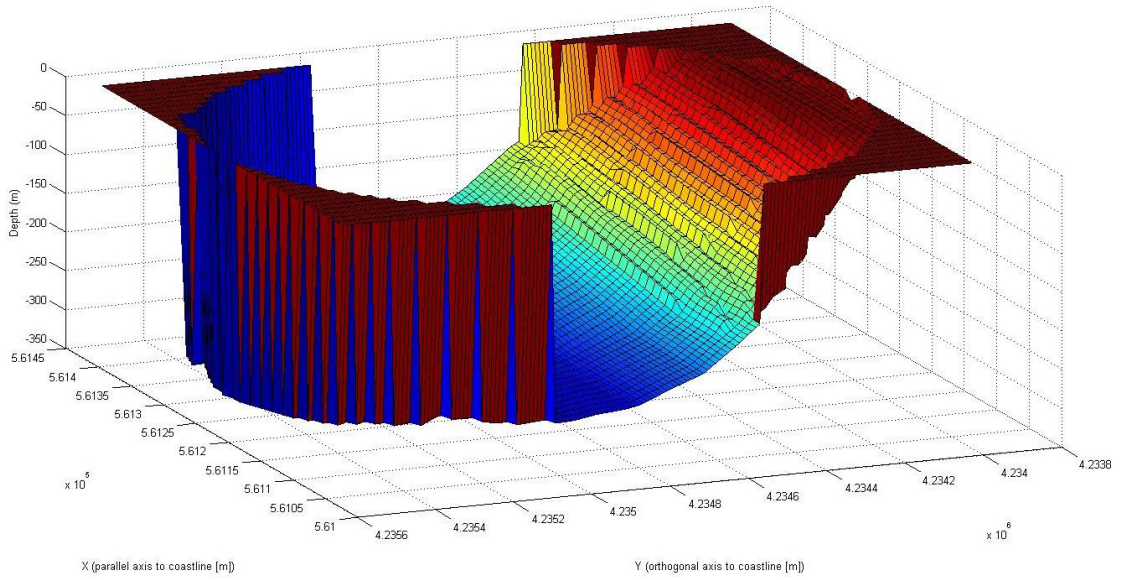

Fig 4.16 Landslide modeling at time T= 30 sec.

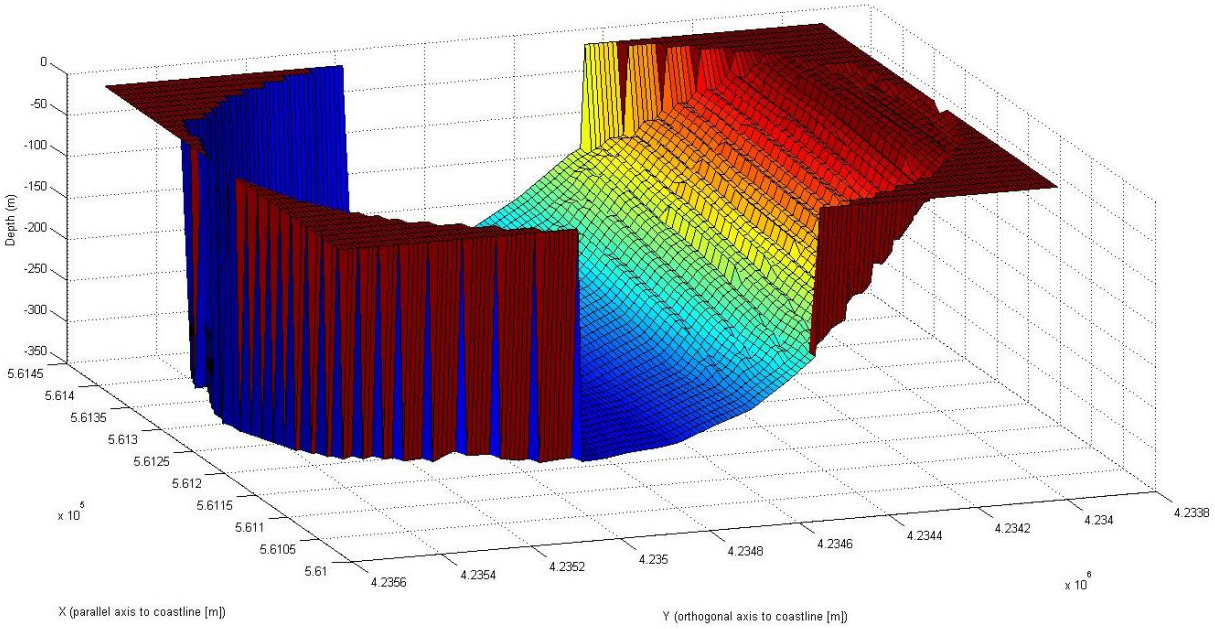

Fig 4.17 Landslide modeling at time T= 35 sec.

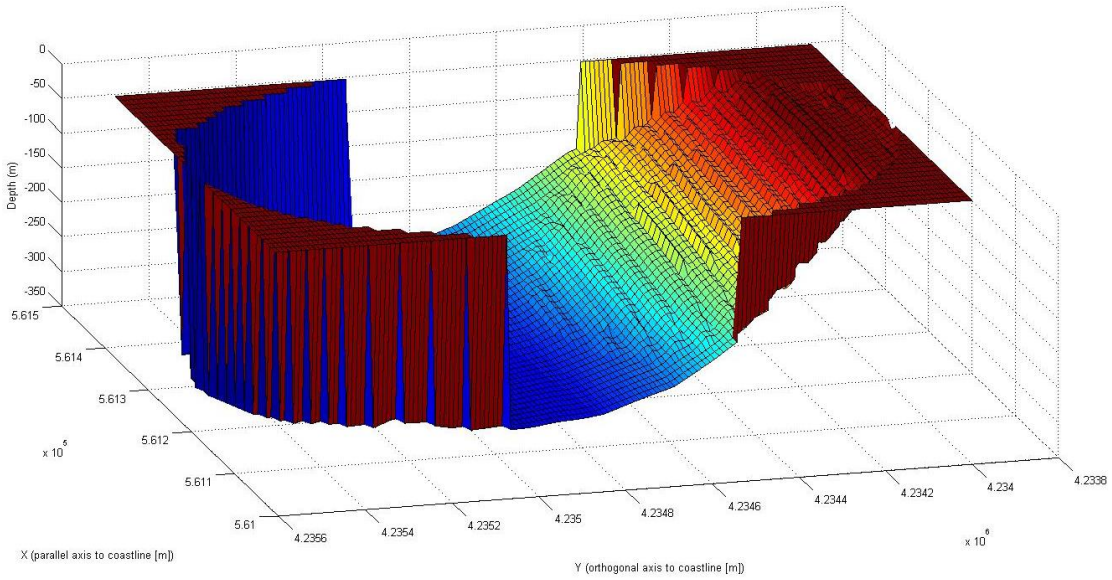

Fig 4.18 Landslide modeling at time T= 40 sec.

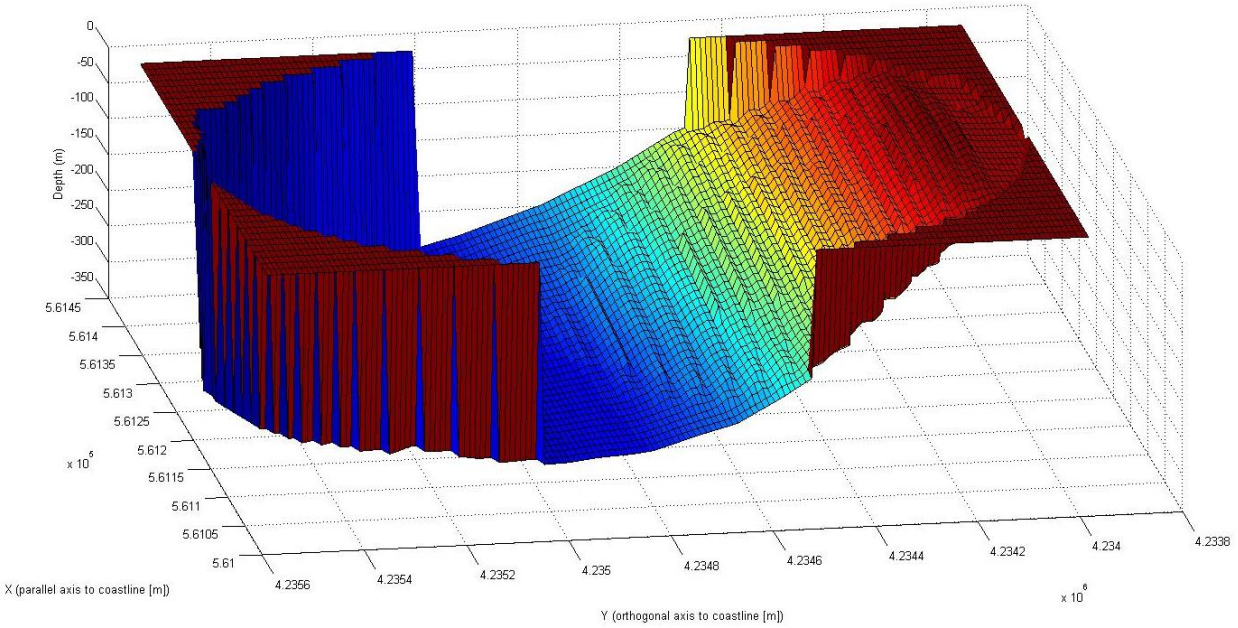

Fig 4.19 Landslide modeling at time T= 45 sec.

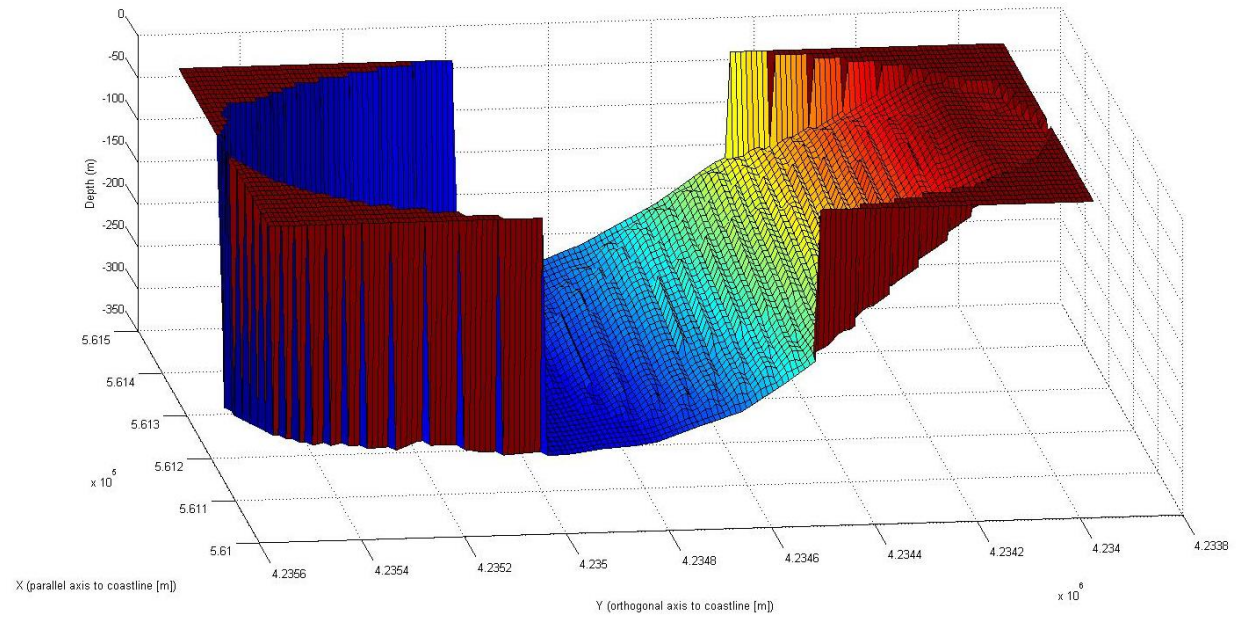

Fig 4.20 Landslide modeling at time T= 50 sec.

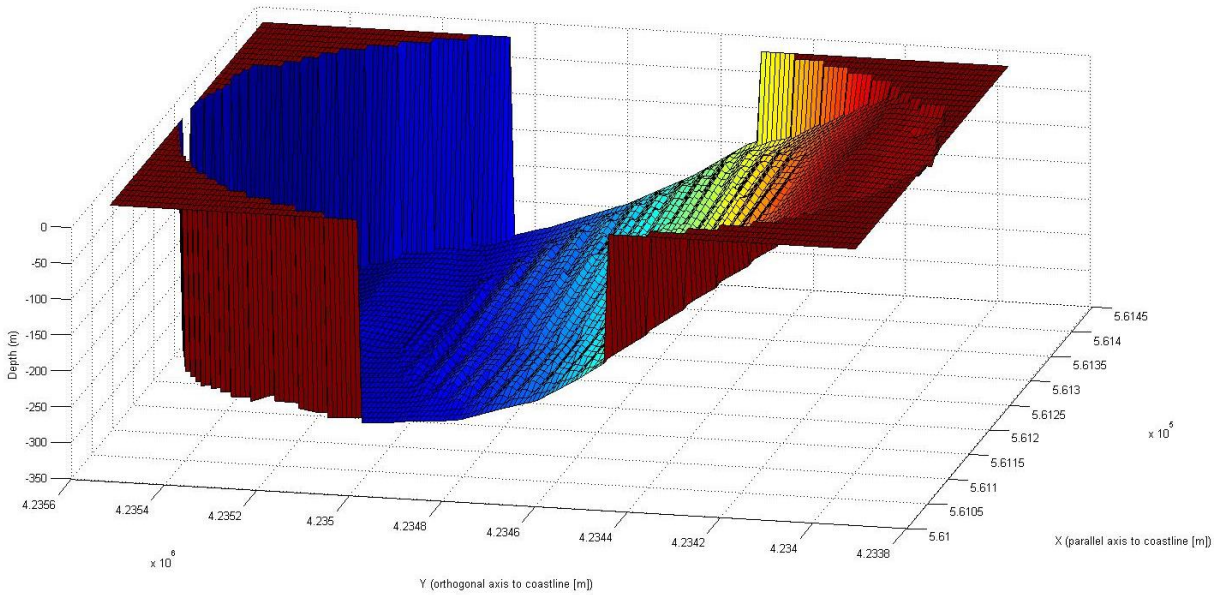

Fig 4.21 Landslide modeling at time T= 55 sec.

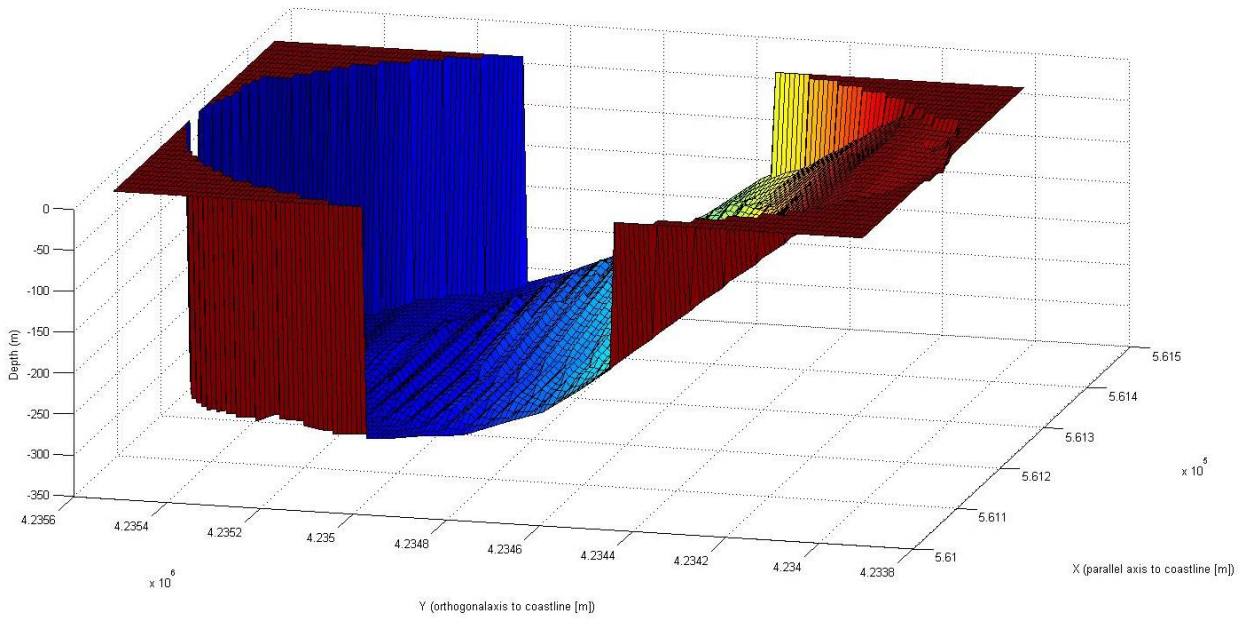

Fig 4.22 Landslide modeling at time T= 60 sec.

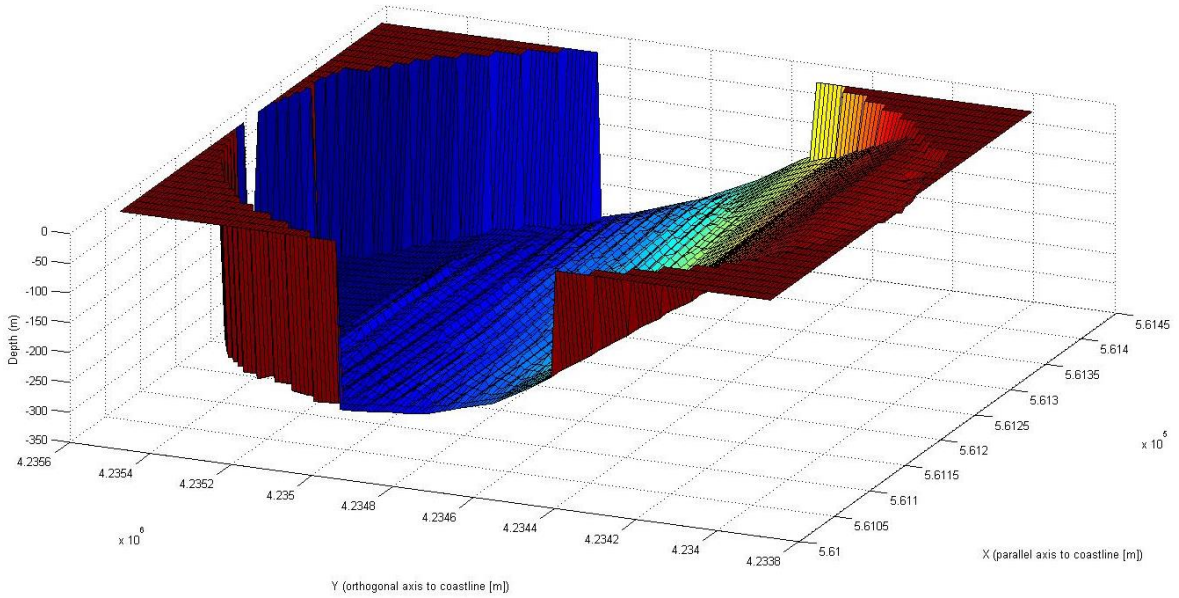

Fig 4.23 Landslide modeling at time T= 65 sec.

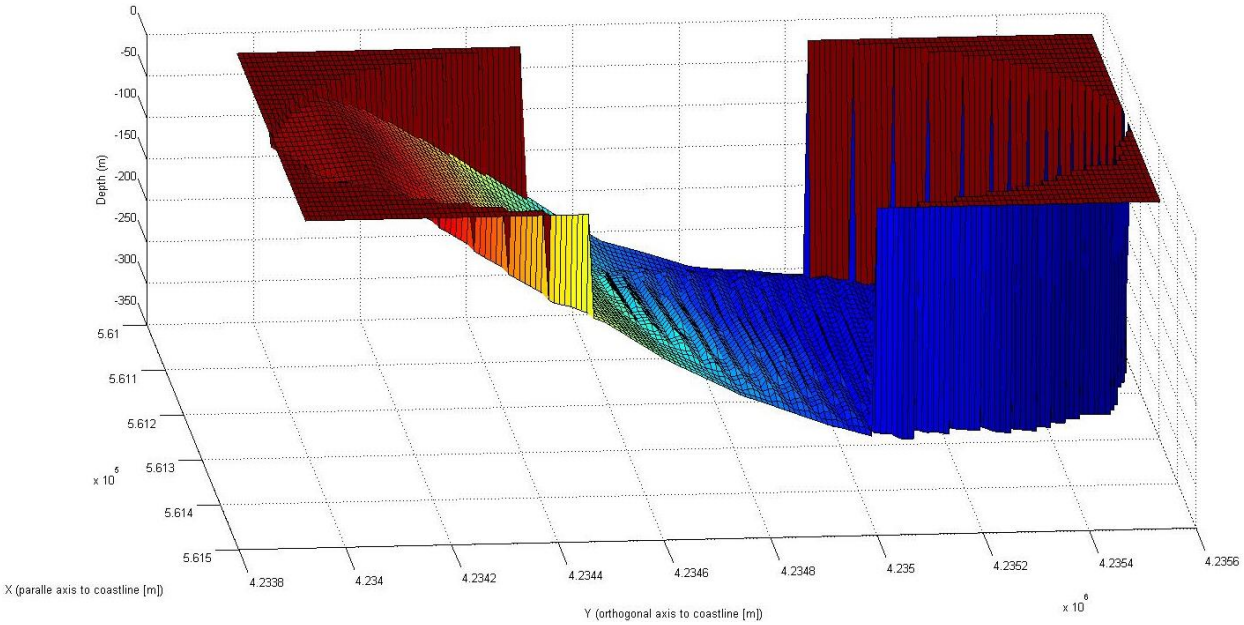

Fig 4.24 Landslide modeling at time T= 70 sec.

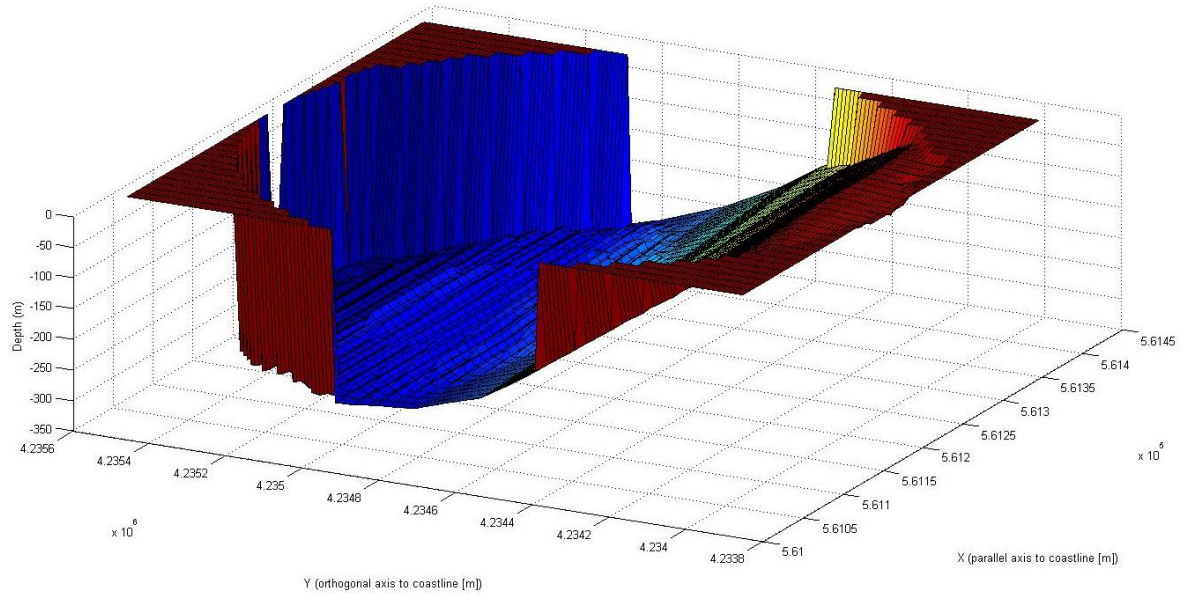

Fig 4.25 Landslide modeling at time T= 75 sec.

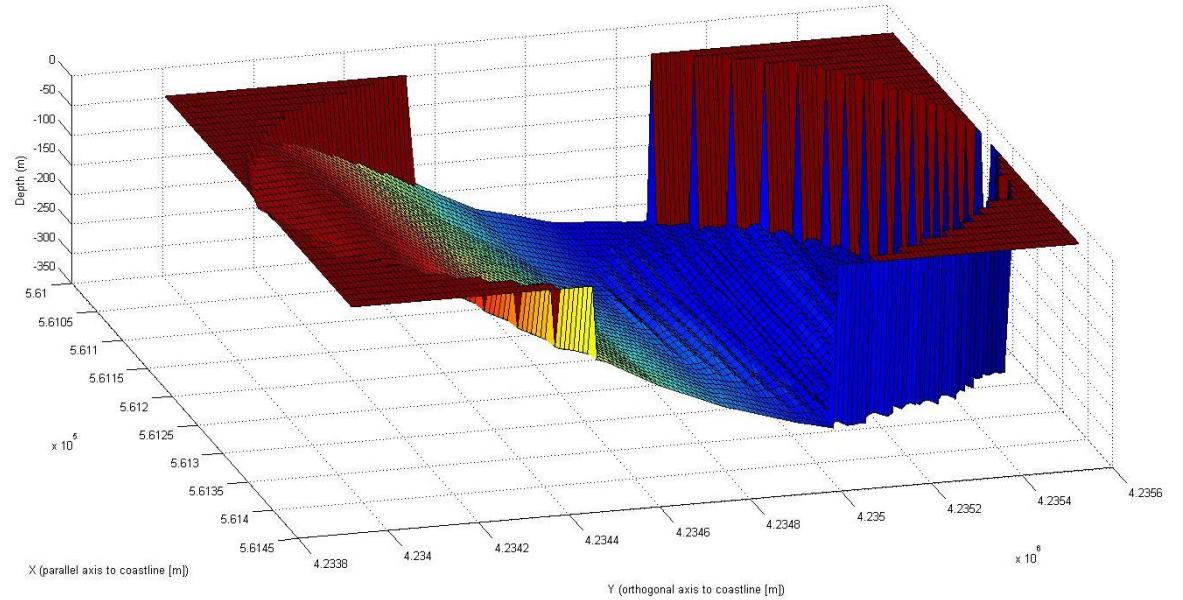

Fig 4.26 Landslide modeling at time T= 80 sec.

4.4 Wave propagation modeling

4.4.1 Geographic domain

The first step to implement the model is to identify the geographic domain to be included in COMSOL, where the characteristics of the model are then assigned. For this purpose, QGIS was used which made it possible to create, through shapefiles, the domain containing both the coastline and the circular contour that in tourn encloses the affected area and the bathymetric data available. The reference system is WGS 84/UTM zone 33N. Using QGIS is useful because once the domain is exported in COMSOL, every point is georeferenced according to that reference system.

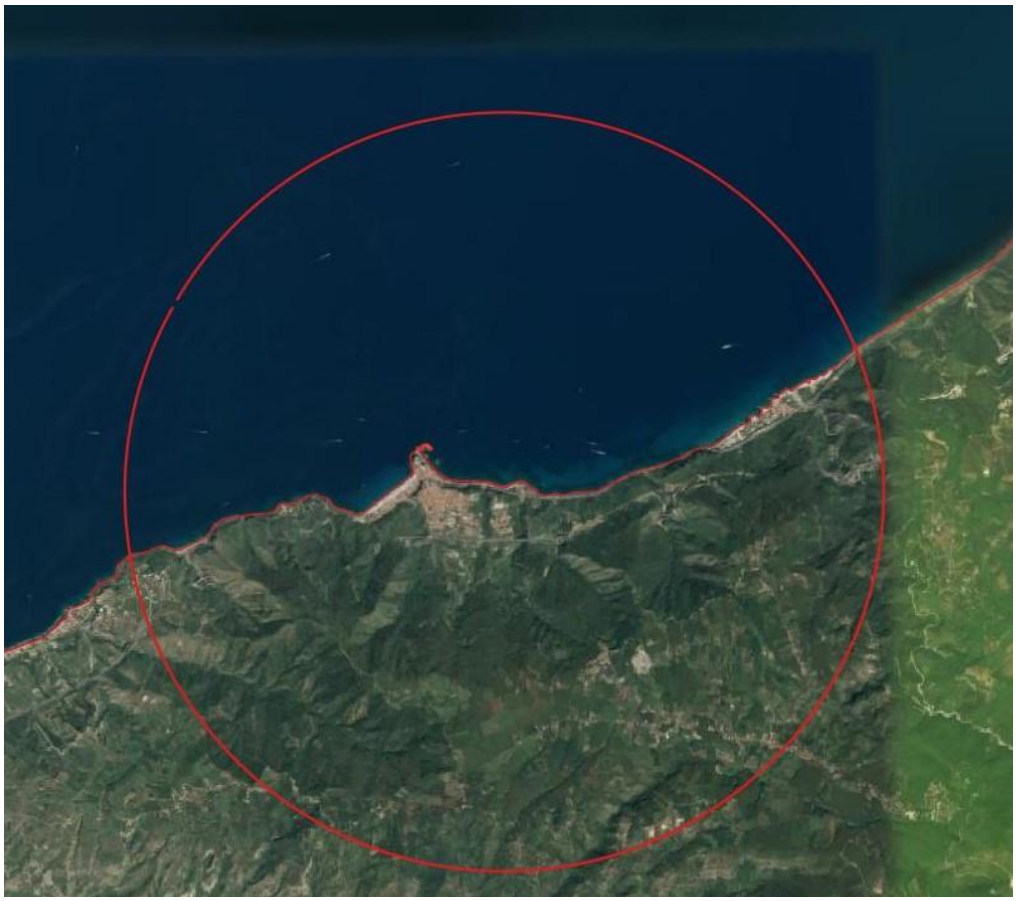

Fig 4.27 QGIS shapefile representing domain boundaries.

Once the shapefile is created, it is imported in AUTOCAD software as DXF file, in order to eliminate the part of the land domain that is not affected by the simulation.

The domain thus composed is therefore purified from the part of land not affected by the simulation and georeferenced; it can then be imported into COMSOL for modeling.

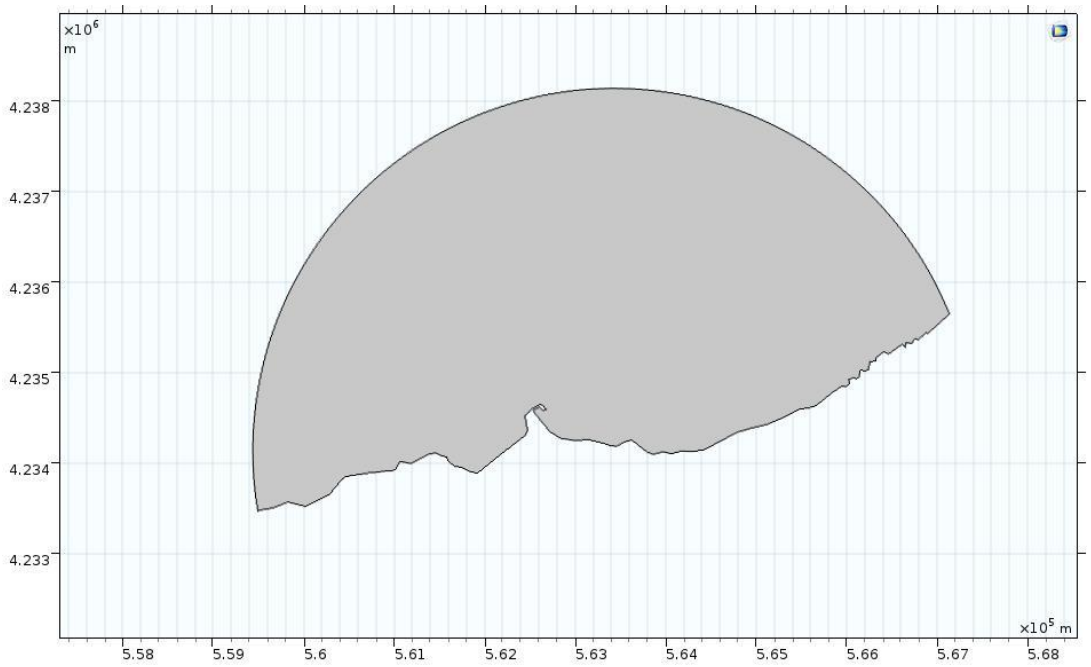

Fig 4.28 Scilla computational domain purified from the part of land (source COMSOL).

4.4.2 Geographic data

The second step is preparing the bathymetric data necessary to be included in the simulation. For this purpose, a subdomain was extrapolated from the meshgrid constructed from the data provided by the IGM (Figures 4.4 and 4.5).

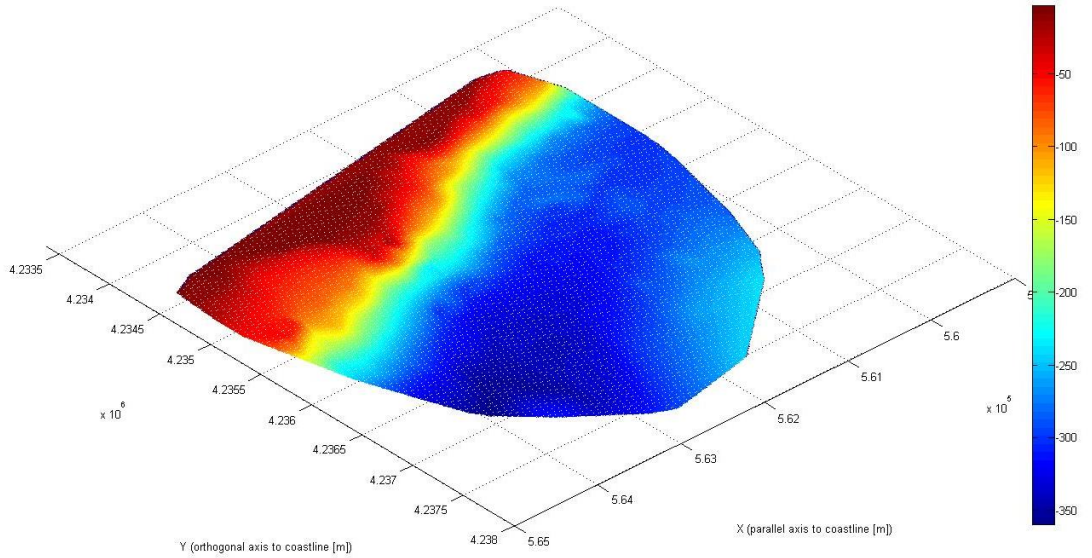

Fig. 4.29 2D plane view of meshgrid interpolating bathymetric data of Scilla.

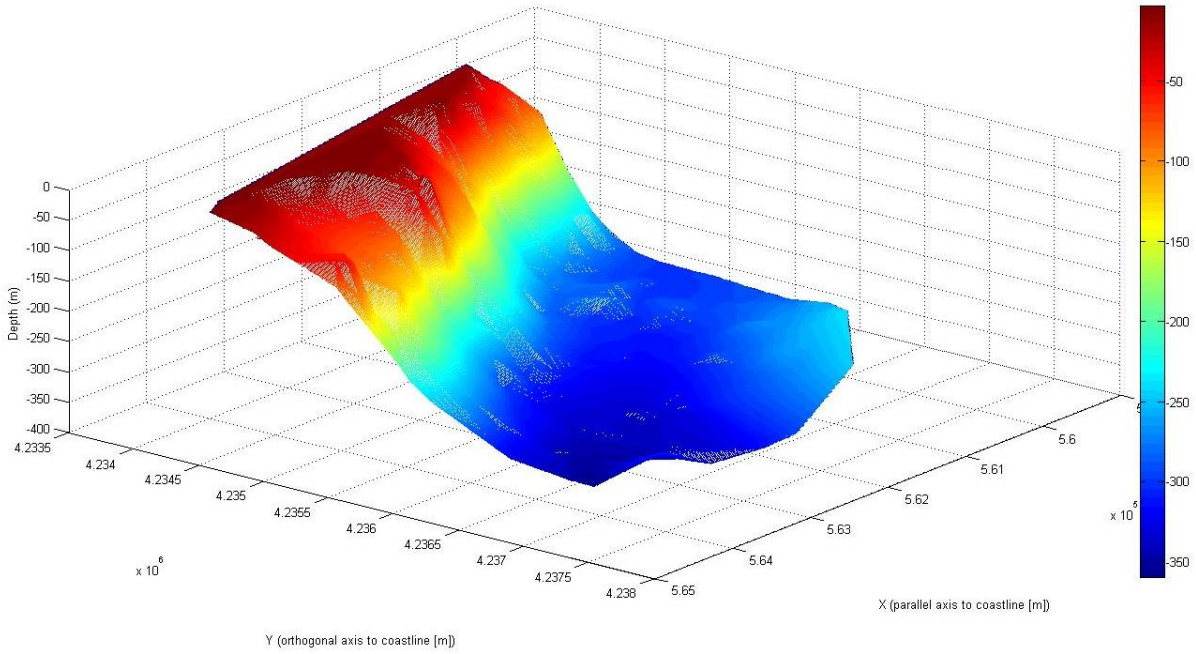

Fig. 4.30 3D plane view of meshgrid interpolating bathymetric data of Scilla.

4.4.3 Source term

The reference equation for applying the method is Eq. 1.36 referred below:

$$\eta_{tt} + gG\eta - \nabla \cdot (gF\nabla\eta) = -h_{tt}$$

This equation is usually referred to as the 'time-dependent mild slope equation' and allows the simulation in the time-domain of the wave propagation. F and G (eq. 1.40 and 1.41) were calculated by assuming a dominant frequency of the wave spectrum, but the validity of the resulting equation would only be for narrow-frequency spectra seas.

By employing the spectral approach proposed by Bellotti et al., the model can on the contrary cover a broad-spectrum wave field, typical of tsunamis, since for each wave frequency a dedicated elliptical equation is solved.

Eq. 1.36, once the Fourier transform is applied, becomes a frequency-dependent equation (Eq. 1.42):

$$\nabla\cdot(cc_g\nabla N)+\omega^2\frac{c_g}{c}N = -\omega^2 H$$

Where N(x,y,ω) and H(x,y,ω) are the Fourier Transform of η(x,y,t) and h_{tt}(x,y,t) respectively, and h_{tt} is the second derivative of the water depth function $h(x,y,t)=h_f(x,y)-h_l(x,y,t)$ defined as the fixed sea floor depth (h_f) minus the thickness of the moving landslide (h_l). k_s is the landslide length parameter, equal to $2\pi/L_s$, where L_s is the landslide length.

Regarding the source term, an array was created in MATLAB that represents the position of the landslide in the spatial dimensions x and y at various time points. The result is, therefore, a set of matrices that represent the spatial position and in the third dimension there is the spatial variation over time.

The resulting movement is represented by the figures from 4.11 to 4.26 and it is the value h(x,y,t). Subsequently the second derivative of h(x,y,t) was calculated and then the Fourier Transform of h_{tt}(,x,y,t) along the third dimension.

4.4.4 Boundary conditions

Boundary conditions used in this work are the fully reflective conditions at coastlines and a radiation condition boundary condition along the semi-circular domain, the use of which is detailed below. The full-reflection boundary conditions can be expressed by assuming that the fluid velocity in the direction orthogonal to the boundary is zero.

$N_n=0$

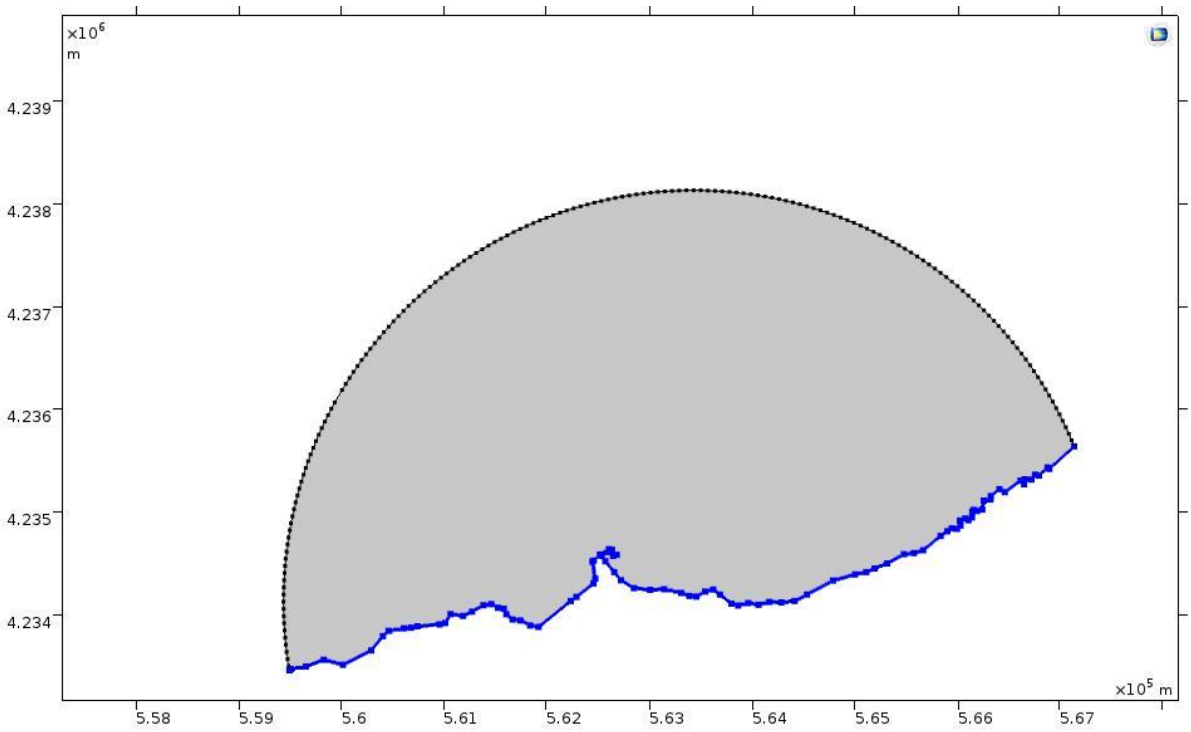

Fig. 4.31 Scilla coastline interested by full-reflection boundary condition (source COMSOL).

The radiation boundary condition can be obtained by using a mathematical formulation that allows the waves that propagate toward the open boundaries to freely exit the computational domain. This condition can be easily formulated for progressive outgoing waves (Sommerfeld, 1964; VanDongeren and Svendsen, 1997) (Eq. 1.44):

$$\eta_t + \frac{c}{\cos(\vartheta_n)}\eta_n = 0$$

The Fourier Transform of Eq. (1.44) provides the radiation condition in the frequency domain (see Beltrami et al., 2001; Steward and Panchang, 2000):

$$N_n + ikcos(\vartheta_n)N = 0$$

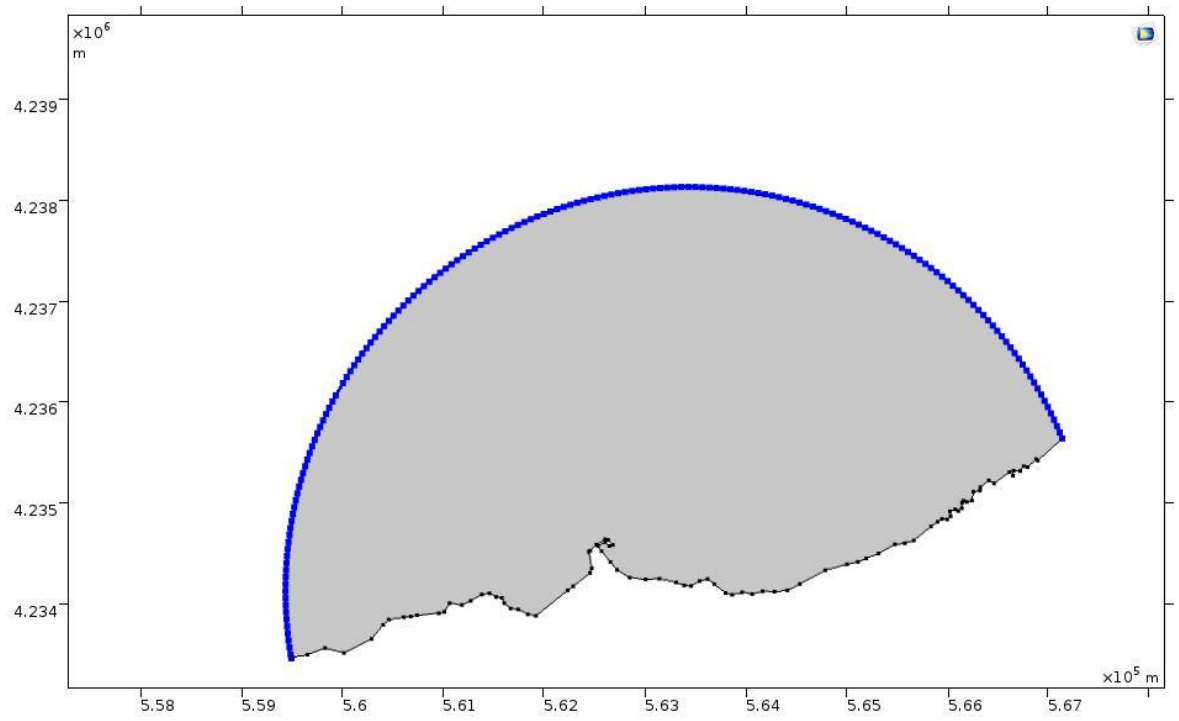

Fig. 4.32 Scilla coastline interested by radiation boundary condition (source COMSOL).

4.4.5 Meshing computational domain

The mesh used for the numerical modeling was chosen after a convergence analysis undertaken to find a balance between computational burdens and detail of the result. The numerical simulation should take into account a distance between the nodes of L/10, where L is the wave length that corresponds to the higher frequency in that range of frequencies at which the energy content is significantly greater than zero and that consequently are worth to be reproduced for the simulation. This is to ensure the minimum of 10 points for wave length.

The numerical simulation, carried out with a finite element method, uses triangular linear elements with a maximum size of 25 m and has a total number of DOF of 216,260.

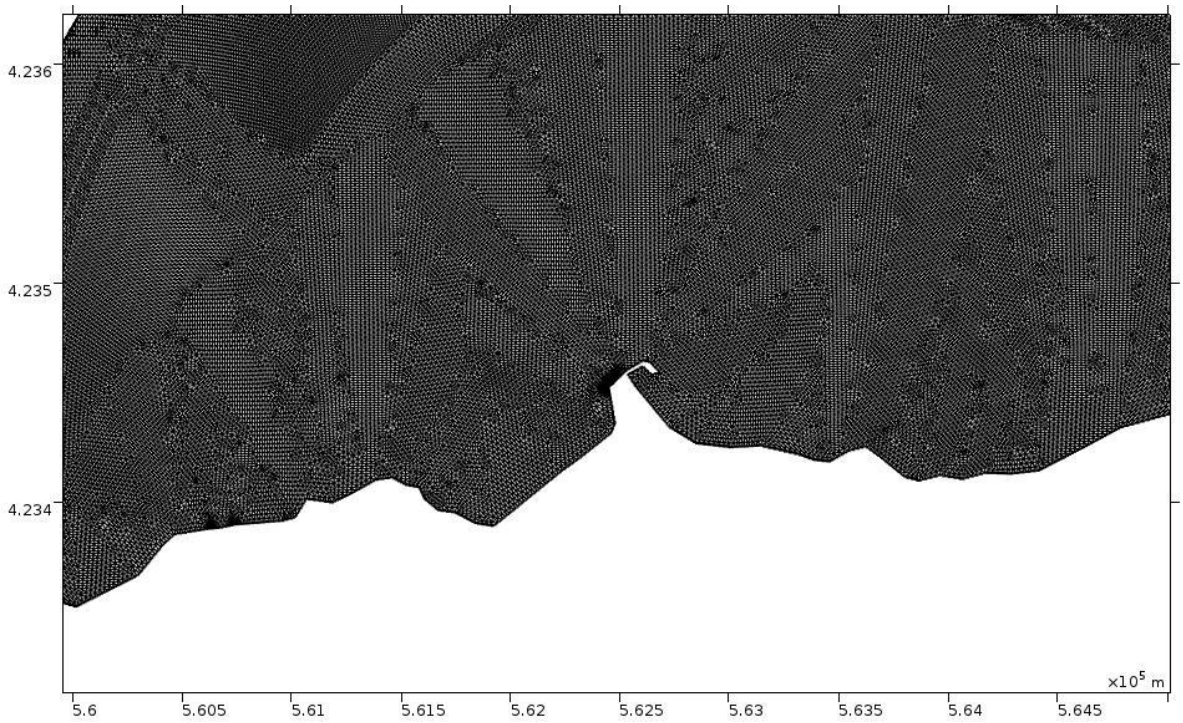

Fig. 4.33 Zoom of the elements of the mesh for the area of Scilla (source COMSOL).

4.4.6 Numerical simulation

The simulation was carried out taking Δt = 2 sec as the reference interval, in such a way as to have a maximum of 4000 units in time, considering a total simulation length of 8000 sec (approximately 133 minutes).

To these values, therefore, there correspond as many omega values between $7.85*10^{-4}$ rad/s < ω < 3.14 rad/s and frequency values in Hz between $1.25*10^{-4}$ Hz < f < 0.5 Hz.

Once the simulation was carried out, points were then taken which corresponded to the intensity of the waves generated by the tsunami in the Scilla area, as documented from historical sources.

In the following figure you can see the points where the wave elevation has been extrapolated and Table 11 shows the coordinates of those points :

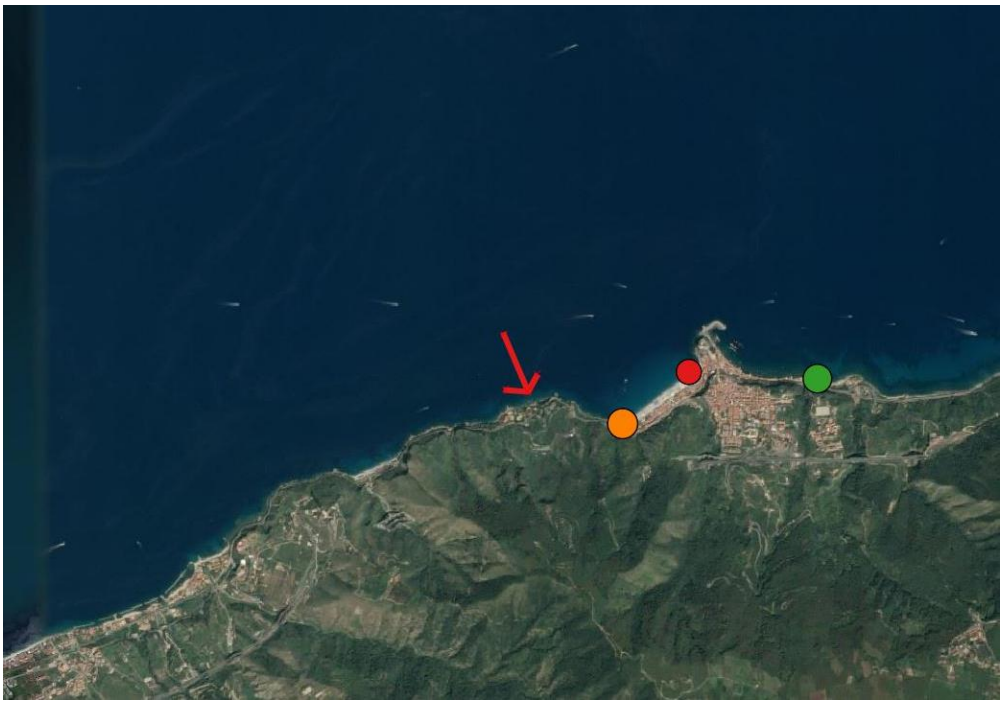

Fig. 4.34 Points where the elevation of the wave was evaluated. In green there is the area of Chianalea; in red Scilla Sud; in orange Scilla Nord. The arrow indicates the position of the landslide and the point where the wave elevation was evaluated (source QGIS).

Area	**X coordinate system WGS/84 33N [m]**	**Y coordinate system WGS/84 33N [m]**
Monte Pacì (landslide source)	561300	4234100
Scilla Marina Nord	561850	4234100
Scilla Marina Sud	563360	4234350
Chianalea	562320	4234370

Table 12 *Coordinates of the points where the wave propagation is calculated.*

The results obtained are the following:

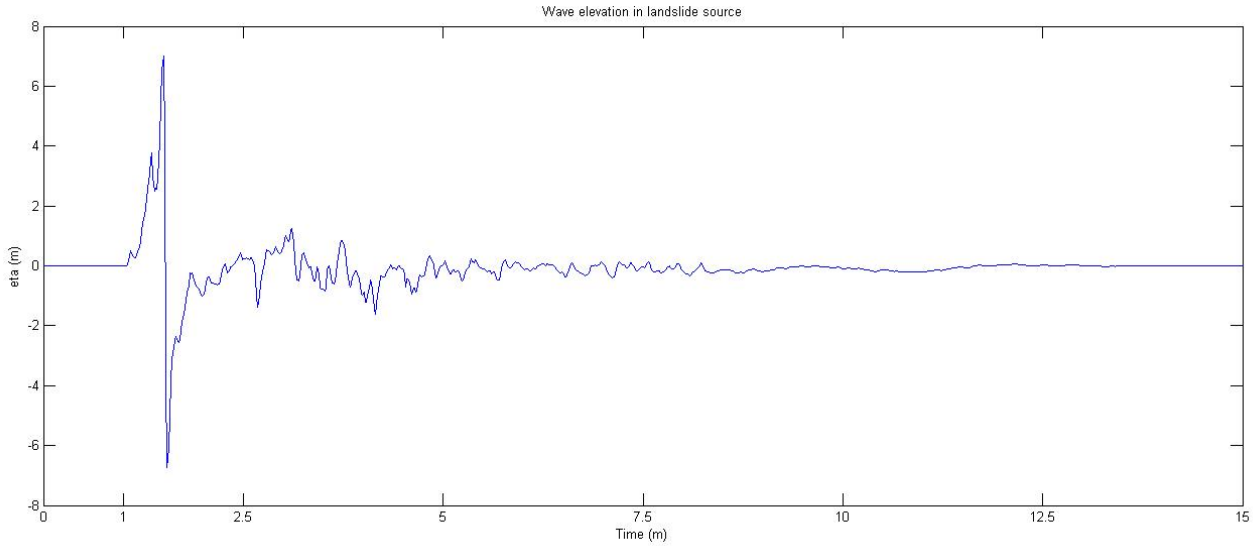

Fig. 4.35 Free surface elevation obtained from the depth integrated model in Monte Capo Pacì (the landslide source).

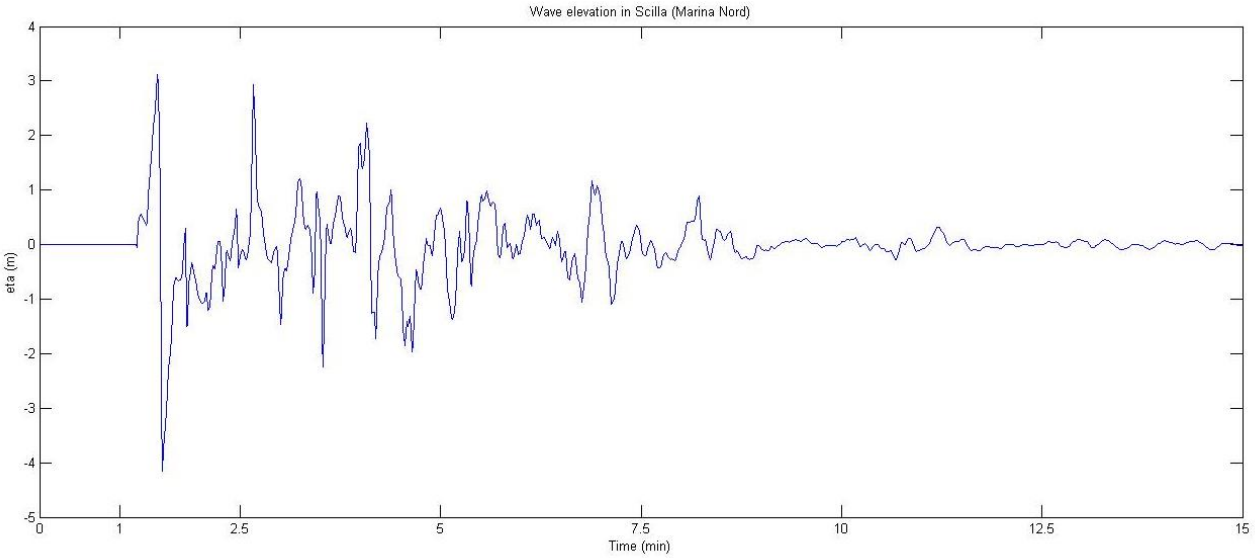

Fig. 4.36 Free surface elevation obtained from the depth integrated model in Scilla Marina Grande Nord.

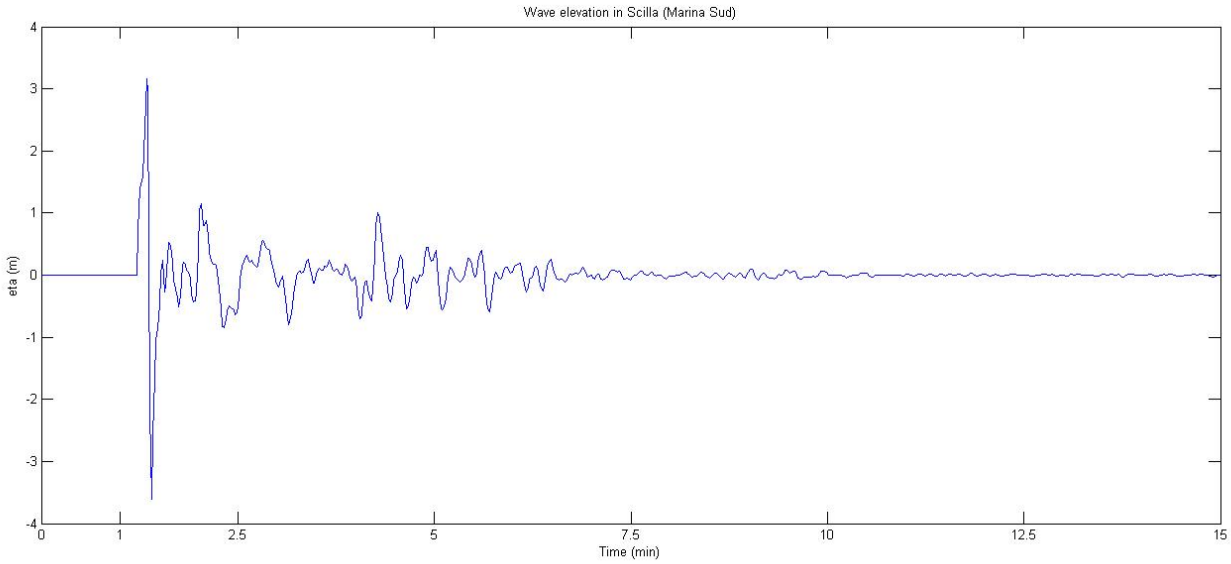

Fig. 4.37 Free surface elevation obtained from the depth integrated model in Scilla Marina Grande Sud.

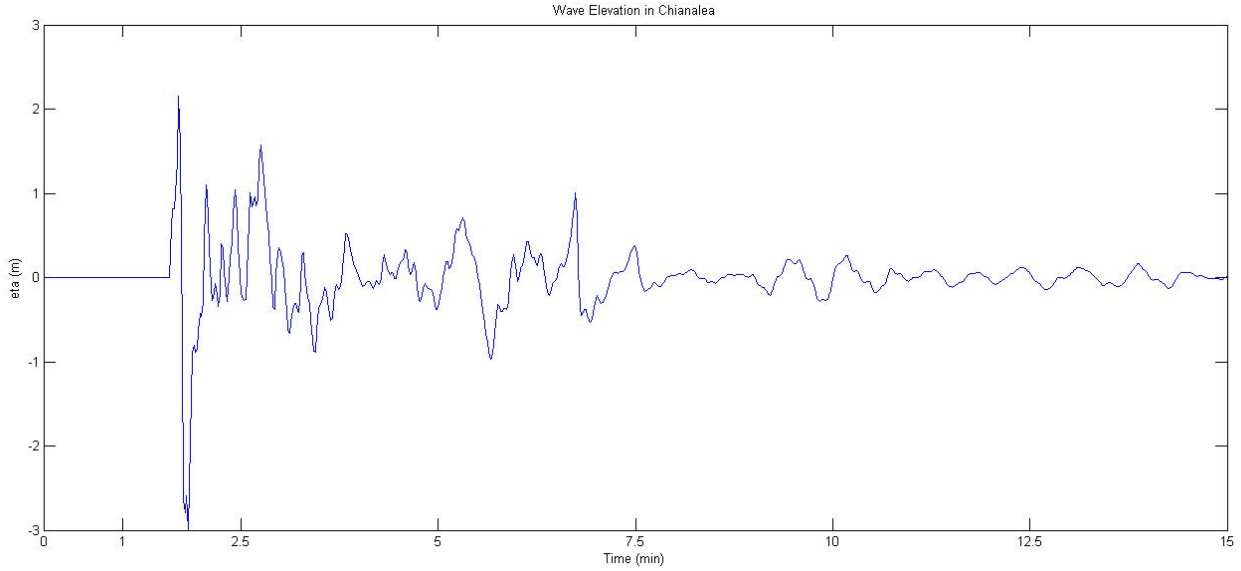

Fig. 4.38 Free surface elevation obtained from the depth integrated model in Scilla Chianalea.

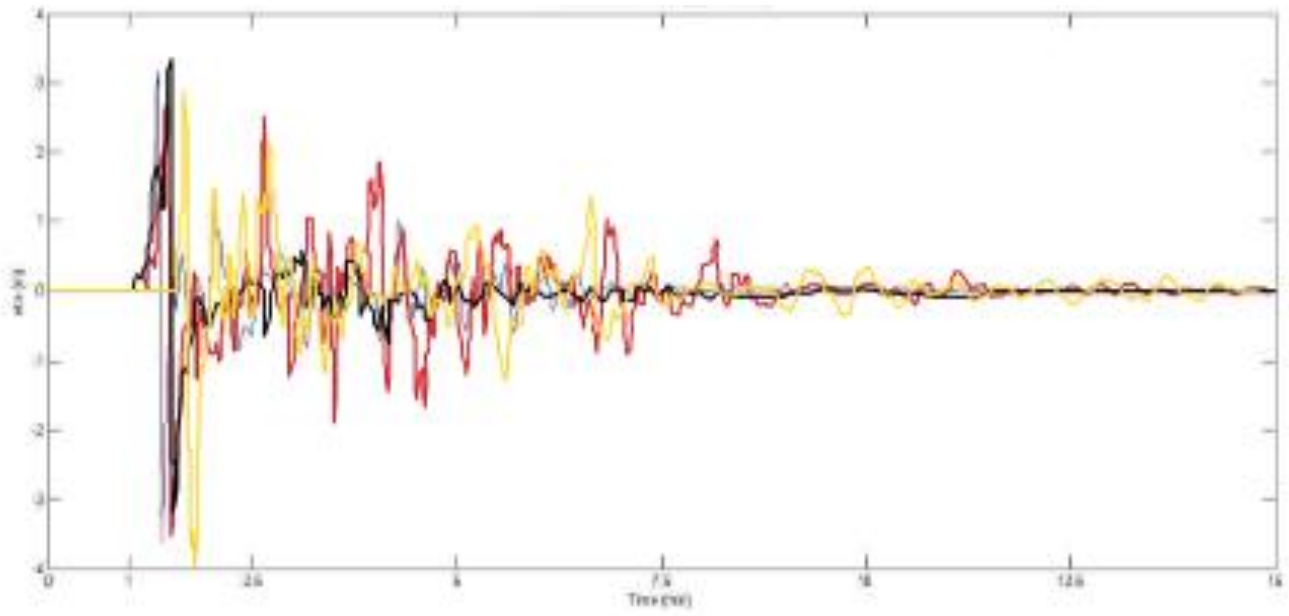

Fig. 4.39 Superimposition of the four distributions to better highlight the different effects of the tsunami at the considered locations. In blu there is the free surface elevation in Scilla Marina Grande Sud, in red there is the free surface elevation in Scilla Marina Grande Nord, in black there is the free surface elevation in landslide source, in yellow there is the free surface elevation in Scilla Chianalea.

4.4.7 Discussion

A numerical model developed by Bellotti (2008) and based on the mild-slope equation was applied to reproduce the propagation of small-amplitude transient waves. The model make use of the Fourier Transform to convert the time-dependent hyperbolic equation into a set of elliptic equations in the frequency domain.

Regarding the hypothesis made in this study on the shape and the sliding time of the landslide necessary for the simulation, reference was made to models and simulations developed by other authors, in particular Mazzanti and Bozzano (2008).

Once the landslide and its movement had been hypothesized, it was inserted in the model and the event was simulated. The data were compared with the historical data deriving from a collection of testimonies from survivors.

Figure 4.35 shows free surface elevation near the source of the event, along landslide movement in Monte Capo Pacì; ("historical sources confirm that the time sequence of the earthquake, landslide

and tsunami can be seen as the first clear evidence of a landslide source for the tsunami. As a matter of fact, according to historical reconstructions, the landslide occurred about 30 min after the earthquake, and the tsunami hit the adjacent Marina Grande beach 30–60 s after the landslide") and is characterized from one main wave triggered about 60 sec after the detachment of the landslide.

Figures 4.36 and 4.37 shows the impact of the event in Marina Grande di Scilla, the area most severely affected by the tsunami.

In the northern Scilla area the tsunami arrived almost simultaneously at Capo Pacì after about 1 minute, and it was the area most severely hit not only by the main wave that arrived on the coast but also by others that followed which had less intensity but still had a disastrous effect on the coast ["three main waves hit the shore, with heights ranging from 6 to 9 m (Sarconi 1784) (see Fig. 2.8b for location). The land was flooded for at least 100 m, with a 200 m ingression in correspondence of the Livorno stream, in the center of Marina Grande (point 7 in Fig. 2.8b)"].

In the southern Scilla area the main wave arrived some seconds after northern Scilla.

The impact, albeit disastrous, was less strong than in the northern part, the waves following the main one were of lower intensity, as evidenced also by the difference in the level of run up reached between the north and the southern part of Scilla ("maximum run-up heights ranging from 6 to 9 m according to Sarconi (1784) and up to 16 m according to Minasi (1785) were recorded respectively along the south and the north of Marina Grande beach").

Figure 4.38 shows the free surface elevation in the area of Chianalea; the main wave arrived about 90 sec after the tsunami was triggered and its intensity was lower, as expected as one moves away from the source of the event and as evidenced by historical sources ("The tsunami hit the cliffs of the Scilla Castle and affected the hamlet of Chianalea (point 8, Fig. 2.8b) on the other side of the Scilla promontory, with waves around 3–4 m high.").

Numerical modelling can provide important and useful information for coastal hazard assessment, on the interaction of the tsunami waves with the local coastal morphology of a given area, and the numerous man made developments existing today.

At the same time, recognizing a landslide-tsunami when the mass failure is entirely submarine is highly challenging, even though it is indispensable for mitigating potential risks associated with future events, considering that the arrival time of these tsunamis on the coast is very short while the associated run-up can be very extensive.

The starting point for identifying areas predisposed to such tsunamis, are marine surveys and the analysis of historical tsunamis where these events are adequately documented. The application of this methodology should lead to the calculation of thematic maps related to hazard, vulnerability, and risk, such as inundation maps and, therefore, the acquisition of all available information on the state of vulnerability in the area.

So far, no such maps exist for the Italian coast, which means that filling this gap should be a priority task over the next few years. As for the analysis of historical events, it is important to point out here that changes in coastal morphology because of erosive phenomena must be taken into account. These are due both to natural (such as the inequality between longshore and river sediment transport) and anthropic causes (such as the presence of coastal structures), as widely addressed in the Afterword, this activity should address the assessment of the level of risk in different areas, and tsunami modeling can provide very interesting and useful information on wave interaction with local coastal morphology and the various existing infrastructures.

Clearly, the identification and monitoring of areas threatened by tsunamis and the definition of potential tsunami sources are essential to mitigate this danger especially in populated areas. Furthermore, the use of reliable and detailed physical models, such as those presented above, become indispensable to this activity.

Once the possible scenarios have been defined as illustrated above and consequent possible actions have been noted, the basic idea is to think of appropriate countermeasures. Therefore, this type of analysis of large historical events, which might repeat in the future, should be the basis for any action aimed at the development of tsunami risk assessment for the Calabrian coast area. Subsequently an alert system could be planned, based on the use of wavemeters that continuously acquire wavelength measurements, mid and peak times and propagation direction.

These parameters are useful to recognize a possible tsunami wave and to identify the coastal tracts that might be affected, on the basis of previous modeling.

5. RISK ANALYSIS AND MANAGEMENT OF TSUNAMIS IN CALABRIA

In recent years, risk assessment has been playing an increasingly important role in coastal territory planning and management. The observations and the current climate change forecasts (eg sea level rise, frequency of intense storms, etc.) show a greater exposure of the coastal areas to risk determinants and, in particular, to erosion and inundation phenomena.

In tsunami event, especially, inundation is devastating and closely connetted with erosion and urbanization.

The critical analysis concerns not only the physical processes responsible for erosion phenomena and flooding, but also the characteristics of the natural environment, the anthropic environment and the interactions between the two. The growing urbanization of coastal areas, mainly linked to the construction of tourist settlements in the territories of greater environmental value, has led to an increase in the vulnerability of coastal areas and their consequent exposure to storms, erosion and floods.

The study analyzes the 1783 Scilla tsunami event with the use of QGIS.

It then hypothesizes that this event were to affect the same areas in two different historical periods, in 1954 and today, so as to be able to evaluate the influence of excessive urbanization and coastal erosion on the risk of flood deriving from an event of such reach. The images of the area in 1954 were provided from the Open Data section of the Calabrian Geoportal (http://geoportale.regione.calabria.it/) in geotiff format, while the images of the area today provided by QGIS in Bing Map format.

5.1 Methodology

Risk, a probabilistic concept, is the probability that a certain event occurs that can cause harm to people. The notion of risk implies the existence of a source of danger and of the possibility of it causing damage.

In this case, the source of the damage is represented by the tsunami event that causes a coastal inundation involving both buildings and people. Risk is closely linked to the concept of vulnerability

of the exposed coastal areas due to the excessive anthropization which has increased over the last 50 years.

The aim of coastal zone management is a correct connection between economic, social and political needs that allow the reduction of these risk factors as far as possible.There are two steps to follow in order to undertake risk analysis and management in the considered area:

1. Analysis of observed data;
2. Use of data from existing studies;

In this paper an analysis was made of observed historical data by Minasi and De Lorenzo who recorded both the height of the tsunami waves that hit the beach and the consequent inundation distance.

5.2 Results

The study consisted of the evaluation of the inundated areas by the tsunami, assuming, however, two different possible scenarios of the same event:

- Effects of the considered event in 1954,
- Effects of the considered event in the present day.

The analysis, in fact, concerned the possible effects of a devastating natural hazard like a tsunami on the coasts, taking into account urbanization, which has tripled since 1950, and with it, therefore, also the effects of an event of this magnitude in the same area. The images of the area in 1954 were provided from the Open Data section of the Calabrian Geoportal (http://geoportale.regione.calabria.it/) in geotiff format, while the images of the area today were provided by QGIS in Bing Map format. For the comparison between the two hypotheses a cartography of 1954 was used as other dated open source cartographies are not available.

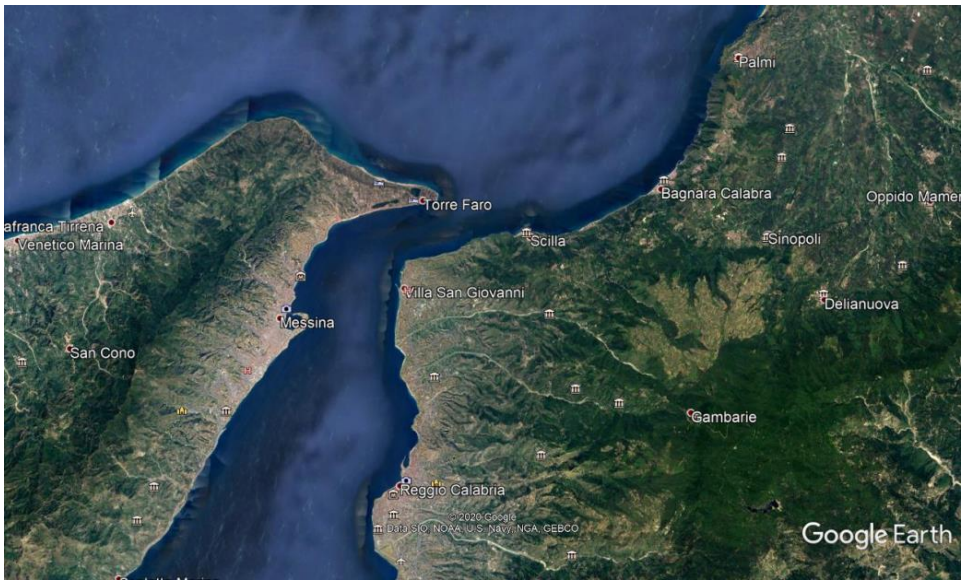

Fig. 5.1 Location of the areas with values of historical data: Scilla, Cannitello (Villa San Giovanni), Reggio Calabria (source Google Earth).

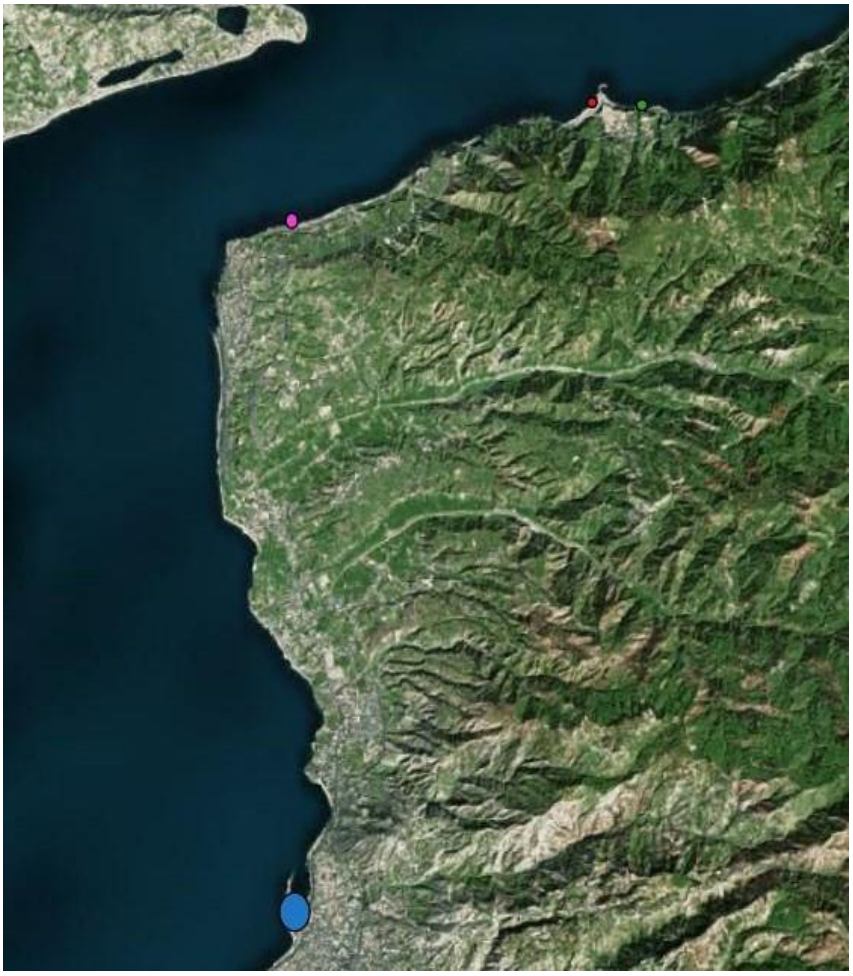

Fig. 5.2 Location of the points where the inundation is evaluated (source QGIS).

The comparison between the inundated areas in 1954 and the present day was made using QGIS. Locations were only taken into consideration where inundation values from historical data were available.

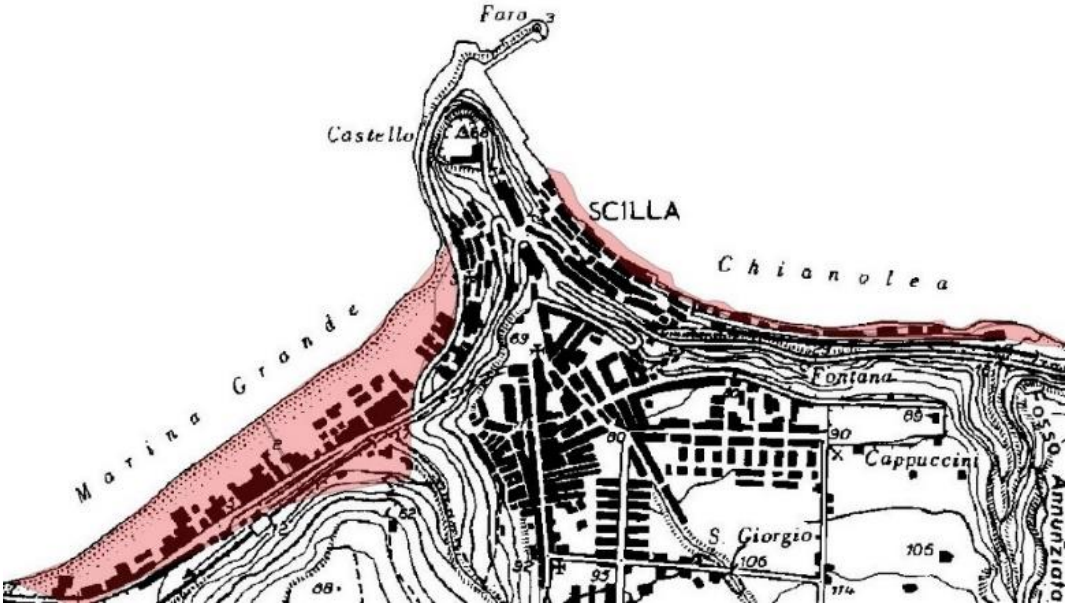

Fig 5.3 Inundation hypothesis in pink of 200 m near Livorno river and of 90 m along St. Nicola's Church in Marina Grande and of 10 m in Chianalea, (Calabrian Geoportal,1954).

Fig 5.4 Inundation hypothesis in pink of 200 m near Livorno river and of 90 m along St. Nicola's Church in Marina Grande and of 10 m in Chianalea, (Bing, present day).

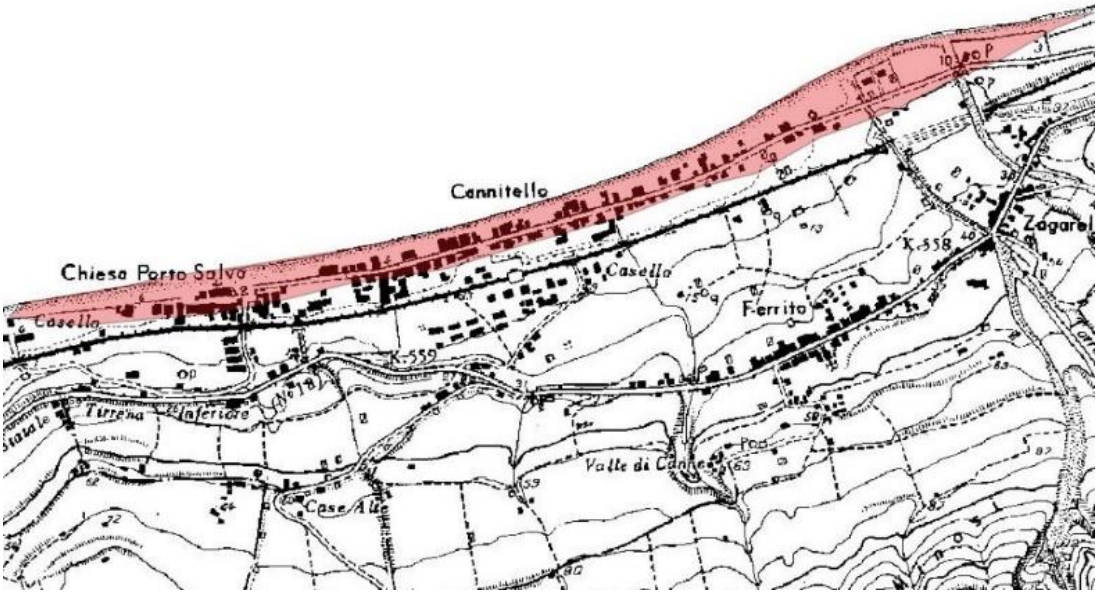

Fig 5.5 Inundation hypothesis in pink of 50 m in Cannitello (Villa San Giovanni), (Calabrian Geoportal,1954).

Fig 5.6 Inundation hypothesis in pink of 50 m in Cannitello (Villa San Giovanni), (Bing, present day).

Fig 5.7 : Inundation hypothesis in pink of 80 m in Reggio Calabria, (Calabrian Geoportal,1954).

Fig 5.8 Inundation hypothesis in pink of 80 m in Reggio Calabria, (Bing, present day).

5.3 Discussion

As can be seen from the images, the same tsunami event, and therefore the same inundation, would have quite different effects in the two cases although quantitatively the flood is the same. Today the effects due to coastal anthropization would be much more devastating and would flood many more buildings and infrastructures that are immediately next to the coast. In Marina Grande and Chianalea the presence of buildings and commercial activities near the coast has tripled, bringing with it a major increase of the risk both for the buildings and, above all, the loss of human lives in the face of an event of magnitude similar to that of 1783. Even in Cannitello (Villa San Giovanni) and Reggio Calabria the conditions are very similar to those of Scilla.

As can be seen from the comparison between the two images, the problem of coastal erosion, from 1950 to today, has reduced the portion of the beach by more than half, thus exposing the inhabited areas near the coast even more to devastating inundation.

In Cannitello the beach has been reduced from a width of 55 m to 25 m, in Marina Grande from a width of 95 m to 60 m, in Chianalea the beach had a width of 15 m in 1954 and nowadays there is no beach, finally in Reggio Calabria the reduction has been from 60 m to 30 m.

There is a very close correspondence between the coastal phenomena that contribute to the balance of the coastal area itself, and the time when this balance is broken by humans who constantly increase urbanization of these areas, As a consequence, related dangers and risks are growing exponentially.

Good risk management begins with the ability to restore the natural balance of phenomena affecting the coast, for example, the interaction between rivers and the sea. It allows a transport of sediments which counteracts coastal erosion. It then counteracts the excessive anthropization of coastal areas by means of strict policies of compliance with building and environmental standards.

CONCLUSIONS

Numerical modelling can provide important and useful information for coastal hazard assessment, on the interaction of the tsunami waves with the local coastal morphology of a given area, and with the numerous man-made developments that exist today. Clearly, this kind of study is necessary for correctly assessing tsunami hazards in a given region and/or coastal town.

Furthermore, the identification and the monitoring of areas threatened by tsunamis and the definition of potential tsunamigenic sources are essential for mitigation of this type of geohazard especially in populated areas.

The 1783 Scilla case study demonstrated both the validation of a model that can be used to simulate possible events of this magnitude on the Calabrian coasts and the possibility of having a reliable tsunami early warning system; it has also the advantage of perfectly combining computational burdens and goodness of results.

A numerical model developed by Bellotti (2008) and based on the mild-slope equation was applied to reproduce the propagation of small-amplitude transient waves. The model make use of the Fourier Transform to convert the time-dependent hyperbolic equation into a set of elliptic equations in the frequency domain.

It is a depth integrated numerical model for the simulation of the generation and the propagation of tsunamis generated by submerged landslides. The model is able to reproduce with low computational costs the full frequency dispersion of the waves and uses an ad hoc treatment for the incorporation of the effects of the moving seafloor to reproduce the generation of the waves.

The model's equations contain a source term which allows the reproduction of the seafloor movements. It was calculated as the time derivative of the water depth multiplied by a transfer function which depends on the generated wave frequencies.

This application is presented to show the applicability of the present approach to real life scenarios; in order to predict the possible effects of an event of this magnitude on Calabrian coasts and to prepare an efficient evacuation plan for the areas affected by the flood.

The important feature of the model is that it is very robust.

After the unit source term computations have been carried out, the results at the points of interest are also obtained for very unrealistic/noised input time series. This is important because when applying the model in real time the system should also work using truncated input time series: when

a tsunami is detected by the tidal gauges, the tsunamis early warning system immediately has to forecast the wave properties at the target points.

It is unrealistic, given the limited time available for spreading the warning, to wait until the tsunamis have been completely measured; it is therefore clear that as the tsunamis are measured, the available time series is to be used as input data.

This study is combined with the analysis of possible effects in terms of inundation of the tsunami event that occurred in 1783, taking into consideration the same areas inundated during the event itself. It was hypothesized that this event had occurred in the same areas in two historical periods, in 1954 and the present, in order to evaluate the effects of the inundation under different conditions both from the point of view of anthropization and coastal erosion.

We have seen how these two variables have strongly influenced the different impact that the event would have had in those areas. For good risk management of tsunamis, it is necessary to improve these two conditions; the reduction of anthropization in coastal areas and a project to reduce coastal erosion on the Calabrian coasts.

This type of analysis of large historical events, that will repeat in the future, should be the basis for any action aimed at the development of tsunami inundation maps for the region of Calabria.

To date, the question of how to protect a given segment of a coastal industrial plant, or private buildings and houses from tsunami attack, within a given period of time (or return period), has been debated.

The only reasonable action that can be taken is that of considering the largest events known to have hit the area of interest, such as the 1783 Scilla case or 1908 Messina Straits case, to best reconstruct these events from their historical source, simulate the events through numerical modelling, and compute tsunami wave action on coastal environments and structures that need to be protected.

The combination between numerical simulations of the tsunami events and the analysis of their impact on the area of interest should be applied to computing thematic maps related to hazard, vulnerability, and risk, such as inundation maps for all coastal segments and sites in Calabria and Sicily, the regions that are most exposed to tsunami.

No such maps exist for any single part of the Italian coasts, which means that filling this gap should be an high-priority task for tsunami scientists in Italy in the coming years.

BIBLIOGRAPHY

- Argnani, A., Armigliato, A., Pagnoni, G., Zaniboni, F., Tinti, S., and Bonazzi, C.: Active tectonics along the submarine slope of south-eastern Sicily and the source of the 11 January 1693 earthquake and tsunami, Nat. Hazards Earth Syst. Sci., 12, 1311–1319, www.nat-hazards-earth-syst-sci.net/12/1311/2012/, doi: 10.5194/nhess-12-1311-2012, 2012.
- Argnani A, Tinti S, Zaniboni F, Pagnoni G, Armigliato A, Panetta D, Tonini R (2011) The eastern slope of the southern Adriatic basin: a case study of submarine landslide characterization and tsunamigenic potential assessment. Mar Geophys Res 32:299–311. doi:10.1007/s11001-011-9131-3.
- Assier-Rzadkiewicz S, Heinrich P, Sabatier PC, Savoye B, Bourillet JF (2000) Numerical modelling of a landslide-generated tsunami: the 1979 Nice event. Pure Appl Geophys 157:1707–1727.
- Augusti, M.: Dei terremoti di Messina e di Calabria dell'anno 1783, memorie e riflessioni, Bologna (in Italian), 1783.
- Avolio MV, Lupiano V, Mazzanti P, Di Gregorio S (2009). A cellular automata model for flow-like landslides with numerical simulations of subaerial and subaqueous cases. EnviroInfo 2009 (Berlin), Environmental Informatics and Industrial Environmental Protection: Concepts, Methods and Tools. Copyright _ Shaker Verlag 2009. ISBN: 978-3-8322-8397-1
- Baratta M (1901) I Terremoti d'Italia. Saggio di Storia, Geografia e Bibliografia Sismica Italiana, F.lli Bocca, Turin, Italy (in Italian).
- Baratta M (1910) La catastrofe sismica calabro-messinese (28 dicembre 1908). Rend Soc Geogr It 496 (in Italian).
- Barbaro, G., Saline Joniche: a predicted disaster. Disaster Advances, 6(7), pp. 1–3, 2013.
- Barbaro, G., Master Plan of solutions to mitigate the risk of coastal erosion in Calabria (Italy), a case study. Ocean & Coastal Management, 132, pp. 24–35, 2016.
- Barbaro, G., Foti, G. & Sicilia, C.L., Coastal erosion in the South of Italy. Disaster Advances, 7, pp. 37–42, 2014.
- Bellotti, G., Cecioni, C., and De Girolamo, P.: Simulation of small-amplitude frequency-dispersive transient waves by means of the mild-slope equation, Coast. Eng., 55(6), 447–458, 2008 doi:10.1016/j.coastaleng.2007.12.006.

- Bellotti, G., Di Risio, M., and De Girolamo, P.: Feasibility of Tsunami Early Warning Systems for small volcanic islands, Nat. Hazards Earth Syst. Sci., 9, 1911–1919, doi:10.5194/nhess-9-1911-2009, 2009.
- Bellotti, G., Beltrami, G.M., De Girolamo, P., 2003. Internal generation of waves in 2D fully-elliptic mild-slope equation FEM models. Coastal Engineering 49 (1-2), 71–81.
- Beltrami, G.M., Bellotti, G., De Girolamo, P., Sammarco, P., 2001. Treatment of wave-breaking and total absorption in a mild-slope equation FEM model. Journal of Waterway Port Coastal and Ocean Engineering-ASCE 127 (5), 263–271.
- Berkhoff, J.C.W., 1972. Computation of combined refraction-diffraction. Proceedings of the 13th International Conference On Coastal Engineering- ASCE, Vancouver, Canada.
- Berkhoff, J.C.W., 1972. Computation of combined refraction-diffraction. Proceedings of the 13th International Conference On Coastal Engineering-ASCE, Vancouver, Canada.
- Bosman A, Bozzano F, Chiocci FL, Mazzanti P (2006) The 1783 Scilla tsunami: evidences of a submarine landslide as a possibile (con?)cause. EGU 2006, Geophysical Research Abstracts, 8,p 10558.
- Bozzano F, Gaeta M, Martino S, Mazzanti P, Montagna A, Prestininzi A (2008) The 1783 Scilla rock avalanche (Calabria, Southern Italy). In: Chen Z, Zhang J, Li Z, Wu F, Ho K (eds) Proceeding of the 10th international symposium on landslides and engineered slopes, 30 June–4 July 2008, Xi'an (China), vol II. Taylor and Francis Group, London, pp 1381–1387.
- Bozzano F, Esposito E, Lenti L, Martino S, Montagna A, Paciello A, Porfido S (2010) Numerical modelling of earthquake-induced rock landslides: the 1783 Scilla case-history (Southern Italy). In: Fifth int. conf. on recent advances in earthquake engineering and soil dynamics, 24–29 May 2010, San Diego, California, Paper n.4.2b.
- Cecioni, C. and Bellotti, G.: Modeling tsunamis generated by submerged landslides using depth integrated equations, Appl. Ocean Res., 32(3), 343–350, doi:10.1016/j.apor.2009.12.002, 2010.
- Cecioni, C. and Bellotti, G.: Inclusion of landslide tsunamis generation into a depth integrated wave model, Nat. Hazards Earth Syst. Sci., 10, 2259–2268, 2010 doi:10.5194/nhess-10-2259-2010.
- Comastri, A. and Mariotti, D.: I terremoti e i maremoti dello Stretto di Messina dal mondo antico al XX secolo: descrizioni e parametri, estratto dal volume: *Il terremoto e il maremoto*

del 28 dicembre 1908: analisi sismologica, impatto, prospettive, a cura di G.Bertolaso, E.Boschi, E.Guidoboni e G.Valensise, DPC–INGV, Roma–Bologna 2008, 813 pp.

- COMSOL Multiphysics User's Guide.
- De Leone, A.: Giornale e notizie de' tremuoti accaduti l'anno 1783 nella provincia di Catanzaro, Napoli, (in Italian), 1783.
- De Lorenzo A (1877) Memorie da servire alla storia sacra e civile di Reggio e delle Calabrie. Reggio Calabria, Cronache e Documenti inediti o rari, Vol I.
- De Lorenzo A (1895) Un secondo manipolo di monografie e memorie reggine e calabresi, Siena Graziani L, Maramai A, Tinti S (2006) A revision of the 1783–1784 Calabrian (southern Italy) tsunamis. Nat Hazards Earth Syst Sci 6:1053–1060.
- Di Risio, M., De Girolamo, P., Bellotti, G., Panizzo, A., Aristodemo, F., Molfetta, M. G., and Petrillo, A. F.: Landslidegenerated tsunamis runup at the coast of a conical island: new physicalmodel experiments, J. Geophys. Res., 114, C01009 doi:10.1029/2008JC004858, 2009.
- Di Risio M, Bellotti G, Panizzo A, De Girolamo P. Three-dimensional experiments on landslide generated waves at a sloping coast. Coastal Engineering 2009;56:659_71.
- Enet, F. and Grilli, S. T.: Experimental Study of Tsunami Generation by Three-Dimensional Rigid Underwater Landslides, J. Waterw. Port C.-ASCE, 133(6), 442–454, doi:10.1061/(ASCE)0733-950X(2007)133:6(442), 2007.
- Foti G., Barbaro G., Bombino G., Fiamma V., Puntorieri P., Minniti F. & Pezzimenti C., Shoreline changes near river mouth: case study of Sant'Agata River (Reggio Calabria, Italy). European Journal of Remote Sensing, 52(sup.4), pp. 102–112, 2019.
- Foti, G. & Sicilia, C.L., Analysis, evaluation and innovative methodologies to prevent coastal erosion. WIT Transactions on Ecology and the Environment, 169, pp. 219–230, 2013
- Graziani, L., Maramai, A., and Tinti, S.: A revision of the 1783–1784 Calabrian (southern Italy) 5 tsunamis, Nat. Hazards Earth Syst. Sci., 6, 1053–1060, 2006.
- Grilli, S. T., Vogelmann, S., and Watts, P.: Development of a 3D numerical wave tank for modeling tsunami generation by underwater landslides, Eng. Anal. Bound. Elem., 26, 301–313, doi:10.1016/S0955-7997(01)0113-8, 2002.
- Grilli, S. T. and Watts, P.: Modeling of waves generated by a moving submerged body. Applications to underwater landslides, Eng. Anal. Bound. Elem., 23, 645–656, doi:10.1016/S0955- 7997(99)0021-1, 1999.

- Guidoboni, E., Ferrari, G., Mariotti, D., Comastri, A., Tarabusi, G., and Valensise, G.: CFTI4Med, Catalogue of Strong Earthquakes in Italy (461 B.C.-1997) and Mediterranean Area (760 B.C.-1500). INGV-SGA. http://storing.ingv.it/cfti4med/, 2007.
- Hamilton W (1783) Relazione dell'ultimo terremoto delle Calabrie. Inviata da S.E.G. Hamilton e tradotta dal dottor G.Sella, Firenze.
- Harbitz CB, Pedersen G (1992) Model theory and large water waves, due to landslides. Preprint Series, 4, Department of Mathematics, University of Oslo.
- Kervella Y, Dutykh D, Dias F. Comparison between three dimensional linear and nonlinear tsunami generation models. Theoretical and Computational Fluid Dynamics 2007;21:245_69.
- Kirby, J.T., Lee, C., Rasmussen, C., 1992. Time-dependent solutions of the mild-slope wave equation. In: Edge, Billy L. (Ed.), Proceedings of the twenty-third International Conference on Coastal Engineering-ASCE, Venice, Italy, vol. 3, pp. 391–404. New York, 0-87262-933-3, 3600 pp.
- Liu, P.L.-F., Wu, T.-R., Raichlen, F., Synolakis, C. E., and Borrero, J.: Runup and rundown generated by threedimensional sliding masses, J. Fluid Mech., 536, 107–144, doi:10.1017/S0022112005004799, 2005.
- Lynett, P. J. and Liu, P. L. F.: A numerical study of submarinelandslide-generated waves and run-up, P. Roy. Soc. London, 458, 2885–2910, 2002.
- Lynett, P. J. and Liu, P. L. F.: A numerical study of the runup generated by three-dimensional landslides, J. Geophys. Res., 110, C03006, doi:10.1029/2004JC002443, 2005.
- Mazzanti P (2008a) Studio integrato subaereo-subacqueo di frane in ambiente costiero: i casi di Scilla (RC) e del lago di Albano (RM). Giornale di Geologia Applicata 8(2):245–261.
- Mazzanti P (2008b) Analysis and modelling of coastal landslides and induced tsunamis. PhD Thesis ''Sapienza'' University of Rome, Department of Earth Sciences.
- Mazzanti P, Bozzano F (2009) An equivalent fluid/equivalent medium approach for the numerical simulation of coastal landslide's propagation: theory and case studies. Nat Hazards Earth Syst Sci 9:1941–1952.
- Mazzanti P, Bozzano F, Avolio MV, Lupiano V, Di Gregorio S (2009) 3D numerical modelling of submerged and coastal landslides' propagation. In: Mosher DC, Shipp C, Moscardelli L, Chaytor J, Baxter C, Lee H, Urgeles R (eds) Submarine mass movements and their

consequences IV advances in natural and technological hazards research, vol 28. Springer, The Netherlands, pp 127–139.

- Mazzanti P, Bozzano F (2011) Revisiting the February 6th 1783 Scilla (Calabria, Italy) landslide and tsunami by numerical simulation. Mar Geophys Res 32:273–286. doi:10.1007/s11001-011-9117-1.
- Mercalli G (1906) Alcuni risultati ottenuti dallo studio del terremoto calabrese dell'8 settembre 1905. Atti dell' Accad Pont di Nap 36:1–9.
- Minasi G 1785, Continuazione ed appendice sopra i tremuoti descritti nella relazione colla data di Scilla de 30 settembre 1783, con altro che accadde in progresso, Messina.
- Minasi A (1970) La specola del filosofo, Natura e sorti nelle incisioni di Antonio Minasi, Ilario Principe, ''Brutium''.
- Nwogu, O., 1993. Alternative form of the boussinesq equations for nearshore wave propagation. Journal of Waterway Port Coastal and Ocean Engineering- ASCE 119, 618–638.
- Panchang, V.G., Wei, G., Pearce, B.R., Briggs, M.J., 1990. Numerical simulation of irregular wave propagation over shoal. Journal of Waterway Port Coastal and Ocean Engineering-ASCE 116 (3), 324–340.
- Panizzo, A., Bellotti, G., De Girolamo, P., 2002. Application of wavelet transform analysis to landslide generated waves. Coastal Engineering 44 (4), 321–338.
- Peregrine, D.H., 1967. Long waves on a beach. Journal of Fluid Mechanics 27,815–827.
- Sarconi, M.: Istoria de' fenomeni del tremuoto avvenuto nelle Calabrie e nel Valdemone nell'anno 1783, Napoli (in Italian), 1784.
- Tinti, S., Bortolucci, E., and Chiavettieri, C.: Tsunami Excitation by Submarine Slides in Shallow-water Approximation, Pure Appl. Geophys., 158(4), 759–797, doi:10.1007/PL00001203, 2001.
- Tinti, S., Manucci, A., Pagnoni, G., Armigliato, A., and Zaniboni, F.: The 30 December 2002 landslide-induced tsunamis in Stromboli: sequence of the events reconstructed from the eyewitness accounts, Nat. Hazards Earth Syst. Sci., 5, 763–775, doi:10.5194/nhess-5-763-2005, 2005.
- Tinti, S., Pagnoni, G., and Zaniboni, F.: The landslides and tsunamis of the 30th of December 2002 in Stromboli analyzed through numerical simulations, B. Volcanol., 68(5), 462–479, doi:10.1007/s00445-005-0022-9, 2006.

- Tinti S, Guidoboni E (1988) Revision of the tsunamis occurred in 1783 In Calabria and Sicily (Italy). Sci Tsunami Hazards 6(1):17–22.
- Tinti S, Maramai A, Graziani L (2004) The new catalogue of Italian tsunamis. Nat Hazards 33:439–465.
- Tinti S, Maramai A, Graziani L (2007) The Italian Tsunami Catalogue (ITC), Version 2. http://www.ingv.it/servizi-e risorse/BD/catalogotsunami/ catalogo-degli-tsunami-italiani.
- Tinti S, Piatanesi A (1996) Finite-element simulations of the 5 February 1783 Calabrian tsunami. Phys Chem Earth 21:39–43.
- Tinti S, Tonini R (2013) The UBO-TSUFD tsunami inundation model: validation and application to a tsunami case study focused on the city of Catania, Italy, Nat Hazards Earth Syst Sci, 13, 1795–1816, www.nat-hazards-earth-syst-sci.net/13/1795/2013/, doi: 10.5194/nhess-13-1795-2013.
- Vivenzio G, 1788, Historia dei tremuoti avvenuti nella provincia di Calabria ulteriore e nella citta` di Messina nell'anno 1783, Napoli.
- Zaniboni F, Armigliato A, Tinti S (2016) A numerical investigation of the 1783 landslide induced catastrophic tsunami in Scilla, Italy. Nat Hazards 84(2):455–470.
- Zaniboni., Pagnoni G., Gallotti G., Paparo M. A., Armigliato A., Tinti S., Assessment of the 1783 Scilla landslide-tsunami effects on Calabria and Sicily coasts through numerical modeling. Nat. Hazards Earth Syst. Sci., 2019.
- Zaniboni F, Armigliato A, Pagnoni G, Tinti S (2014a) Continental margins as a source of tsunami hazard: the 1977 Gioia Tauro (Italy) landslide-tsunami investigated through numerical modelling. Mar Geol 357(2014):210–217. doi:10.1016/j.margeo.2014.08.011.
- Zaniboni F, Pagnoni G, Armigliato A, Elsen K, Tinti S (2014b) Investigations on the possible source of the 2002 landslide tsunami in Rhodes, Greece, through numerical techniques. In: Lollino G, Manconi A, Locat J, Huang Y, Canals Ardilas M (eds) Eng Geol Soc Territ—volume 4. doi:10.1007/978-3-319-08660-6_17. _ Springer International Publishing Switzerland 2014.
- Zaniboni F, Pagnoni G, Armigliato A, Tinti S, Iglesias O, Canals M, (2014c) Numerical simulation of the BIG'95 debris flow and of the generated tsunami. In: Lollino G, Manconi A, Locat J, Huang Y, Canals Ardilas M (eds) Eng Geol Soc Territ—Volume 4, doi:10.1007/978-3-319-08660-6_19. _ Springer International Publishing Switzerland 2014.

- Zaniboni F., Tinti S. (2014) Numerical simulations of the 1963 Vajont landslide, Italy: application of 1D Lagrangian modelling. Nat Hazards 70:567–592. doi:10.1007/s11069-013-0828-2